School of Civil and Mechanical Engineering
Department of Civil Engineering

Impacts of Turbulent Mixing on Nutrient Load in the Swan Estuary

Mahmood Hajiani

This thesis is presented for the Degree of
Doctor of Philosophy
of
Curtin University

September 2013

Abstract

Stratification is one of the most important causes of water quality deterioration. Stratification usually acts to isolate the bottom of the water column from surface water, via a strong density gradient. The consequence is an anoxia zone in the bottom that accelerates nutrient release from the sediment. However, turbulent vertical mixing plays an indispensible role in eroding the stratification. A full understanding of vertical mixing can be achieved via numerical simulation and field measurements. However, numerical simulation is highly dependent on field measurements, as field measurements provide the necessary data (initial condition and validation data) for modelling. Further, vertical mixing in a numerical simulation usually is modelled via turbulence closure schemes. In fact, closure schemes present turbulent vertical mixing based on microstructure profiles of some measurable variables. Therefore, field measurement data are not only necessary for running a numerical model (initial and validation data), but are also essential to propose new closure schemes or validate an available vertical mixing routine. Further, microstructure data can be used to achieve a deep insight into turbulent vertical mixing.

In this study, data collected from three direct field measurements in the lower part of the Swan River Estuary in Western Australia were arranged to provide a data set of estuarine processes that can be used for validation of closure schemes or running a numerical model by providing all the necessary data (initial condition, validation condition, and supplementary data). Moreover, data was used to gain a better understanding of vertical mixing in a stratified shear flow. To achieve the maximum accuracy in the study, different approaches to estimate different variables were tried.

The rate of dissipation of turbulent kinetic energy was estimated by three different approaches (Batchelor curve fitting, inertial subrange, and the shear microstructure method). The results from the three methods were similar. However, there were some difficulties in using the Batchelor and inertial subrange methods. The Batchelor method needs an extra visual inspection to discard inappropriate fit that means one may lose valuable information contained in discarded segments. The inertial subrange method is inconvenient, especially when the measured spectrum does not show a clear subrange. Therefore, shear dissipation was the sole method that showed acceptable results and convenient application.

Flow velocity measured in the field was compared with the velocity from a time-dependent inverse method. Both approaches showed a similar flow direction. However, the velocity magnitude within the two methods was different, as the inverse method shows averaged velocity over the interval of two transects, while direct measurements present instantaneous velocity.

The Swan River Estuary field measurements were conducted in a sheltered area during the daytime. So, wind and natural convection did not affect the turbulence. To enhance data sets, some microstructure profiles measured in a thermally stratified lake were added to the available data, where wind energy at the surface, internal wave motions, natural convection and shear instability forced the turbulence. Turbulent vertical mixing was studied using the data sets. Eddy diffusivity of mass and turbulent viscosity as a function of gradient Richardson number (Ri_g) showed three distinct zones. The first region was a weak stratification regime (Ri_g <0.01). The second range was an intermediate band of gradient Richardson number (0.01 < Ri_g <0.25). Within the first two regimes, eddy diffusivity was larger than eddy viscosity. In the third range Ri_g > 0.25 and eddy diffusivity and eddy viscosity dropped dramatically due to the increasing gradient Richardson number. However, in this regime, in some segments turbulent viscosity was larger than eddy diffusivity that was caused by the effects of horizontal anisotropy and contamination by the effect of internal waves.

The variability of the Schmidt number (turbulent Prandtl number (Pr_t)) was studied within four regimes (down-gradient buoyancy and momentum fluxes, down-gradient buoyancy and up-gradient momentum fluxes, up-gradient buoyancy and up-gradient momentum, and up-gradient momentum and down-gradient momentum fluxes). The large populations within each zone revealed that up-gradient fluxes are as important as down-gradient fluxes. When both buoyancy and momentum fluxes were down-gradient, within one-tenth log bins of gradient Richardson number showed the minimum scatter from the best-fitted curve. In the weak stratification zones, Pr_t showed an asymptote in the range of 0.4-0.8. However, when both fluxes had the same sign, the Schmidt number increased with the increasing gradient Richardson number.

The study showed that the comprehensive study of vertical mixing is achieved when both down-gradient and up-gradient fluxes are weighted similarly to each other. Moreover, it was observed that turbulence could survive even for Ri_g <0.25.

Dedication

To

Vajihe my lovely, unique, and supportive wife for all love and support. Thank you for being with me during the hard time of my life.

My parents for their encouragement and love especially my **mother** who taught me patience and perseverance.

My Sister for her dedication

My brothers

Thanks all; you made it for me possible to complete this dissertation.

Acknowledgement

I would like to express my deepest appreciation to my supervisor Dr Ranjan Sarukkalige for his strong support, not only in study but also in my life. I am sure that the accomplishment of this work would not be possible without your support. Thank you for all valuable lessons that gave me in academic and personal life. I will not forget your kindness.

I would like to thank Prof. Jorg Imberger from Centre for Water Research (CWR) at University of Western Australia for great support and advice. You opened my eyes to interesting field of study. Thank you for your invaluable time that allocated to me.

I would like to thank A/Prof Clelia Marti for her support and advice.

I would like to express my appreciation to Prof. Hamid Nikraz the head of Department of Civil Engineering for his support.

Especial thanks to all CWR staff in their assistance in using field equipments and support during field observations.

I would not have been able to undertake this postgraduate research without the generous financial assistance provided by the Curtin University through a Curtin International Postgraduate Scholarship (CIPRS).

Table of contents

List of Tables

List of Figures

1 Introduction

1.1 Background

Water resources play an indispensable role in different aspects of human life and the aquatic environment. Water bodies are a vital environment and habitat for various species of plant and animal, numerous microorganisms, and support aquatic ecosystems. Anthropogenic activities such as construction, land developments for urbanization and agricultural activities have led to the deterioration of water bodies. Global warming and the growing population have amplified the damage even more. All these lead to environmental issues such as algal blooms, anoxia zones in water columns, and salt intrusions into rivers.

These irreversible damaging effects on water bodies have led to pressure on governors and managers to implement sustainable management practices. The idea of sustainable development is to balance the interaction of different influencing factors affecting natural waters (Yeates, 2007). The outcome of sustainability is to protect the water bodies from environmental deterioration. Before any practical action can be taken, a good understanding of the physics and ecology of water environments is essential. A full description of past, present, and future physical, chemical, and biological states of a water body leads to a comprehensive strategic plan in which all influencing factors in natural waters can be specified to mitigate the water quality deterioration. In other words, the relationship between earlier and current times helps to make a healthy future for natural waters. Field measurements and numerical modelling are usually invoked to conduct hydrodynamic and water quality studies of natural waters. These two approaches are very close related to each other. In fact field measurements enable researchers to study the quality of natural waters and even more to examine the performance of numerical models and pave the way for further improvements of such models to respond well to all kinds of different conditions. A good understanding of some phenomena such as stratification in quality research is very important. The majority of water bodies experience

stratification during a period of time (Boehrer and Schultze, 2008). Stratification amplifies the quality issues. It acts as a barrier for vertical mixing. The consequence is some phenomena such an anoxia zone in the bottom of the water column or algal blooms. To understand the stratification, microstructure measurements of turbulence properties provide invaluable information. Turbulence has the potential to mix the stratified water columns in the phenomenon called turbulent mixing. Turbulent mixing acts to erode the stratification (Yeates, 2007); therefore it lessens the quality problems in natural waters. For example, vertical mixing can improve the anoxia zone by bringing oxygen saturated surface layers to bottom waters or moderate the side effects of pollution by dilution.

Numerous closure schemes have been proposed to estimate vertical mixing (K_ρ). These closures are based on the relationship between measured turbulence variables. It assumes that vertical mixing can be estimated as a function of turbulence variables. For example, one of the most popular approaches is to calculate the diapycnal mixing based on the gradient Richardson number (Ri_g) (Forryan et al., 2013; Simanjuntak et al., 2011; Yeates, 2007; Yeates et al., 2013). Many efforts have been exerted in recent years to improve the understanding of turbulent mixing and the performance of the mixing closures based on field measurements.

1.2 Research problem

Turbulence is ever-present in natural waters and it has a central role in mixing water columns within shear-stratified waters. Numerous studies have been conducted to estimate turbulent fluxes in water bodies (Etemad-Shahidi and Imberger, 2002a; Saggio and Imberger, 2001). However, the majority of these studies have focused on a particular space or time (Trevethan and Chanson, 2009). An instrument is installed in a point of the river at constant depth; the observations then are applied for whole water bodies, while the results present a snap-shot of turbulence in different stages of its evolution. Some other field measurements have been conducted in limited periods (Etemad-Shahidi and Imberger, 2002b). They neglected the long estuarine or lake process that can provide all necessary inputs for numerical simulation and

examination of turbulence closure schemes. Flow velocity has been measured with instruments. However, the question is: how accurate is the velocity measurement?

As mentioned earlier, quantifying the vertical mixing is essential to managing water quality and ecology. Although the diapycnal mixing can be directly estimated in the field, in most of studies the rate of vertical mixing has been indirectly estimated from other turbulent properties (Etemad-Shahidi and Imberger, 2005; Etemad-Shahidi and Imberger, 2006). Using these indirect approaches is applicable when certain assumptions are met. Usually the indirect methods overestimate the buoyancy flux due to considering that there is a constant mixing efficiency (Etemad-Shahidi and Imberger, 2005; Etemad-Shahidi and Imberger, 2006). While many studies have shown that there are up-gradient fluxes as many as down-gradient fluxes (Etemad-Shahidi and Imberger, 2001), usually the indirect methods neglect negative buoyancy fluxes (Etemad-Shahidi and Imberger, 2005). K_ρ can be indirectly determined from the rate of dissipation (ε) of turbulent kinetic energy (TKE). The dissipation itself is estimated from different approaches. But which approach can relatively present the best estimate of dissipation?

When a laminar flow evolves to turbulence, the gradient Richardson number must be less than a critical value. It is usually agreed that at $Ri_g < 0.25$ shear instability may be triggered (Yeates et al., 2013). The turbulence onsets to transfer kinetic energy from large eddies (containing scales) to small scales in a process called turbulent cascade. In this evolution, the gradient Richardson number is modified to $Ri_g \ll 0.25$ (active turbulence). The turbulence eventually is collapsed at a scale called the Kolmogorov scale, where kinetic energy is converted to heat (decaying turbulence). The turbulence is in decaying mode when $Ri_g > 0.25$. So far, the majority of studies have considered the active turbulence and they neglected decaying turbulence (Yeates et al., 2013). The essential question is if there are any consequences for turbulence studies in neglecting the turbulence in a regime of strong stability $(Ri_g > 0.25)$?

1.3 Aims and objectives

The research aims are:

- To provide a data set of estuarine process that can serve for validation of closure schemes at the process level. The data have been organized to provide all necessary inputs to allow a validation of the numerical simulation: initial conditions, forcing meteorological and tidal data as well as all validating data.
- To examine the data to provide a better understanding of vertical mixing in a stratified shear flow and so derive a generic understanding of turbulent mixing.

The research objectives are:

- To compare three different approaches (Batchelor curve fitting, inertial subrange and shear microstructure methods) to estimate the rate of dissipation of Turbulent Kinetic Energy (TKE).
- To use the inverse method to estimate flow velocity as an alternative approach to direct measurements in estimating flow velocity.
- To find out how turbulent viscosity (eddy viscosity) responds to changes in gradient Richardson number.
- To study the variability of Schmidt number (turbulent Prandtl number (Pr_t)) as a function of Ri_g .

1.4 Research scope

The extent of the proposed study is given as follows:

- A considerable extent of study allocated to literature reviews to find the existing issues in the proposed field.

- The lower part of Swan River Estuary in Western Australia was selected as the domain of study, where the deepest point of the river (with a depth of about 21 m) is located.
- Microstructure measurements were conducted during three days on 27 August (initial condition), 8 October (validation condition), and 2 November 2012 (supplementary data).
- The measurements covered different tidal conditions such as spring and neap tides.
- Microstructure measurements were confined to velocity, temperature, conductivity and dissolved oxygen during the field studies. However, pH and turbidity were measured on 8 October 2012 to use for the inverse method.
- To overcome the difficulty of the non-stationary nature of turbulence, we applied a segmentation algorithm based on temperature gradient measurement.
- The rate of dissipation of TKE was estimated by three different approaches.
- The mean variables (salinity, temperature, dissolved oxygen, turbidity, pH) measured on 8 October were used to run the inverse method to estimate the velocity field as an alternative to direct measurements. Field measurement on that day was confined to ebb tide, allowing the tracers to move an appreciable distance, though short compared to the diurnal tidal period.
- The turbulent vertical mixing was studied with the microstructure profiles measured in the Swan River Estuary and some additional data measured in Lake Kinneret. In fact diapycnal mixing studies were supported with comprehensive data sets from the estuary and lake.

1.5 Innovation and contribution to knowledge

Although many research projects have been conducted to study turbulent fluxes and vertical mixing in natural waters (Etemad-Shahidi and Imberger, 2006; Saggio and Imberger, 2001; Yeates et al., 2013), this study has tried to add something new to previous findings. This was achieved either by exerting modifications to previous studies or by examining some aspects of the science that were neglected. These can be introduced as follows:

- Flow velocity estimated from direct measurement with a falling instrument (Portable Flux Profiler (PFP)) was validated by a time-dependent inverse method.
- Shear square (S^2) previously (Etemad-Shahidi and Imberger, 2001; Yeates et al., 2013) was calculated based on $S^2 = (\partial v_1 / \partial x_3)^2 + (\partial v_2 / \partial x_3)^2$

  where v_1 and v_2 are horizontal velocities. The estimate of shear square is central to the calculation of the gradient Richardson number and so to turbulence studies. However, the previous way of estimating the shear must be modified as shear is given by a partial differential equation of horizontal velocities ($v_h = (v_1^2 + v_2^2)^{1/2}$) in the vertical direction. The shear should be estimated from:

  $S = \partial v_h / \partial x_3 = \partial (v_1^2 + v_2^2)^{1/2} / \partial x_3 = (v_1 \partial v_1 / \partial x_3 + v_2 \partial v_2 / \partial x_3) / (v_1^2 + v_2^2)^{1/2}$.
- The rate of dissipation of kinetic energy was determined from three different approaches: Batchelor dissipation (ε_B), the inertial subrange method and shear microstructure dissipation (shear dissipation (ε_s)).
- Vertical mixing was studied not only with data collected in the Swan River Estuary, but also with some additional microstructure data recorded in a thermally stratified lake. This approach makes a comprehensive conclusion for vertical mixing in natural waters. In the domain of the study in the Swan River Estuary, shear was the dominant mechanism by which energy is transferred to turbulence. However, in the lake, not only the shear instability due to internal waves, but also wind energy at surface layers and natural cooling convection during night-time, feed the turbulence.
- Eddy diffusivity of mass was directly estimated as(Thorpe, 2007):

  $K_\rho = \overline{v_3' \rho'} / \partial \rho / \partial x_3$

  where v_3' and ρ' are vertical velocity fluctuations and density fluctuations, and ρ is the density.
- Not only eddy diffusivity of mass was studied, turbulent viscosity was involved in this research.

- The Schmidt number (turbulent Prandtl number) was studied as a function of gradient Richardson number for both down-gradient and up-gradient of mass and momentum fluxes.
- A quadratic zone due to the nature of turbulent fluxes were depicted: (1) positive buoyancy and momentum fluxes (down-gradient fluxes); (2) positive buoyancy fluxes with negative momentum (up-gradient) fluxes; (3) negative buoyancy and momentum fluxes; (4) negative buoyancy fluxes with positive momentum fluxes.

1.6 Thesis structure

This thesis is organized in 7 chapters. The structure of all chapters is similar. Firstly, a brief literature review regarding the main topic is explained in the *Introduction* section. All equations and science background related to that particular topic is given in the *Methodology* section. Methodology is followed by the *Results* section, where the findings are presented. The outcomes are discussed in the *Discussion* part. Finally, each chapter is finished with a summary.

Chapter 2 includes the instrumentation, the domain of study (area of field measurements), and data processing. In this chapter, firstly the instrument used to collect microstructure data is introduced, with all necessary detailed descriptions. Secondly, the method of signal processing and data acquisition and reduction is illustrated. Thirdly, the domain in which measurements were conducted is described, with a description of the meteorology station and tide gauge. The three different field trips conducted in the lower part of the Swan River Estuary are then explained. Finally, how the turbulent properties were estimated within temperature gradient stationary segments is illustrated.

Chapter 3 contains descriptions of the application of three different methods to estimate the rate of dissipation of kinetic energy. The chapter is started with a short introduction of the importance of estimating the turbulent kinetic energy dissipation. Then Batchelor curve fitting method, as the first approach to estimate dissipation, is introduced focusing on important criteria for application. Then the methodology of

using the Batchelor approach is presented. Batchelor dissipation results are given in the results section. The second approach is the inertial subrange method, which is firstly introduced with the necessary assumptions for application. The method of application is described. Finally, the results are presented. As the last alternative, the shear dissipation method is explained, with the method of application. Outcomes are given in the results part. The results of the three approaches are discussed and finally, a summary is presented.

Chapter 4 presents the findings of the three different field studies conducted in the Swan River Estuary. A brief literature review is given in the introduction. Before showing the results of each field trip, a brief of background and the environmental conditions on that particular day is given. Then the chapter is divided into three parts. Firstly, the results of turbulent fluxes measured on 27 August 2012 during spring tides in the domain, is presented. This data is considered as the initial condition. Secondly, the findings of a high resolution of time and space measurement conducted on 8 October 2012 are explained, when the estuary experienced a neap tide condition. High-resolution measurements were conducted on that day to provide the necessary inputs for the inverse method. The data from 8 October 2012 is assumed to be the validation condition. Thirdly, the turbulent fluxes measured on 2 November 2012 are demonstrated. The results of the three field studies are discussed to find out their key points. Finally, with a summary, the chapter is closed.

Chapter 5 is allocated to the results of the inverse method. As previously mentioned, a high-resolution time and space measurement was conducted on 8 October 2102 to provide the necessary input data for the inverse technique, to estimate velocity field. The chapter starts with an introduction that is followed by the derivation of the transport equation. Inverse velocity is then presented and compared with the direct measurements of velocity. A summary is given at the end of the chapter.

Chapter 6 includes the study of turbulent mixing. The variability of eddy diffusivity of mass, turbulent viscosity, and Schmidt number as a function of gradient Richardson number for both positive and negative fluxes are studied. All findings in this chapter resulted from microstructure data from the estuary and a lake. This

chapter is organized as follows. Firstly, the significance of vertical mixing in natural waters is supported with a relatively short literature review. Secondly, the structure of eddy viscosity and eddy diffusivity as a function of Ri_g is studied. Thirdly, the variability of Pr_t as function of Ri_g is presented. Then the important outcomes of the chapter are discussed. Chapter finishes with a summary.

Chapter 7 presents the conclusions. Then some recommendations for future studies are provided.

2
Instrumentation and domain of field measurements

Since the first direct measurement of turbulent properties in natural waters in the early sixties, instruments and techniques have considerably improved. These advancements have been enriching the knowledge of turbulence in the fluid mechanics field. Whilst previously, long studies of water bodies or examination of some theories were impossible, these days the conduct of such field experiments is an easy task. Introduction of sophisticated hardware and software has led to the invention of some instruments that can be manipulated far from the study sites. However, the invention of each instrument or technique has its own limitation. In this study we used a sophisticated Portable Flux Profiler (PFP) developed at Centre for Water Research (CWR), at University of Western Australia for the field measurements. This chapter mainly presents related information on field instrumentation. The methods of signal processing, data acquisition, and data preparation are described. The chapter is followed by introducing the domain of study and finishes with the definition of some turbulent properties and scales.

2.1 Introduction

The first direct measurements of small scale turbulent motions was conducted by (Grant, Stewart et al. 1962) in the well mixed and tidal influenced Discovery Passage off the west coast of Canada. For first time, the studies were performed in an environment with a high Reynolds number of about 10^8 that was considerably larger than values that were observed in the laboratory. The objective was to study the $-5/3$ Kolmogorov power law. To perform the research, they attached hot-film anemometers on a research ship to estimate velocity fluctuations. Since then the techniques and instruments have dramatically advanced. (Imberger and Head 1994) have introduced four reasons for this fast advancement. The first reason for the changes can be attributed to the introduction of specific signal processing chips (DSP chips). The most important characteristic of these chips is that they help researchers to make instruments with a high capacity for signal processing. The second factor is the presence of cheap power utilization compared to earlier times. Moreover, the introduction of computer memory with a larger capacity of data storage has paved the way too. The third reason can be attributed to the introduction of laser and acoustic velocity measurement. With these facilities, the background concentrations of particles can be estimated. The fourth reason is the existence of very accurate sensors, which have the capability to measure the different tracers such as temperature, conductivity, and dissolved oxygen.

The field measurements are categorized in two main groups (Thorpe 2007). The first is that in which turbulent fluxes are advected past a fixed point with a mean velocity v, and the temporal variations of turbulence then are recorded. The second option is when an instrument with a nominal speed passes through a water column while recording all changes in turbulent properties. In both methods, invoking Taylor‘s frozen hypothesis converts the frequency domain to the wavenumber domain. In other words, instead of temporal gradients, space gradients of measurements are presented.

In natural waters, different instruments provide time series measurements of basin scales (fine scale profiles) or microstructure scale measurements associated with turbulent fluxes or other turbulent properties (Imberger and Head 1994). Time series instruments usually are fixed at the bottom of the water body or floated at the water

surface, measuring different variables. They continuously record the necessary data, though the instruments need regular maintenance. For example, thermistor chains with an accuracy of about ± 0.005 $^{\circ}C$ measure the water temperature (Imberger and Head 1994). The chains can be extended from the surface to the bottom of water columns. The measured data can provide invaluable information such as the annual thermal cycle, stratification pattern, and internal wave motions (Yeates, Imberger et al. 2008). According to (Imberger and Head 1994) there are a variety of scales in the flow field such as basin scale motions (10^4 m), synoptic scales (10^3 m), internal wave and intrusion scales (10^2 m), entraining scales (1 m), and finally turbulent mixing motion (0.001 m). However, fine scales comprise internal wave, intrusion, and entraining motions. Microstructure scales are confined to a range between entraining scales and the Kolmogorov velocity scale (10^{-3} m), and the range is extended down to Batchelor scale (10^{-4} m) where there is still gradient in scalars. In field studies, usually microstructure instruments record temperature, conductivity, dissolved oxygen, and velocity micro-scales (Imberger and Head 1994). Moreover, the application of the Acoustic Doppler Current Profiler has widely increased (George and Lumley 1973; Agrawal 1984; Brumley, Cabrera et al. 1991). In this method, acoustics are used to estimate flow velocity and particle concentration. Measuring the intensity of the backscatter signal as a robust function of signal frequency and the sound target size of the particle, is used to estimate the concentration of particles (Ferguson 1983).

In a study conducted by (Carter and Imberger 1986), they examined vertically rising microstructure profilers to measure temperature and conductivity gradient. The instrument was totally independent from surface motions and collected data with a sample rate of about 100 Hz with a rising speed of about 0.1 ms^{-1}. This gives a vertical resolution of about 1 mm. Then they used the instrument to collect some data in the Swan River Estuary and Koombana Bay in Western Australia. They concluded that the performance of the instrument was acceptable, just that there was a problem in long term drift in the conductivity sensor. To solve this problem, they proposed that it is better to use a large 4-electrode cell.

(Moum 1990) used a falling microstructure profiler in the ocean to estimate the vertical velocity fluctuation. Using a commercially available differential pressure transducer, dynamic pressure was measured. The instrument had a nominal drop

velocity of about 0.9 ms^{-1} and the limitation of vertical velocity fluctuation due to noise in the instrument was about 0.003 ms^{-1}. To know the performance of his instrument, he compared the results from shear probes and the new instrument. Turbulent scales resulting from the two instruments agreed well. He concluded that the instrument could be used to estimate turbulent fluxes using an eddy correlation method.

The performance of a free falling microstructure profiler was examined by (Wolk, Yamazaki et al. 2002). Turbulent velocity shear and temperature gradient were measured with standard turbulence sensors. Moreover, *in situ* chlorophyll and turbidity were measured using a bio-optical sensor. Then measured turbulence spectra from the field test were compared with an empirical spectrum. The results from the two methods well agreed.

The aim of this chapter is to explain the instruments used to collect data in field studies. Moreover, the detailed descriptions of data acquisition, reduction, and preparation for further calculations are illustrated. The domain of field measurements is introduced in this chapter.

2.2 Instrumentation

This study presents comprehensive data sets of microstructure profiles such as a three-component of velocity, temperature, salinity, turbidity, pH and dissolved oxygen taken by a falling Portable Flux Profiler (PFP) (Figure 2.1), a multi-scale probe developed by the Centre for Water Research (CWR) at the University of Western Australia (UWA). The PFP was designed as a free falling profiler and has an overall length of 1 m and weight of 62 kg. The PFP incorporates instruments that sample at 100 Hz for measuring turbulent microstructure; instruments that sample at 50 Hz or measuring fine-scale gradients in temperature, conductivity, velocity, pH and dissolved oxygen (50 Hz) (Imberger and Head 1994); and multi-wavelength fluorometers for measuring fluorescence of photosynthetic pigments and dissolved organic carbon that samples at 1 Hz (Beutler, Wiltshire et al. 2002). The buoyancy of the PFP is adjusted with ballast weights to achieve a free falling speed of 0.1 ms^{-1}, which implies a vertical resolution of about 1 mm for the 100 Hz microstructure measurements. The vertical and horizontal components of the velocity can be measured with the Laser Doppler Anemometers (LDA). The resolution of

measurement is 0.001 ms^{-1} (Saggio and Imberger 2001). The 3-axis LDA system is made of two 2-axis systems attached orthogonally. Therefore, it provides a surplus vertical velocity component. The type of each system is forward scattering, in which light scattered from a particle in the measurement volume is mixed with the reference beams. The result is a Doppler-shifted signal. Using a square-law device, light is mixed. The output of this law is the positive sum and difference of the frequencies, introducing directional ambiguity. Particle motion in one direction or the other will then increase or decrease the detected frequency. The velocity of the scattering particle has a direct relation to Doppler frequency. Velocity components with a magnitude of ±235 mms^{-1} are measured with the PFP. It is worth mentioning that the measured velocity is the velocity of the scattering particle. However, as the size of particle becomes sufficiently small (approx. 5 μm), so it is assumed that the particle velocity and fluid velocity are the same. With the PFP in its vertical position one of the 2-axis systems returns one component of the horizontal velocity and vertical velocity. The second 2-axis system has the same job. Therefore, the PFP can measure the vertical velocity twice.

2.3 Signal processing and data acquisition

Doppler signals are the result of the frequency shifting, mixing, and band-passing processes with a centre frequency of 64 KHz and a range of ±32 KHz. The signals are continuously digitized to 8-bit resolution. Fast Fourier transforms are computed for each 1024-point of data block. Knowing the Doppler sensitivity of the system (139.5 $Hzmm^{-1}s^{-1}$), the velocity and its sign is computed. The 1024-point data blocks are 50% overlapped, so up to 500 velocity estimates per second are being obtained for each channel. Using a low-pass finite impulse response (FIR), velocity signals are converted to a 100 Hz rate to match the sampling rate of the microstructure temperature and conductivity sensors. A flux gate compass and 2-axis inclinometer record the vehicle orientation for later decontamination of the velocity data. A differential GPS records the location of the profiling station. A portable data acquisition system, consisting of a signal interface box and a laptop computer, manages data acquisition and display.

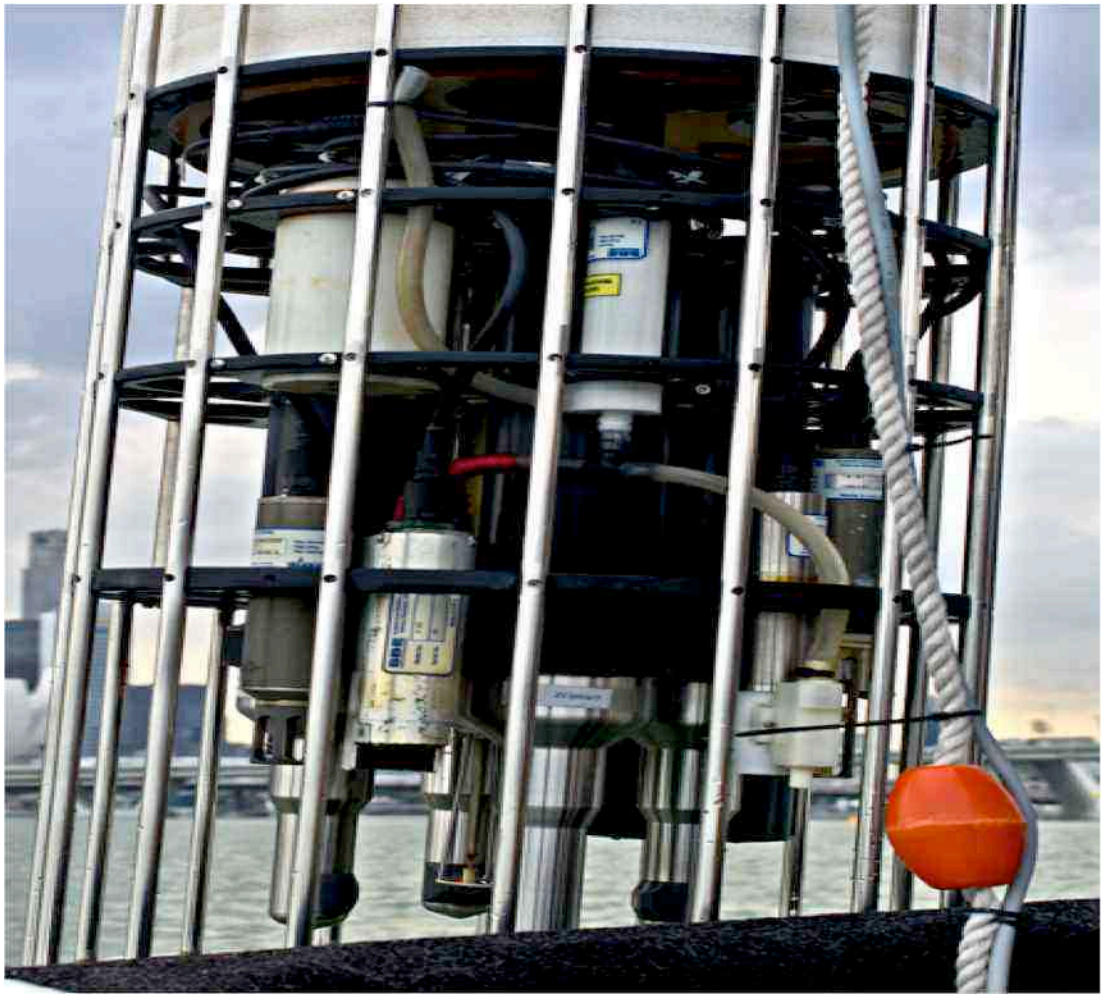

Figure 2.1 Portable Flux profiler (PFP) used to collect microstructure data sets. (www.cwr.uwa.edu.au).

2.4 Data reduction

A series of scripts have been written at the CWR to calculate the different properties of flow, based on raw data measured with the PFP. These scripts use a package, which contains specific programs that perform file formatting, calculation and filtering. The names of the scripts are Pclean, Xaspect, and Plaser. In Pclean, different variables such as drop velocity, flow velocity, salinity, density, and temperature are calculated. All values are saved in some channels. The main function of Pclean is to prepare data for Xaspect and Plaser. In Xaspect, a variety of different filters and functions are performed to calculate many parameters. Temperature stationary segments and Batchelor dissipation are two important outcomes of Xaspect used in Plaser. Plaser contains a series of functions and filters that calculate

turbulent properties of water such as Richardson number, shear, buoyancy frequency, velocity fluctuations, Reynolds stresses, shear dissipation, buoyancy fluxes and eddy diffusivity of mass, based on direct measurements. The major part of this study was allocated to modification and rewriting of Plaser in response to present turbulent properties, all based on direct measurement.

2.5 Domain of field measurements

The Swan River Estuary, a micro-tidal estuary (where the tide range is less than 2m (Masselink and Short 1993)), is located in the southwest of Australia ($31^{\circ}41'$ S and $116^{\circ}04'$ E). The main functions of the estuary are recreation, fishing, transpiration, and urban stormwater disposal. The catchment of the Swan has an area of about 121 000 km^2 (Donohue, Davidson et al. 2001). Three main tributaries feed the river flow: the Avon River, the Canning River, and the Helena River. The Avon River contributes 85 per cent of the fresh water flow (Donohue, Davidson et al. 2001). However, annual mean discharges of the Avon are highly variable, dependent on the seasonal variability of rainfall. The Swan River catchment experiences a Mediterranean climate, with a hot and dry austral summer. The river flows through the city of Perth and discharges to the Indian Ocean at the port of Fremantle (the shipping part of the river). Construction of Fremantle Harbor changed the hydrology of the estuary. Due to deepening in the river mouth, intrusion of oceanic water increased (Hodgkin and Hesp 1998). Moreover, intense anthropogenic activities such as land clearing and urbanization in the surrounding area imposed significant changes in nutrients, sediments, runoff, and salinity of the estuary (Donohue and Trust 1994). The river can be separated in two sections: the lower part (a deep and wide basin) and the upper Swan (a shallow and narrow area) (Stephens and Imberger 1996; O'Callaghan, Pattiaratchi et al. 2010). The deepest part of the Swan is Black Wall Reach, with a maximum depth of about 21 m (Etemad-Shahidi and Imberger 2002). The main basin of the estuary acts as a trap for nutrients and sediments transported from upstream. The upper Swan has a mean depth of about 3m (Stephens and Imberger 1996). In summer and autumn usually, strong stratification is observed in this part of the river, due to high solar radiation, high temperatures, and negligible freshwater inflow due to low rainfall. Rainfall occurs mainly during the

cool winter period and of the 870 mm of annual rainfall, almost 80 per cent occurs from May to September (O'Callaghan, Pattiaratchi et al. 2010). Moreover the upper Swan is characterized by a considerable level of phytoplankton biomass, anoxia at the bottom and dinoflagellate blooms (Hamilton, Chan et al. 2001). While a summer intrusion salt wedge from the Indian Ocean propagates more than 50 km from Fremantle, in winter this distance is limited to 5-20 km from the ocean's entrance (Hamilton, Chan et al. 2001). At the river mouth diurnal tides, with a maximum tidal amplitude of about one metre, force the estuary. However, semi-diurnal tides and sub-tidal oscillation play a role in water surface levels. The magnitude of spring-neap cycles vary from 0.3 to 0.8 m (O'Callaghan, Pattiaratchi et al. 2010).

2.5.1 Field measurements

Field measurements were conducted in the lower part of the Swan River, where the deepest point of the river (21 m) is located (Figure 2.2). Three field studies were carried out on 27 August, 8 October, and 2 November 2012 in the domain, to study mixing and turbulent fluxes (Figure 2.2). The idea was to collect a series of data sets that can provide valuable information for the long term study of estuarine process. The data sets provide all necessary inputs for numerical simulations (initial and validation data) and examination of the performance of different closure schemes. Although all studies were similar in profiling the water column surface to bottom, different profiling stations were chosen in different conditions, such as spring and neap tides, to collect a variety of diverse data sets. The first field measurement was conducted on 27 August during spring tides. This day was assumed as the initial conditions in the Swan Estuary. Although some chemical and biological variables were collected on the first day, temperature, conductivity, and velocity microstructure were used to study turbulent fluxes. A high temporal and spatial measurement was conducted on 8 October 2012. The objective was to estimate the velocity field using an inverse technique to validate measured velocity fields with the PFP. Five consecutive transects were profiled during a period of neap tidal conditions. Ten profiling stations were chosen with a mean horizontal distance between stations of about 200 m. Fifty profiles of temperature, conductivity, velocity, pH and dissolved oxygen were recorded with the PFP. Profiling was started from upstream (first station) and finished near the mouth of the river at Fremantle

(tenth station). Fifty profiles of different passive tracers were provided to feed the inverse method. On 2 November, a supplementary field study was conducted to enhance the available data set for a comprehensive study of turbulent fluxes and vertical mixing in the Swan River Estuary.

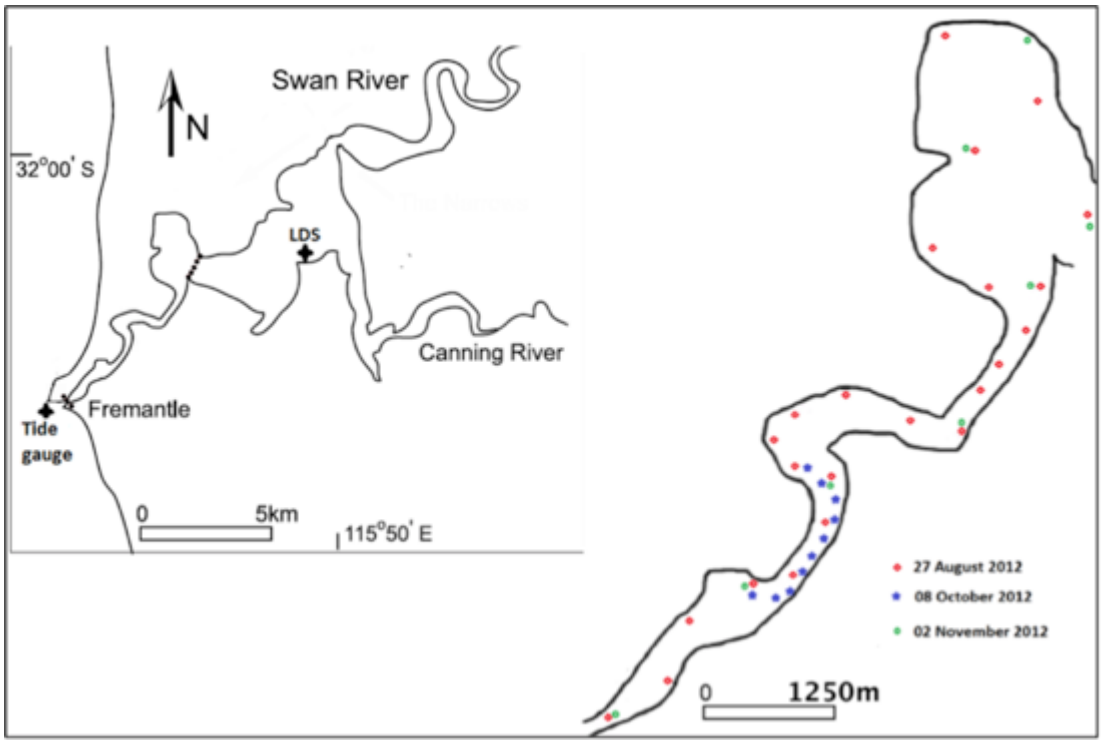

Figure 2.2 Map of Swan River Estuary. Study domain is marked with black dots. The location of stations on different days is indicated with colour markers. Locations of tide gauge and LDS are marked.

2.6 Meteorological and water level data

Water salinity and temperature were continuously measured with a Lake Diagnostic Station (LDS; Global Water Monitoring, Australia) (Imberger 2004). The location of LDS is shown in Figure 2.2. The LDS consisted of 16 fast-response thermistors spaced at 0.5 to 1 m; two conductivity sensors at 0.5 and 8.0 m depths and a pressure sensor located 0.5 m above the bottom. The LDS also recorded wind speed and direction, short wave radiation, net wave radiation, air temperature and relative humidity 2 m above the water surface with a sampling interval of 30 s.

Water surface levels data in Fremantle were measured with a tide gauge belonging to the Department of Transport (Figure 2.2).

2.7 Data Preparation

To compensate for the difference in distance between the pressure (depth) sensor and the conductivity and temperature sensors, a lag distance (0.43 m) was added to the depth channel. The depth channel was then filtered by applying a second order Butterworth low pass filter in both directions at 6.25 Hz. The low pass filter removed fluctuations due to noise in the signal. Applying a 31-point Guassian derivative filter to the depth channel presented the drop velocity. A low pass filter to remove the noise introduced by the derivative filter was then applied to the results. In applying this low pass filter, care was taken to keep the real drop velocity fluctuations that are due the response of the probe to changes in the water density.

The microstructure temperature sensors FPO7 had a response time of 12 ms and a resolution of 0.001 °C. The microstructure conductivity sensors consisted of fast-response, four-electrode units, with a response time of 4 ms and resolution of 0.0004 Sm^{-1}. The microstructure conductivity and temperature sensors each had distinct and non-ideal step responses. The different responses of the sensors caused mismatching between temperature and conductivity sensors. This resulted in a salinity and density spiking phenomenon (Horne and Toole 1980). Two important factors that might cause spiking are a time lag between sensors or different dynamic response functions. While the time lag is removed by physical shifting of the sensors on the instrument, the mismatch in response might be eliminated by filtering the signals of the sensors. Profiles of temperature and conductivity were digitally sharpened. Then signals were smoothed using the method described by (Fozdar, Parker et al. 1985) before being used to derive density and salinity. The sharpening was applied to measure small scale fluid properties such as displacement scales (Imberger 1985). Salinity was calculated following UNESCO algorithms (Fofonoff and Millard 1983).

To overcome the difficulty of the non-stationary nature of turbulence, a segmentation algorithm was applied to the temperature gradient signals (Imberger and Ivey 1991). In this method, an autoregressive (AR) method was individually fitted to two adjacent windows of temperature gradient signals. The AR coefficients that resulted from both windows were used to determine the distance between two stationary segments. Using two adjacent sliding windows, sample by sample, inside the data and finding where the magnitude of an evaluated norm exceeded a threshold value

(30), the boundaries of statistically homogeneous temperature gradient segments were specified (Imberger and Ivey 1991). Displacement scale L_d (vertical distance between position of particle before and after mixing) and density fluctuation ρ' were calculated based on the algorithm explained by (Thorpe 1977) . To calculate L_d and ρ', density signals (Figure 2.3a) were reordered (Figure 2.3b), and then the measured and the reordered signals were compared. Figure 2.3c shows density fluctuations. The centred displacements L_c is an approximation of the overturn scales positioned at the centre of the overturns, and were estimated by averaging of the absolute value of half of the displacement scales (BOASHASH 1986; Saggio and Imberger 2001).

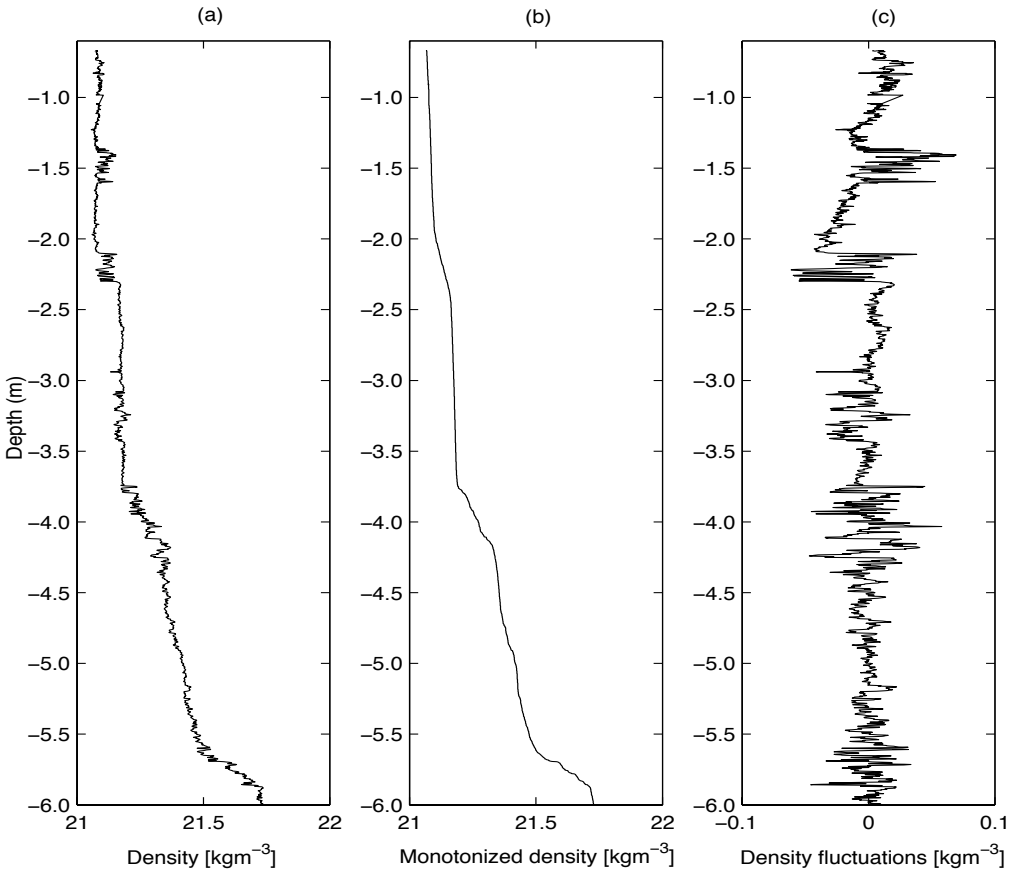

Figure 2.3 Measured density with PFP on 8 October 2012 at 09:33 am in Swan River Estuary showing (a) density, (b) sorted density and (c) density fluctuations.

Flow velocity was estimated from the raw velocity signal measured relative to the probe (Figure 2.4a). Firstly, measured relative velocity was low-pass filtered at 0.4 Hz. Secondly, the horizontal velocities were decomposed to North-South (N-S) and

East-West (E-W), then by integrating the drag forces on the probe, as in the method suggested by Hendricks and Rodensbuch(1981) and Saggio and Imberger(2001). Drag forces were calculated using:

$$dF_i = 0.5\rho_i C(A_1 v_{hi}|v_{hi}| + A_3 v_{hi} v_{3i}) \quad (2.1)$$

where v_{hi} and v_{3i} are the measured horizontal and vertical velocity components relative to the probe, I denote to each sample recorded by PFP, and C is a coefficient equal to:

$C_d/(1+C_m)$ where C_d is the drag coefficient and C_m is the added mass coefficient. A_1 and A_3 are the area projections of the probe. The flow velocities at each point are then given by:

$$v_{i+1} = v_i + dF_i \Delta t M^{-1} \quad (2.2)$$

where Δt is the sampling interval, and M is the mass of the probe. The coefficient C was established by calibration with electro-current meter data collected in the 1997 Lake Ogawara field experiment. In this procedure it was assumed that instrument came to rest once it had settled on bottom.

Velocity fluctuations v' were determined as the difference between measured flow and mean velocity $\overline{v}$ (Figure 2.4b), $v' = v - \overline{v}$ (Figure 2.4c). Therefore, the three velocity fluctuations are v_1', v_2' (horizontal velocity fluctuations in N-S and E-W directions, respectively), and v_3' (vertical velocity fluctuation).

To estimate mean velocity, a non-recursive Gaussian filter was applied to the horizontal v_1, v_2, and vertical v_3 flow velocities. The Gaussian filter had a standard deviation equal to envelope function at each point of the velocity profile. The envelope was defined as the maximum of L_c over a window of length L_c. This window had a variable size adjusted as the magnitude of L_c varied through the profile (Saggio and Imberger 2001). Ensemble averages $\overline{v_3' v_1'}$, $\overline{v_3' v_2'}$, and $\overline{v_3' \rho_3'}$ as well as variances $\overline{v_1'^2}$, $\overline{v_2'^2}$, and $\overline{v_3'^2}$ were estimated by having density and velocity fluctuation, then the velocity scale was estimated as:

$$q = \sqrt{\overline{v_1'^2} + \overline{v_2'^2} + \overline{v_3'^2}} \quad (2.3)$$

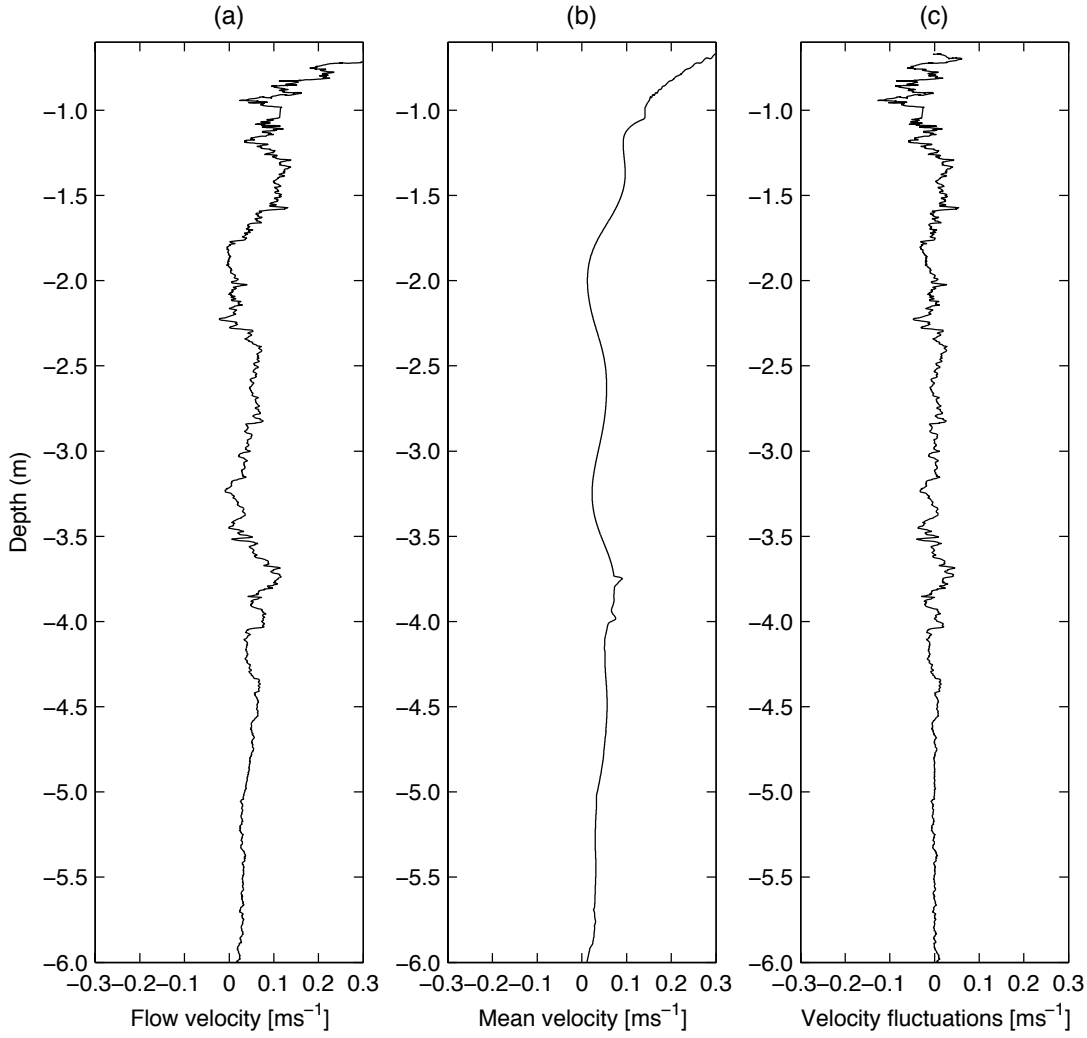

Figure 2.4 Observed velocity with PFP on 8 October 2012 at 09:33 am (a) flow velocity, (b) mean velocity, and (c) velocity fluctuations.

Turbulent kinetic energy (TKE) equation for an incompressible fluid is given by (Ivey and Imberger 1991):

$$-\frac{\partial}{\partial t}\left(\frac{\overline{q^2}}{2}\right)-\frac{\partial}{\partial x_j}\left(\frac{\overline{v_j' q^2}}{2}\right)-\frac{\partial}{\partial x_j}\left(\frac{1}{\rho_0}\overline{v_j' p'}\right)-\bar{v}_j\frac{\partial}{\partial x_j}\left(\frac{\overline{q^2}}{2}\right)-\overline{v_i' v_j'}\frac{\partial \bar{v}_i}{\partial x_j}=\frac{g}{\rho_0}\overline{v_3 \rho'}+\upsilon\overline{\frac{\partial v_i'}{\partial x_j}\frac{\partial v_i'}{\partial x_j}} \quad (2.4)$$

where $\overline{q^2}$ is the twice TKE per unit mass, ρ_0 is the reference density, p' is the pressure fluctuation. (Ivey and Imberger 1991) rewrote the equation as:

$$m = b + \varepsilon \quad (2.5)$$

where m is the net rate of variability, production, and importation of mechanical energy that is used for mixing the stratified water columns, b is the buoyancy flux, and ε is the rate of dissipation of TKE. The methods of estimating the rate of dissipation of kinetic energy are completely illustrated in Chapter 3.

Buoyancy flux was directly calculated by:

$$b = (g / \rho_0)\overline{v_3' \rho'} \tag{2.6}$$

Down-gradient fluxes (when a heavier particle (lighter particle)) moves upward (downward) (Etemad-Shahidi and Imberger 2001) were considered positive and up-gradient fluxes (re-stratification) were assumed to be negative.

Sorted density and flow velocity profiles were low-pass filtered at 0.4 Hz to estimate buoyancy frequency and shear. To understand the strength of a stratified shear flow, buoyancy frequency is given by:

$$N^2 = -(g / \rho_0)\partial\rho / \partial x_3 \tag{2.7}$$

The negative sign is applied because buoyancy frequency for a stable water column is positive. Equation (2.7) implies that the weight of a particle defines the dynamic behaviour of the particle (Imberger 1994). The interpretation of buoyancy frequency is the time scale which a particle needs to return its stable position before mixing events.

Shear was calculated by:

$$S = \partial v_h / \partial x_3 \tag{2.8}$$

where v_h is horizontal flow velocity and x_3 is positive upward.

One important question is: when does a flow become turbulent or unstable? To answer this in steady, two-dimensional, stably-stratified, horizontal shear flows with an ideal Boussinesq assumption, a dimensionless number called the gradient Richardson number, Ri_g, was calculated as a parameter relating to local shear stability:

$$Ri_g = N^2 / S^2 \tag{2.9}$$

Usually, it is assumed that instability in a water column can occur when the gradient Richardson number is less than 1/4 . So, one can expect when the Ri_g somewhere in the flow is increased to more than the threshold value, all fluctuations are dampened due to viscosity and buoyancy and turbulence decays. However, $Ri_g < 1/4$ is a

necessary but not sufficient criterion. For a given flow, there is a critical Richardson number Ri_c in which, if somewhere in the flow gradient the Richardson number was less than the critical Richardson number, flow is unstable. In (Thorpe 2007) a detailed description of how to find a Ri_c has been illustrated.

The median value of N^2, S , and Ri_g over the length of stationary segments were determined. As these variables within the segment did not show a Gaussian distribution (Saggio and Imberger 2001), median values were used instead of mean values (Figure 2.5).

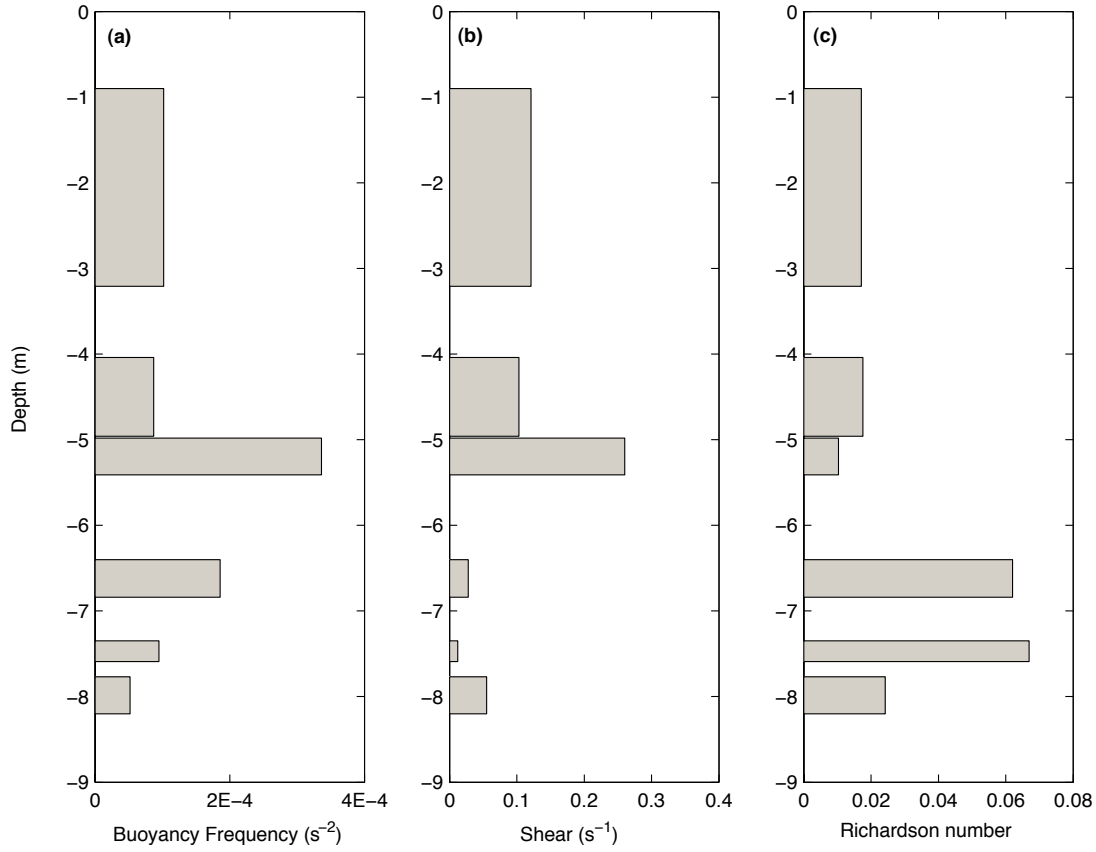

Figure 2.5 Flow properties over the stationary segment length taken with PFP on 8 October 2012 at 08:26 am in Swan River estuary, (a) showing buoyancy frequency, (b) shear, and (c) gradient Richardson number.

2.8 Length scales

There are varieties of length scales in turbulence studies: Batchelor length scale, Kolmogorov length scale, Displacement length scale, Centred displacement scale,

Thorpe length Scale, Ozmidov length scale and Shear length scale. The understanding of these length scales are of prime importance to the study of turbulent mixing in natural waters.

2.8.1 Batchelor length scale

A scale at which the gradients of scalars (gradient of concentration) produce by the rate of strain is balanced by diffusive smoothing (Batchelor 1959; Nihoul and Jamart 1988). Batchelor length scale L_B is given by:

$$L_B = (\upsilon D^2 / \varepsilon)^{1/4} \tag{2.10}$$

where υ is kinematic viscosity and D is the molecular diffusion of heat.

This length scale plays an indispensible role in nutrient uptake by aquatic systems. (Taylor and Stocker 2012) stated that motile microorganisms can use the nutrient gradient if their moveability range (the distance that they can swim during the age of a nutrient patch) is larger than the Batchelor scale. Moreover, the Batchelor length scale is essential in estimating the rate of dissipation of TKE that is explained in Chapter 3.

2.8.2 Kolmogorov length scale

The Kolmogorov scale L_K is the smallest hydrodynamic scale in turbulent flow at which turbulent kinetic energy is dissipated to heat by the effect of viscosity (Kolmogorov 1962). This scale is the smallest length scale of velocity fluctuations. Therefore this scale is a function of υ and ε. It is given by:

$$L_K = (\upsilon^3 / \varepsilon)^{1/4} \tag{2.11}$$

2.8.3 Displacement length scale

Turbulence has the potential to mix stratified water columns. Once turbulence happens the particle with larger density moves upward and is placed between particles with less density, or contrariwise. The vertical distance between the levels of a particle before and after mixing is called the displacement scale L_d (Thorpe 1977).

2.8.4 Centred displacement scale

The centred displacement L_c is an approximation of the overturn scale placed at the centre of the overturns. It is estimated by averaging the absolute value of half of the displacement scales (BOASHASH 1986; Saggio and Imberger 2001). This length scale is important to separate mean velocity from background velocities.

2.8.5 Thorpe length scale

The root mean squared of displacement scales represents the Thorpe scale L_T (Thorpe 1977). It is a simple estimate of overturn scales in stratified flow that can be calculated from density profiles (Mater, Schaad et al. 2013). If the mean horizontal density is smaller than the vertical gradient, then the Thorpe scale is a measure of mean eddy size (Dillon 1982).

2.8.6 Ozmidov length scale

In stratified water considering the effect of buoyancy, the possible large overturn scale is called the Ozmidov length scale L_o (Ozmidov 1965; Dillon 1982). In water columns with strong stratification, eddies larger than L_o are distorted. The Ozmidov scale is given by:

$$L_o = (\varepsilon / N^3)^{1/2} \tag{2.12}$$

2.8.7 Shear length scale

The larger scale in shear flow at which turbulence is affected is the shear length scale L_s. In other words, flow scales larger than the shear scale are deformed by shear (Smyth and Moum 2000; Bluteau, Jones et al. 2011). This scale is given by:

$$L_s = (\varepsilon / S^3)^{1/2} \tag{2.13}$$

3

Estimation of the rate of dissipation of turbulent kinetic energy

Estimating the rate of dissipation (ε) of kinetic energy can provide invaluable information about turbulence. The intensity of diapycnal mixing can be indirectly calculated from ε as the determination of dissipation is more convenient than measuring turbulent fluxes directly. Energy dissipation can be estimated from microstructure measurements. Different approaches have been proposed to determine dissipation based on temperature and velocity microstructure measurement. Some assumptions were used to derive these methods. In this chapter, the results of ε that were estimated using three different methods, are presented. Firstly, the Batchelor dissipation method was used to estimate energy dissipation. It is one of the widely used methods in which a Batchelor theoretical spectrum is fitted to a measured temperature gradient spectrum. Secondly, the inertial subrange method was applied. The rate of dissipation of turbulent kinetic energy can be estimated by fitting the Kolmogorov -5/3 slope to the velocity spectrum in log-log spaces. This method is based on single-point velocity measurement. Thirdly, the shear microstructure dissipation (shear dissipation) method was used. The method uses measured velocity strains to represent energy dissipation. Finally, the results from the three approaches were compared to each other. It was concluded that provided there is a good fitting in the Batchelor method and the presence of the inertial subrange in second technique, dissipation from these methods agreed well. Moreover, comparison of Batchelor dissipation and shear dissipation verified the accuracy of shear dissipation. While there are some limitations in using the first two methods, shear dissipation can be widely used to estimate the rate of dissipation of turbulent kinetic energy.
.

3.1 Introduction

According to turbulent cascade, large overturn scales transfer their energy to small scales through intermediate scales called inertial subrange. In the small scale (Kolmogorov scale), viscosity dissipates turbulent kinetic energy in an irreversible action to heat, resulting in irreversible fluxes of heat, nutrient, mass, and contamination (Thorpe 2007). The rate of dissipation of kinetic energy (ε) controls mixing and turbulent fluxes (Bluteau, Jones et al. 2011). So, vertical mixing can indirectly be determined from the rate of dissipation of TKE. In huge numbers of numerical models, closure schemes for vertical mixing are based on the calculation of the dissipation rate (Burchard and Petersen 1999). The ε can be a key parameter for comparing different numerical models in terms of accuracy in balancing the TKE. Quantitatively, estimation of energy dissipation can be directly considered as the production of TKE changes the potential energy of water columns(Kocsis, Prandke et al. 1999). Therefore, a comparison between potential energy before mixing and after mixing presents the rate of dissipation of TKE. Further, the direct relationship between energy dissipation and the sustainability of the aquatic environment has been confirmed in various scientific studies. For example, (Huang, Lenain et al. 2012) studied the importance of the dissipation of turbulent kinetic energy to sustain a coral reef in shallow water. They stated the crucial role of energy dissipation on reef morphology, microorganism distribution, and nutrient uptake by the coral reef community. The effect of currents on bottom friction caused a fully mixed bottom boundary layer in which maximum nutrient uptake by biota is proportional to $\varepsilon^{1/4}$ (Hearn, Atkinson et al. 2001; Falter, Atkinson et al. 2004).

One may ask the question: why are closure schemes for vertical mixing in many models and studies built on measurement of the rate of dissipation of turbulent kinetic energy? The answer is clear, as the estimate of the energy dissipation and then, indirectly, calculation of turbulent fluxes, is easier to do than direct measurements of vertical mixing and buoyancy fluxes.

Dissipation is calculated using different approaches. For example, in the field it can be estimated from velocity strain measured by a falling instrument, Bactchelor method (Luketina and Imberger 2001), and the application of the inertial subrange method to measured velocity spectra (Bluteau, Jones et al. 2011). Although the

mentioned methods are widely used to calculate the rate of energy dissipation, difficulty arises as all nine components of the dissipation tensor cannot be measured. Assumption of the isotropy of turbulence is the key solution to this issue (Itsweire, Koseff et al. 1993). Once all nine components of the dissipation tensor are estimated, the real value is attained. Direct numerical simulation (DNS) (Itsweire, Koseff et al. 1993; Herring and McWilliams 2006; Druzhinin, Troitskaya et al. 2012) and three-dimensional particle image velocimetry (PIV) (Saarenrinne and Piirto 2000; Burchard, Craig et al. 2008; De Jong, Cao et al. 2009) have the ability to estimate all nine velocity strains. However, these approaches have some limitations such as the difficulty of application of PIV in the field.

The objective of this chapter is to examine the performance of the three different approaches to estimate the rate of dissipation of turbulent kinetic energy. Further, the results from these three methods (Batchelor curve fitting, inertial subrange and velocity strains (shear dissipation)) are compared. Eventually, one of these methods is chosen for the rest of the study for estimating the dissipation rate of turbulent kinetic energy.

3.2 Batchelor Dissipation

3.2.1 Introduction

Numerous studies (Gregg 1977; Dillon and Caldwell 1980) (Grant, Hughes et al. 1968; Elliott and Oakey 1976; Marmorino and Caldwell 1978) (Kocsis, Prandke et al. 1999) have been conducted to use a theoretical Batchelor spectrum (Batchelor 1959) in natural waters. In this method, dissipation is estimated by fitting a theoretical spectrum (Batchelor spectrum) to the observed temperature gradients spectrum (Luketina and Imberger 2001). The range of high wavenumber of one-dimensional temperature gradients is a function of the energy dissipation and temperature variances χ_T (Luketina and Imberger 2001). To use this method, the presence of isotropic and homogenous turbulence and a clearly viscous convective inertial subrange is necessary.

To achieve an appropriate fit, different approaches have been conducted. For example, a graphical method in which a non-dimensional Batchelor spectrum fits to

temperature gradient signals, proposed by (Stewart and Grant 1962) or nonlinear least squares for fitting proposed by (Dillon 1982). Although the techniques are different, the objective is to get the Batchelor wavenumber. The Batchelor wavenumber has a direct relationship to the rate of dissipation. However, difficulty in knowing the exact response frequency of temperature sensors, limitations in sensor frequency range, contamination of signals with noise, and the effects of internal waves on the lower band of wavenumber domain (Gregg 1977; Dillon and Caldwell 1980) are ongoing challenges of these methods. Moreover, with an appropriate curve fitting it is very important to know what portion of fits should be used or how χ_T can be determined from the observed spectrum (Luketina and Imberger 2001). Here the method applied by (Luketina and Imberger 2001) is used to estimate Batchelor dissipation.

3.2.2 Method

(Batchelor 1959) proposed a temperature gradient wavenumber spectrum in a high Reynolds number, isotropic and homogenous turbulence. Using Batchelor's results by (Gibson and Schwarz 1963), they presented the one-dimensional Batchelor spectrum $S(k)$:

$$S(k) = \frac{\chi_T}{2D_T} \frac{(2q)^{0.5}}{k_B} S_N(\alpha) \qquad (3.1)$$

where k is wavenumber (radm^{-1}) , q is a universal constant assuming 2($3^{1/2}$), k_B is the Batchelor wavenumber. If the Batchelor length scale is inversed then wavenumber can be estimated. Batchelor scale is given by:

$$L_B = (D_T^2 \upsilon / \varepsilon)^{1/4} \qquad (3.2)$$

D_T is the diffusivity of heat , $\alpha = (2q) k k_B^{-1}$ is a dimensionless wavenumber, and $S_n(\alpha) = \alpha \left[e^{-\alpha^2/2} - \alpha \int_\alpha^\infty e^{-x^2/2}\, dx \right]$ is the normalized spectrum. By fitting the theoretical spectrum given by equation (3.1) to the measured spectrum and an approximation of the temperature variance, the only remaining variable is the Batchelor wavenumber which turns Batchelor dissipation (ε_B).

Knowing the Batchelor-like portion of the measured temperature gradient spectrum,

and fitting the theoretical spectrum to this part, χ_T can be estimated as:

$$\chi_T = 6D_T\left[\int_0^{k_L} S(k)\,dk + \int_{k_L}^{k_n} D(k)\,dk + \int_{k_n}^{\infty} S(k)\,dk\right] \tag{3.3}$$

where $D(k)$ is measured spectrum, k_L is an estimate of the lowest wavenumber of $D(k)$, and k_n is the noise wavenumber. The value of k_L is estimated by an iterative algorithm. Before the first turn it is assumed to be the minimum wavenumber of $D(k)$. During the subsequent trials k_L is set to the intersection of $D(k)$ and the best fit of $S(k)$. The noise wavenumber is fixed to the minimum wavenumber of the observed spectra. It is assumed that the value should be larger than 30 m^{-1} to ensure that a suitable minimum wavenumber has been selected. With an assumption for χ_T, the theoretical spectrum can be fitted to the observed spectra so the Batchelor wavenumber is estimated. To find out the right part of the observed spectrum, a trial and error method for all possible portions of the spectrum is considered and repeated six times for the entire spectrum(Luketina and Imberger 2001). In each turn the value of the noise wavenumber and the rate of dissipation of the temperature gradient are refined. A nonlinear curve fitting is used to determine the acceptable fit of the theoretical spectrum to the measured spectra. However, the outcome of this method is a local solution. Moreover, this approach is computationally demanding. To overcome this issue, about 200 geometrically interval values of the Batchelor wavenumber are examined, such that ε varies between 10^{-12} and 10^{-4} m^2s^{-3}(Luketina and Imberger 2001). By applying this method, it is accepted that the result is a Batchelor wavenumber with the least error. Using the Batchelor wavenumber, Batchelor dissipation can be estimated using $\varepsilon = (2\pi)^4 \nu D_T^2 k_B^4$.

Log-log space is used for curve fitting, as the roll-off region is clearly well defined compared to a liner-linear format (Luketina and Imberger 2001). In the fitting procedure, it is essential that at least the peak of the spectrum and the initial portion of the roll-off section are contained in the fitting. Moreover, the wavenumber of the data in which fitting is applied must have at least a span of one decade.

3.2.3 Results

Figure 3.1 shows a Batchelor fitting for a profile of a temperature gradient taken in the Swan River Estuary at 07:57 am on 8 October 2012. This profile has two stationary temperature gradient segments. Fig.3.1 shows proper fittings for both segments, where both the peak and initial roll-off regions have been covered by theoretical spectra. Moreover, there is a sufficient range of wavenumbers in the measured data to estimate the Batchelor dissipation. Although the effect of fine scale contamination in low wavenumbers is observed in both segments, the algorithm has ignored the contamination to achieve a good fitting. Theses segments have not been contaminated with noise in high wavenumbers. The rates of energy dissipation (Batchelor dissipation) for these two segments can be used for further calculations.

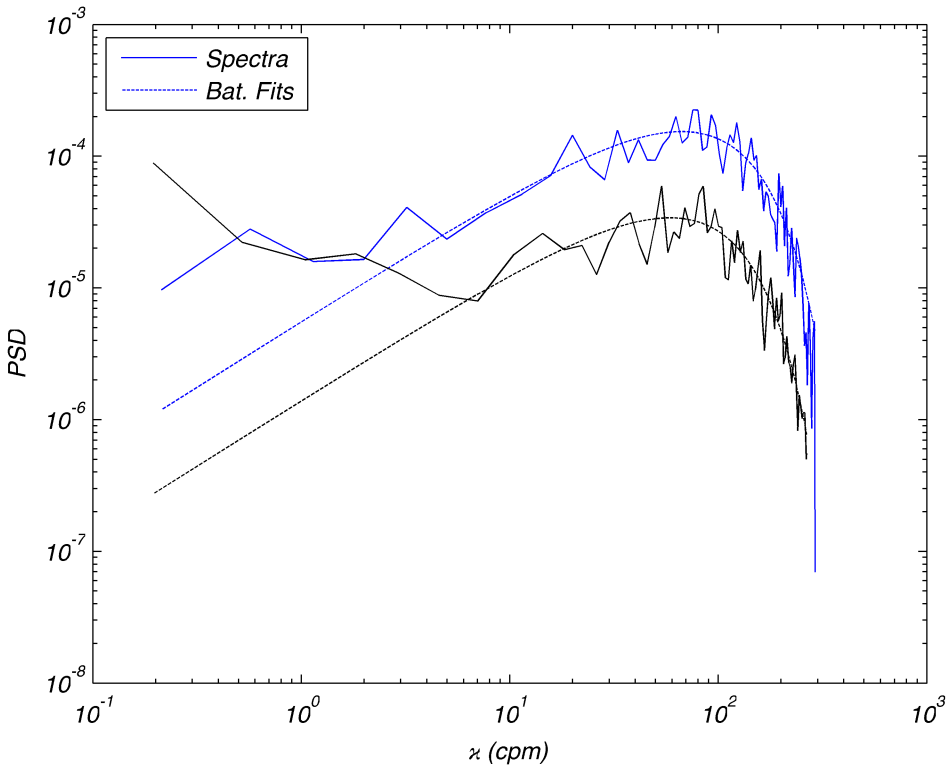

Figure 3.1 Measured temperature gradient spectra (solid line) and fitted theoretical Batchelor spectra (dashed line) for a profile taken in the Swan River on 8 October 2012 at 07:57 am.

The temperature profile, temperature gradient, and logarithmic value of the Batchelor dissipation corresponding to the first figure are presented in Fig.3.2. The first stationary temperature gradient segment extends from 1 m below the surface to a depth of about 4.70 m, with a dissipation rate of about 7.8×10^{-7} m^2s^{-3}. The adjacent segment extends from a depth of about 4.8 m to the bottom, with Batchelor dissipation rate of about 7.8×10^{-7} m^2s^{-3}. These two segments almost cover the entire water column, where the difference in temperature between the top layers and bottom layers is not very big. However, the background stratification is acceptable for algorithms to determine the rate of dissipation.

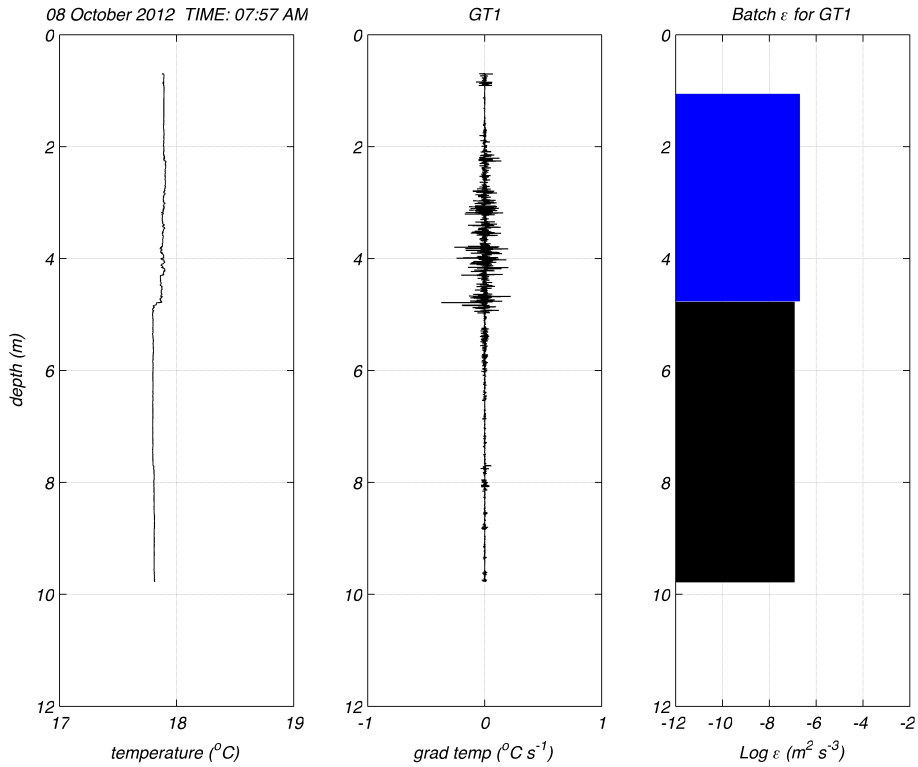

Figure 3.2 Temperature, temperature gradient, and logarithm of Batchelor dissipation for a profile taken in the Swan River on 8th October 2012 at 07:57 am.

A trial with an inappropriate fitting is depicted in Figure 3.3. The profile was recorded in the Swan River Estuary on 8 October 2012 at 09:14 am. It shows that the theoretical Batchelor spectrum is far from the measured temperature gradient spectrum. The algorithm could not properly fit the theoretical spectrum to the peak and initial part of the roll-off region in the measured spectra. Although a series of trial and error procedures were conducted, the algorithm was not successful. However, the method presented a value for dissipation. It is obvious that the rate of dissipation that resulted from this curve fitting must be discarded and cannot be used further.

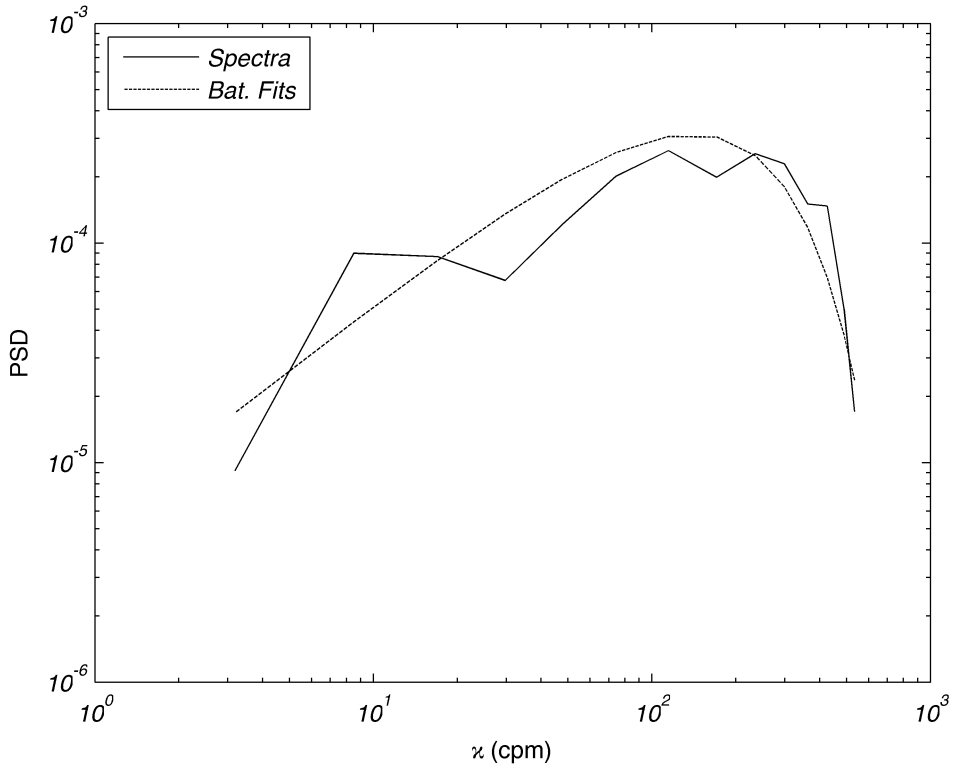

Figure 3.3 An inappropriate Batchelor curve fitting to temperature gradient profile measured in the Swan River Estuary on 8 October 2012 at 9:14 am.

3.3 Inertial subrange method

3.3.1 Introduction

One of the alternative approaches in measuring the rate of dissipation of kinetic energy is the inertial dissipation subrange method. To use this method, a measured single-point velocity is necessary; therefore, this method can be categorized into the 'convenient and cheap' approaches (Bluteau, Jones et al. 2011). Provided an accurate measurement of velocity is made, with some assumptions such as a homogenous and isotropic turbulence, the rate of dissipation of turbulent kinetic energy can be estimated by fitting the Kolmogorov -5/3 slope to the velocity spectrum in log-log domain. Allowing the Kolmogorov's hypothesis, if the wavenumber spectrum of three-dimensional velocity in a flow with high Reynolds number is depicted, a clear inertial subrange with slope of $-5/3$ should be observed. The inertial subrange depends only on the energy dissipation (Burchard, Craig et al. 2008). The inertial subrange is a middle range of turbulent scales in which wavelengths are smaller than energy containing overturns but bigger than Kolmogorov's scale. In the inertial subrange, the energy supplied from large overturns is balanced with energy converting to smaller scales, where it is converted to heat. The advantage of this method is that with a single velocity component in one direction, the rate of dissipation can be estimated. To apply this method, the time series of velocities in the frequency domain should be converted to a wavenumber domain. The upper and lower part of the inertial subrange changes with flow conditions. The high wavenumber end of the inertial subrange depends on both dissipation and mean velocity. Both shear and buoyancy anisotropy (Saddoughi and Veeravalli 1994) reduce the extent of the inertial subrange (Bluteau, Jones et al. 2011). Therefore, finding the inertial subrange is the major challenge of this method.

3.3.2 Methodology

Assuming an isotropic turbulence in a natural flow with a high Reynolds number, the inertial subrange of the energy spectrum (E_{jj}) for each single velocity component j is given by:

$$E_{jj}(k) = A_j C\varepsilon^{2/3}k^{-5/3} \quad (3.4)$$

where C is the Kolmogorov universal constant (Sreenivasan 1995), and is usually assumed to be 1.5, k is the wavenumber, and A_j is a constant related to the velocity component, where $j = 1,2,3$ (Pope 2000). For the longitudinal direction (mean advection) $A_1 = 18/55$, and for other directions (perpendicular to mean advection and vertical direction) $A_2 = A_3 = 1.33A_1$ (Bluteau, Jones et al. 2011). Using the theoretical energy spectrum (Eq. 3.4), the rate of dissipation is estimated. Similarly to the Batchelor method, here again the procedure is to fit the theoretical energy spectrum (E_{jj}) to the observed spectra (D_{jj}) of measured velocity profiles. All fittings occur within the stationary temperature gradient segments. As previously mentioned, time series of velocity profiles are in the frequency domain while frequency has to be converted to the wavenumber domain to estimate the dissipation. Using the mean velocity in the longitudinal direction ($\overline{v}_1$) and invoking Taylor's frozen hypothesis, the frequency domain is converted to the wavenumber domain via ($\overline{v}_1 \partial/\partial x_1 = \partial/\partial t$). The hypothesis is valid when $v_1^{'}/\overline{v}_1 \ll 1$, where $v_1^{'}$ is the longitudinal velocity fluctuations (Bluteau, Jones et al. 2011; Higgins, Froidevaux et al. 2012). When surface waves affect the turbulence, the modification must be applied to Eq. 3.4 (Lumley and Terray 1983; Burchard, Craig et al. 2008).

Provided there is a precise velocity measurement and isotropic turbulence, D_{jj} should present a distinct inertial subrange with a slope of about -5/3 in the log-log domain. In this method, dissipation can be estimated from each velocity component. Flow conditions determine the low and high wavenumber of the inertial subrange. It was previously mentioned that the inertial subrange is an intermediate range of length scales where the scale corresponding to a low wavenumber is smaller than energy containing scales, and the scale associated with a high wavenumber is much larger than the Kolmogrov scale. Theoretically, it is assumed that the high wavenumber bound is almost $k \approx 1/(10L_k)$ (Pope 2000). For the low wavenumber, two different scenarios are considered: either the influence of stratification or the effect of shear on the inertial subrange. In the stratified water, considering the effect of buoyancy, the large overturn scale is defined as the Ozmidov length scale. The effect of shear on turbulence is estimated by the shear length scale. (Bluteau, Jones et

al. 2011) re-examined the results of the study conducted by (Gargett and Holloway 1984) where they introduced the parameter $I = L_o / L_K$. This parameter defines the effect of stratification on the extent of the inertial subrange. Accordingly, if $I > 3000$ there is a clear inertial subrange for all three components of velocity with at least 1-2 decades extension; theoretically the inertial subrange spans in the range of $3/L_o < k < 1/(10L_K)$. When $600 < I < 900$ anisotropy affects the inertial subrange at the low wavenumber for D_{22} and D_{33}; however, mean advection velocity presents an obvious bound for the inertial subrange. The inertial subrange at a low wavenumber is lost even for D_{11} when $200 < I < 300$. In this circumstance, the application of the inertial subrange method provides unreliable results. The effect of shear on the inertial subrange is introduced by $B = L_s / L_K$. $B > 3000$ (Saddoughi and Veeravalli 1994) means there is a clear inertial subrange for all three velocities with two decades range between the low and high wavenumber. (Bluteau, Jones et al. 2011) examined the results of (Saddoughi and Veeravalli 1994) to understand the effect of anisotropy that resulted from shear. For $B \simeq 950$, there is more than one decade of the inertial subrange for D_{11}, and less than one decade for other velocity components. When $B = 350 - 430$, D_{11} shows about one decade of inertial subrange. While D_{33} presents a half decade of inertial subrange, D_{22} does not have any inertial subrange. For a detailed description please see (Bluteau, Jones et al. 2011).

Energy dissipation within a temperature gradient stationary segment is estimated based on using the inertial subrange method. To achieve the best fit between the observed velocity spectrum and the theoretical spectrum, least square regression is used in the log-log wavenumber domain.

3.3.3 Results

Figure 3.4 shows the spectrum of longitudinal velocity for a profile measured with the PFP in the Swan River Estuary on 8th October 2012 at 9:14 am where the Batchelor dissipation method could not estimate the energy dissipation (Figure 3.3). Calculation shows that $B = 380$; therefore, there should be about one decade of inertial subrange for D_{11}. Using the linear least square fitting to fit a $-5/3$ theoretical slope to the measured spectrum, black dots show the best fitting. Figure 3.4 shows a distinct inertial subrange for this particular profile. The inertial subrange dissipation is $\varepsilon = 3\times10^{-7}$ m^2s^{-3}. However, there is not a clear inertial subrange for the spectrum of lateral velocity D_{22} (Figure 3.5). We have to show the spectrum for longitudinal velocity and transverse velocity in two separate figures, in order to show more detail of the fitting process.

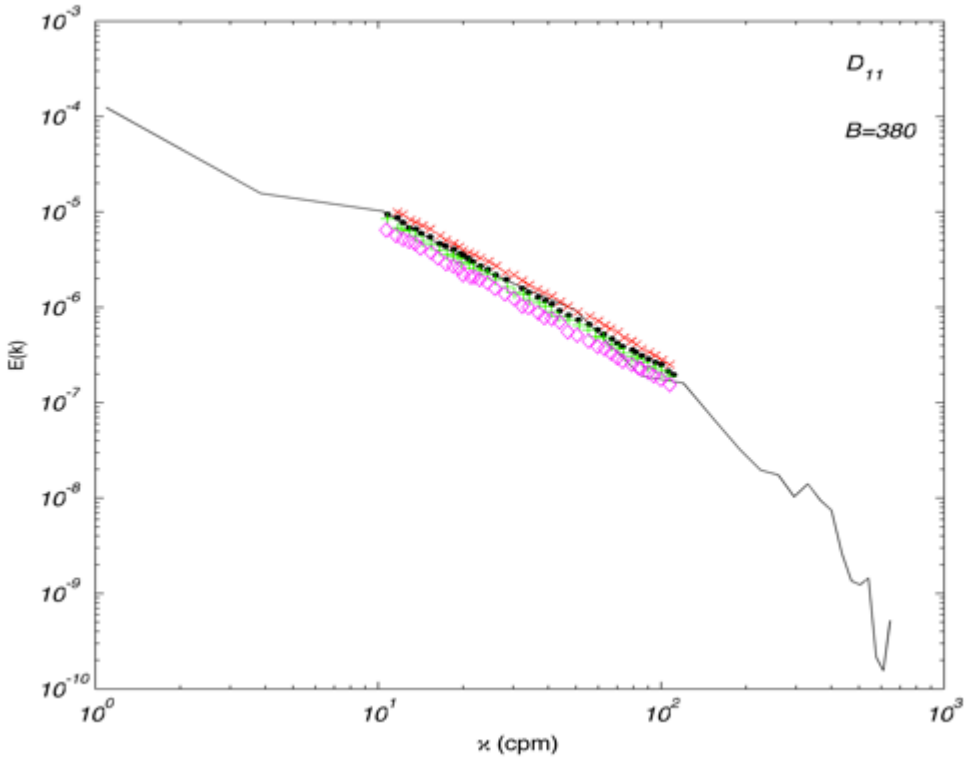

Figure 3.4 Spectrum of longitudinal velocity measured with PFP in the Swan River Estuary on 8 October 2012 at 9:14 am, B=380.

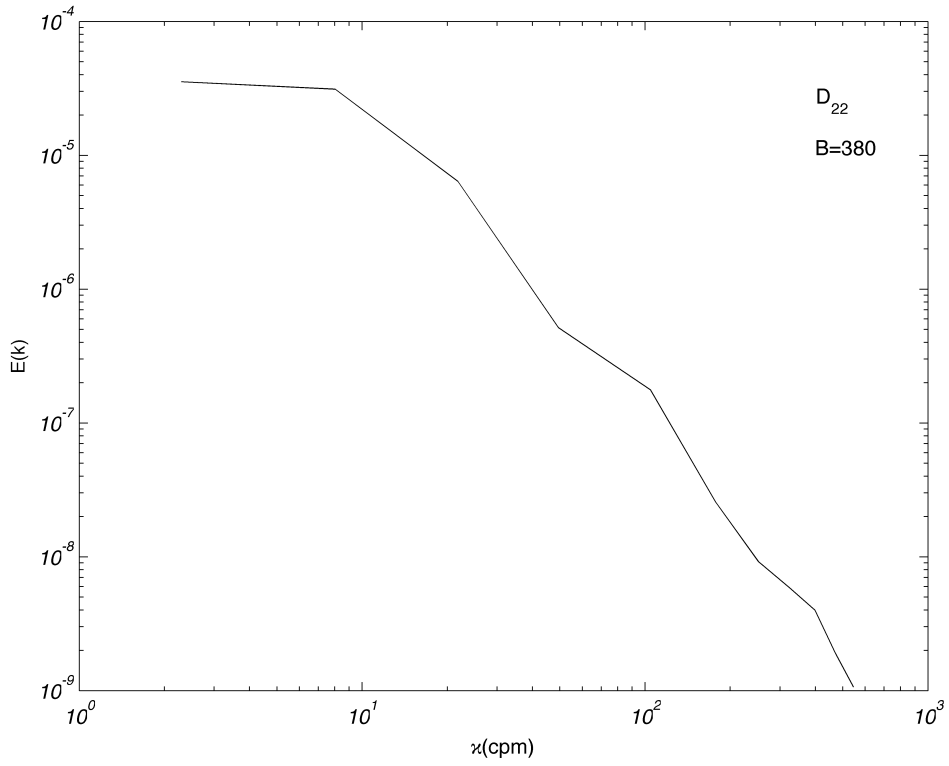

Figure 3.5 Spectrum of lateral velocity (perpendicular to mean advection velocity) measured with PFP in the Swan River Estuary on 8 October 2012 at 7:57 am, B=380.

Figure 3.6 presents the spectrum of longitudinal velocity for the second temperature gradient stationary segment (see Figure 3.2) recorded with the PFP in the Swan River Estuary on 8 October 2012 at 07:57 am. It shows a clear inertial subrange. Further, three different parts of the turbulent length scales are shown on this figure. The first part belongs to energy containing scales where turbulence is fed from large scales. The second region is the inertial subrange part where turbulent kinetic energy transfer to turbulence has become balanced with the rate of dissipation of energy. Finally, there is the region where turbulent kinetic energy is converted to heat in an irreversible procedure. Figure 3.6 shows clearly the lower and higher wavenumber bounded to the inertial subrange. According to the figure, the low wavenumber is smaller than energy containing length scales. The length scale associated with the high wavenumber at the end of the inertial subrange is about 10 times smaller than the Kolmogorov scale. Dissipation value for this segment is $\varepsilon = 7.6 \times 10^{-7}$ $m^2 s^{-3}$.

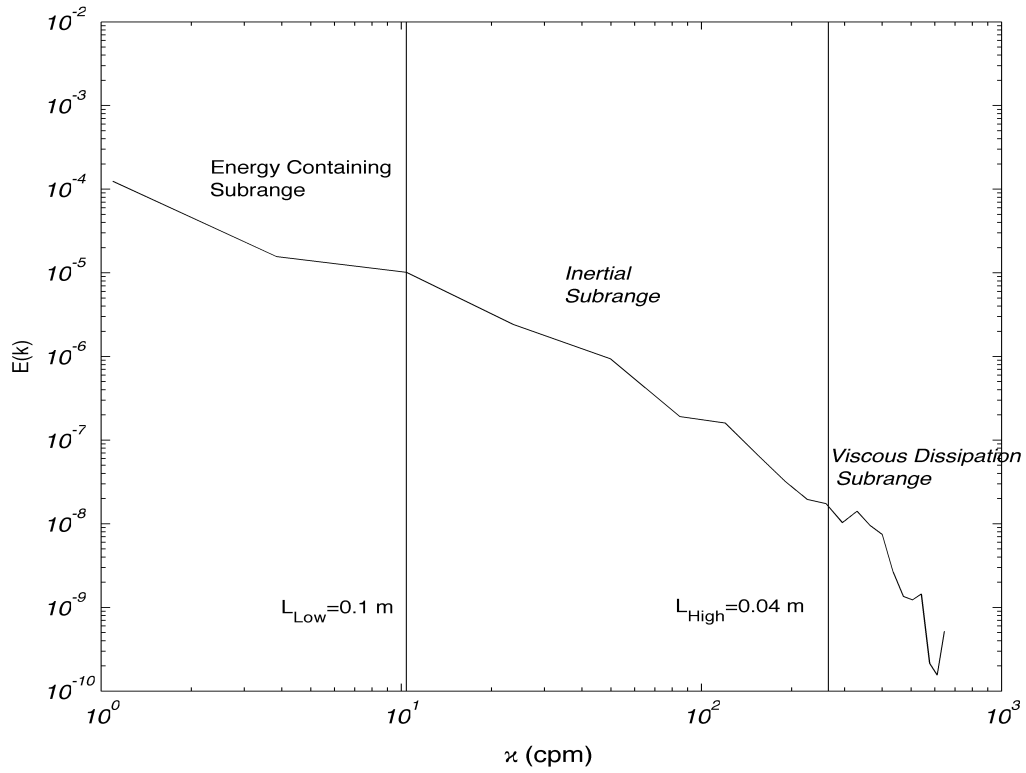

Figure 3.6 Spectrum of mean velocity advection for second stationary segment (see Figure 3.2) taken in the Swan River Estuary on 8 October 2012, at 7:57 am.

3.4 Shear Microstructure Dissipation (Shear dissipation)

3.4.1 Introduction

Shear microstructure dissipation (ε_s) is one of the other techniques in which dissipation of turbulent kinetic energy in natural stratified waters is estimated. As for the Batchelor approach in this method, having the microstructure measurement is necessary. While the Batchelor method relies on temperature gradient microstructure, the shear dissipation method is based upon velocity microstructure. Assuming an isotropic turbulence, the rate of dissipation can be estimated from small-scale shear fluctuations $\partial v' / \partial x_3$ (Gregg 1991; Kocsis, Prandke et al. 1999). Although some studies related to turbulence have been conducted in the Swan River Estuary (Etemad-Shahidi and Imberger 2002; Etemad-Shahidi and Imberger 2002; Etemad-Shahidi and Imberger 2005), the rate of dissipation of kinetic energy was calculated

based on temperature gradient microstructure. Here the rate of dissipation of turbulent kinetic energy is estimated based on small-scale shear fluctuations.

3.4.2 Methodology

Provided there is a homogenous and isotropic turbulence, (Piccirillo and Van Atta 1997) proposed an equation to estimate the rate of dissipation of TKE based on the measured velocity microstructure. Using the three measured velocity strains, dissipation is given by:

$$\varepsilon_s = \upsilon[5\overline{(\partial v_3^{'} / \partial x_3)^2} + 5/2\overline{(\partial v_1^{'} / \partial x_3)^2} + 5/2\overline{(\partial v_2^{'} / \partial x_3)^2}] \qquad (3.5)$$

where the bars denote ensemble averages.

To use this method, absolute velocity (flow velocity) is filtered with a non-recursive Guassian filter. The length of the non-recursive filter is 31 samples. As the PFP has a vertical resolution of about 1 mm in the vertical, therefore filtering is performed on a vertical space of about 3 cm. The output of this non-recursive filter is a time velocity gradient. Invoking Taylor's frozen hypothesis converts the time gradient quantity to a space gradient. To do that, the drop velocity of the instrument for each data point is invoked. To overcome the difficulty of the non-stationary nature of turbulence, the velocity fluctuation strain should be presented within each temperature gradient stationary segment. The shear microstructure dissipation is determined by using Eq. 3.5.

3.4.3 Results:

Figure 3.7 shows energy dissipation that resulted from the shear microstructure dissipation method. For consistency with Batchelor dissipation, we used microstructure velocities taken in the Swan River Estuary at 07:57 am on 8 October 2012. There are some local maxima and minima within the water column for both $dv_1^{'}/dx_3$ and $dv_2^{'}/dx_3$. However, the maximum for both $dv_1^{'}/dx_3$ and $dv_2^{'}/dx_3$ happens in the surface layer of about 1 s^{-1}. Moreover, $dv_2^{'}/dx_3$ shows a significant maximum at the bottom of the water column. The maximum of $dv_3^{'}/dx_3$ happens at the bottom with a value of about 0.8 s^{-1}. The first stationary temperature gradient segment (upper segment) has a dissipation rate of about $\varepsilon=7.9\times10^{-7}$ m^2s^{-3}. The shear dissipation for the second temperature gradient segment was $\varepsilon=7.8\times10^{-7}$ m^2s^{-3} (Figure 3.7)·

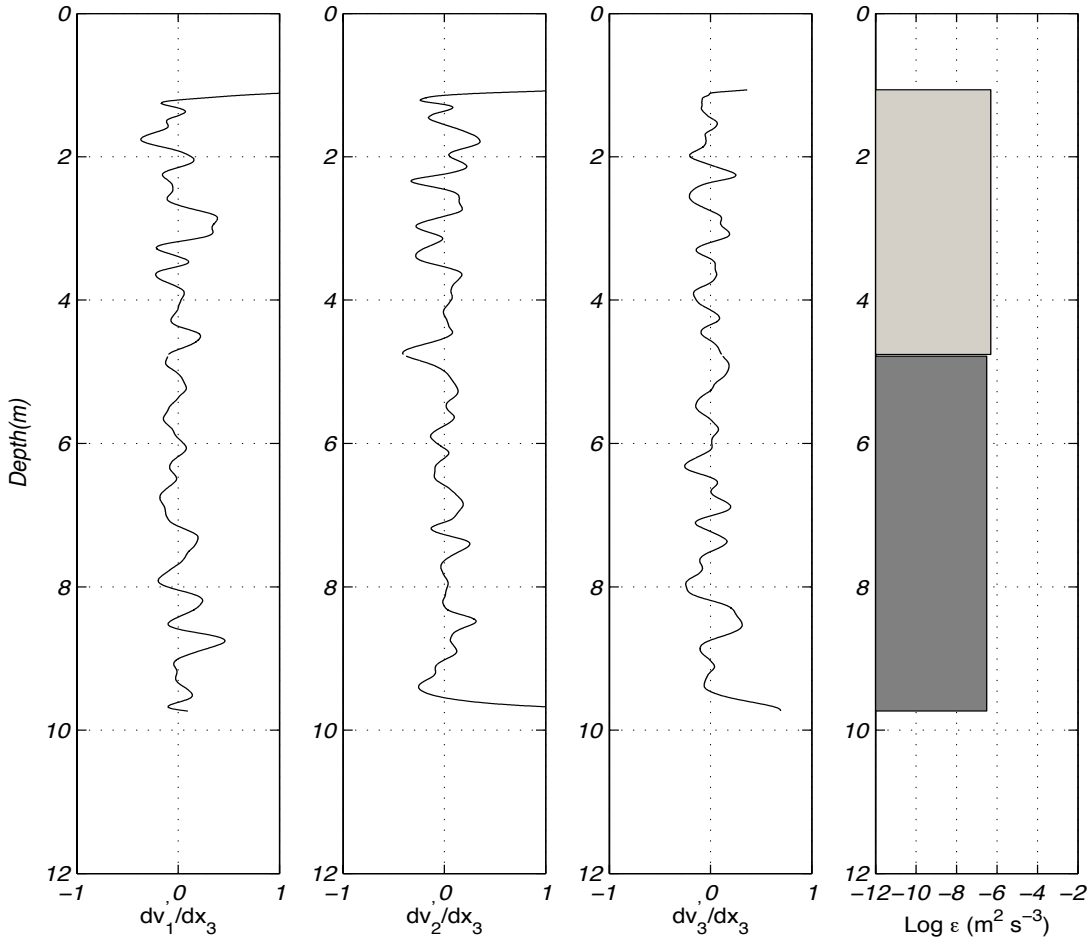

Figure 3.7 Shear microstructure fluctuations and logarithm of shear dissipation for a profile taken in the Swan River on 8 October 2012 at 07:57 am.

The shear dissipation for a profile measured with the PFP on 8 October 2012 at 9:14 am in Swan River Estuary is presented in Figure 3.8. Shear microstructure for both horizontal velocities present a minimum at the surface and a maximum at the bottom of the temperature gradient segment. $dv_3^{'}/dx_3$ does not show a significant event through the entire water column. The Batchelor dissipation method could not appropriately fit the theoretical spectrum to the observed spectrum. However, using the shear dissipation method, the rate of dissipation of kinetic energy is $\varepsilon = 7.1\times10^{-7}$ m^2s^{-3}.

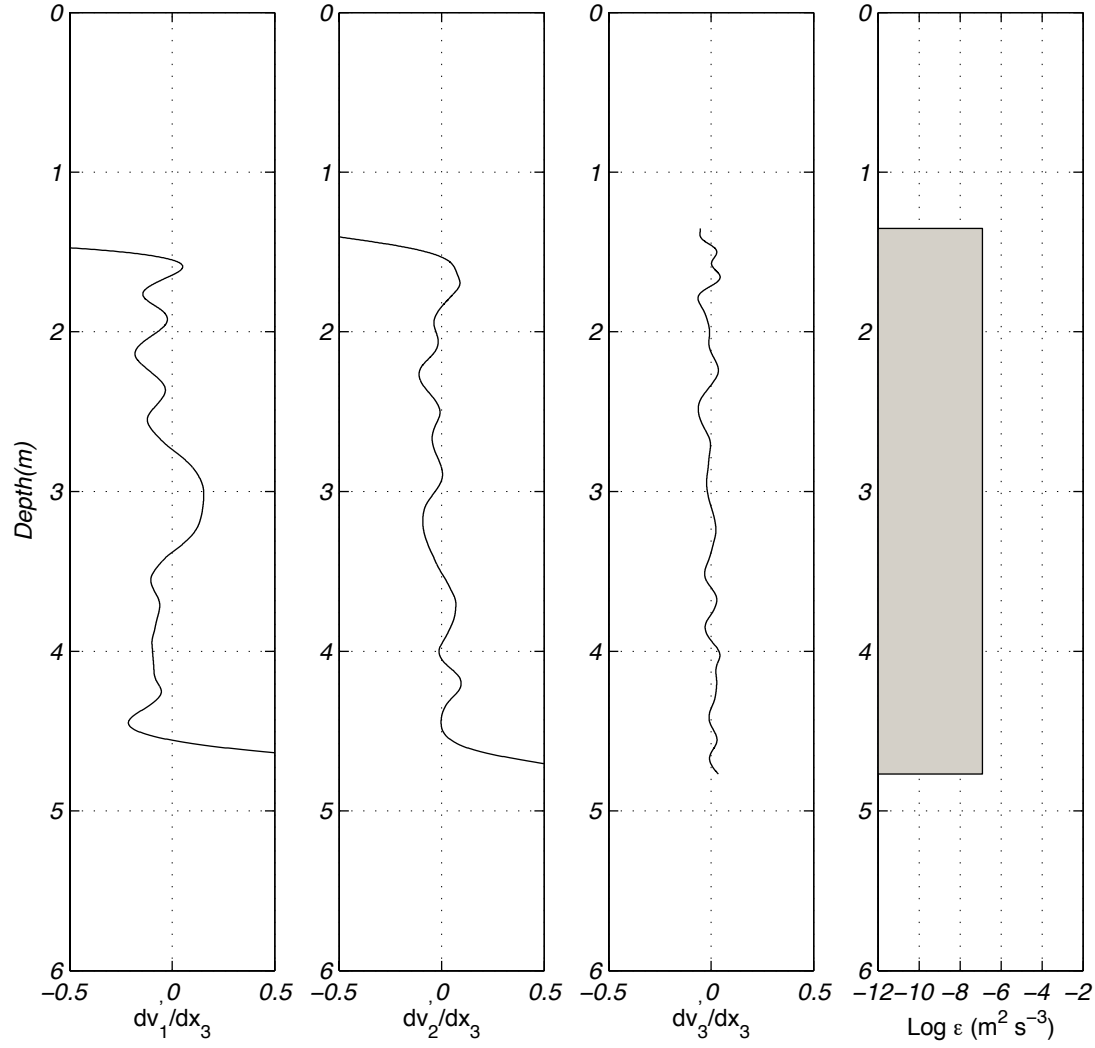

Figure 3.8 Shear microstructure fluctuations and shear dissipation for a profile measured with the PFP in the Swan River Estuary on 8 October 2012 at 9:14 am.

3.5 Discussion

If the effects of sensor errors, internal waves and other interfering factors are eliminated, the Batchelor method provides accurate results (Luketina and Imberger 2001). However, this approach needs an extra visual investigation in which the inappropriate fittings must be discarded. Therefore, one might lose many of the stationary segments that might be essential for further studies. The inertial subrange method has its limitations. As previously mentioned, buoyancy and shear might cause a reduction of the extent of the inertia subrange. Further, this approach seems to be a time consuming method and sometimes it is not convenient to find a clear subrange. The microstructure shear dissipation method seems the only approach that can save both time and segments. As in the majority of studies, the rate of dissipation of kinetic energy has been estimated from Batchelor curve fitting; therefore, we compare two other alternatives with Batchelor dissipation (Figure 3.9). To achieve this objective, microstructure data collected in the Swan River Estuary was used. (Kocsis, Prandke et al. 1999) mentioned that due to several assumptions in the shear dissipation and Batchelor dissipation methods, there is no necessity that the two methods present the same dissipation. However, our findings show that, providing there is a good curve fitting method and accurate velocity measurement, Batchelor and shear dissipation methods yield close results (Figure 3.9a). Batchelor dissipation and inertial subrange results are compared in Figure 3.9b. These two methods show acceptable agreement. However, the inertial subrange method presents more scatter compared to shear dissipation. This can be explained by the effects of buoyancy or shear on the extent of the inertial subrange, where they act as limiting factors.

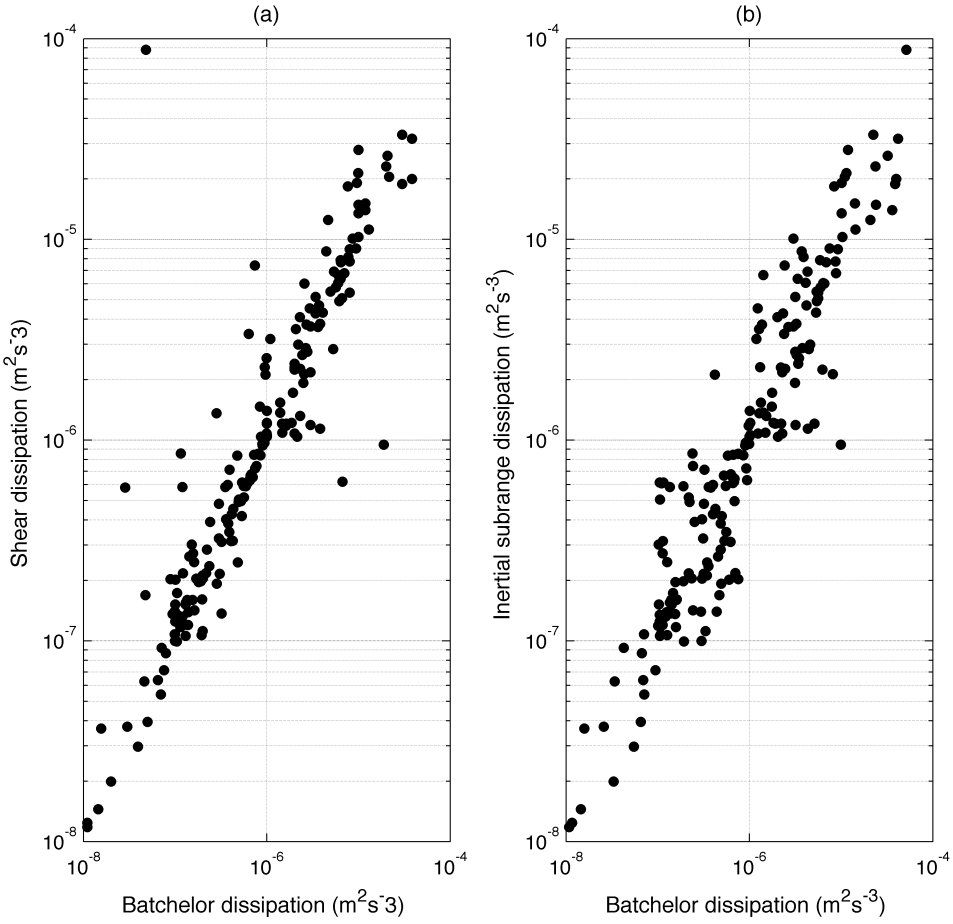

Figure 3.9 Comparison between three different approaches in estimating the rate of dissipation of kinetic energy. (a) Shear and Batchelor dissipation (b) Inertial dissipation and Batchelor dissipation

3.6 Summary

Three different approaches were used to estimate the rate of dissipation of kinetic energy (Batchelor, inertial subrange and shear dissipation methods). All these three methods are based on microstructure measurement: temperature microstructure for Batchelor dissipation and velocity microstructure for inertial and shear dissipation. To use these methods, some assumptions are considered, such as isotropic and homogenous turbulence. Results show that these methods yield almost the same results. However, shear dissipation shows less scatter than the inertial subrange method. Shear dissipation will be used for further calculations in this study.

4

Turbulence measurements In the Swan Estuary

The key factor in a good understanding of turbulence is accurate measurement of turbulent properties. However, direct measurements of turbulent fluxes are a tedious job. This is because turbulence is very chaotic and its properties change with time and space. Therefore field measurements of turbulent properties just present a snapshot of a certain time within the lifetime of turbulence evolution. Lab experiments and numerical simulations are two alternatives to direct measurements. Lab experimentation is one of the most useful methods. However, lab work has some limitations relating to the reality of natural waters. Numerical simulation itself is completely dependent on data. Provided there is the presence of proper data, the important question in modelling is how accurately a model can simulate the vertical mixing of a water body. Numerous closure schemes have been applied in numerical models. Their job is to present vertical mixing based on some measurable parameters in the field. Therefore one can imply two primary objectives of field measurements. Firstly, it is to provide input data for numerical modelling and secondly it is to examine or propose mixing closure schemes or study the vertical mixing in natural waters. To achieve these objectives, detailed descriptions of three field experiments on 27 August, 8 October, and 2 November 2012 in the lower part of the Swan River Estuary using the PFP are presented in this chapter. The first and second field trips were organized to provide necessary data for initial and validation conditions. Moreover, the last field trip was conducted to provide some supplementary data. The mean variables (salinity, temperature, dissolved oxygen, pH and turbidity) of the second field measurements are used to estimate the velocity field by the inverse method (Chapter 5). Moreover, measured turbulent variables are used to study vertical turbulent mixing (Chapter 6). Salinity contours showed stratification conditions with usually strong intensity in the upper part of the domain. The partially mixed thermal structure of the domain in first field trip was replaced with thermal stratification at the third field experiment. This verified that the study site undergoes a seasonal thermal stratification. From the first to the third field trip the dissolved oxygen concentration reduced due to an increase of algal bloom activity and a reduction of freshwater inflow to the river. The results of this study revealed that always there is an oceanward current during ebb tide, with the maximum velocity occurring during the ebb tide before the slack time. The maximum of the shear dissipation and the Reynolds number showed a direct relationship to shear values.

4.1 Introduction

Direct measurement of turbulence in the field provides a means to improve the knowledge of turbulence and the processes that control the vertical diffusion of water columns. However, direct measurement of turbulence is a tedious task because of the unsteady nature of turbulence. In other words, turbulence is highly variable in time and space. Accurate direct small-scale measurement of turbulence is crucial to studying the evolutionary state of turbulence. For example, the direct measurement of small-scale is very important to the ecology of aquatic environments. Microorganisms play an important role in aquatic chains. However they cannot exploit turbulence at eddies with large scales. This is due to the tiny size of bacteria. Therefore, microorganisms benefit from turbulence at a small scale, as their size is comparable to the Batchelor scale (Stocker 2012).

One of the other aspects of the science being indebted to direct measurements of turbulence is numerical modelling. In fact, field measurements support modelling advancement in two ways. Firstly, field measurements provide all the necessary input data for simulations. For example, to simulate a river one must have all the forcing variables such as wind, inflow and meteorological data with high accuracy. Further, the presence of validating data is crucial for the future interpretation of water bodies when study is going to be conducted using numerical models. Secondly, vertical mixing in numerical models is based on different turbulent closure schemes. A variety of closure schemes have been proposed to parameterize vertical mixing at resolved scales. However, accurate simulation of vertical mixing of water columns is still a challenging part of numerical modelling, as the models usually can not present the transient distribution of turbulent mixing at micro-scales (Yeates 2007). Moreover, the effects of numerical diffusion in modelling damage the accuracy of the simulation (Laval, Hodges et al. 2003). Most of these schemes are based on explicit representation of turbulence evolution (Simpson, Crawford et al. 1996). During turbulence evolution, the rate of production of turbulent kinetic energy available for mixing is equated with buoyancy fluxes and the energy dissipation (Umlauf and Burchard 2003; Souza 2007). As previously mentioned, the understanding of turbulence evolution is just possible with small-scale

measurements. Therefore, an accurate direct measurement of turbulent properties at small scales is very valuable to resolve the problem.

Etemad-Shahidi and Imberger (2005) used microstructure data collected in the Swan River Estuary to compare direct and indirect diapycnal diffusivity. Using the direct measurement data showed the disadvantage of the indirect method in estimating the negative buoyancy fluxes.

Simanjuntak et al. (2011) used temperature and velocity measurements to study mixing characteristics in benthic and interfacial regions of a shallow, tidal estuary during a period of maximum freshwater discharge via a barrage and high shear. They used the concept of percentage down-gradient flux to propose a new closure scheme based on gradient Richardson number as an alternative to a general mixing routine in an explicit mixing model for the 3-D estuary, lake and coastal ocean model (ELCOM) (Hodges 2000; Hodges, Imberger et al. 2000; Hodges and Imberger 2001; Dallimore, Hodges et al. 2003; Laval, Imberger et al. 2003; Hodges and Dallimore 2006). Then, based on the outcome of numerical simulations, they examined the performance of the new closure scheme. They concluded that the proposed closure performed better than the general closure scheme in stratified water.

Therefore, field measurement of turbulence properties such as turbulent velocity fluctuations, Reynolds stresses, the rate of dissipation of kinetic energy and buoyancy fluxes present valuable information in both the concept of turbulence and the design of new closures for turbulent mixing.

In this chapter, full descriptions of three microstructure measurements in the lower part of the Swan River Estuary are presented. The chapter was organized such that it provides initial data (first field trip), validation data (second field measurement) and some supplementary data (third microstructure measurement). These detailed data sets provide valuable information either for running a numerical model or the examination of turbulent closure schemes. Further, mean variables collected in the second field trip are used to estimate the velocity field by the inverse technique in Chapter 5. The turbulent fluxes presented in this chapter are used for the study of turbulent vertical mixing in Chapter 6.

The outcomes of each set of field measurements are categorized into four sections. Firstly, the background environmental conditions of that day are presented. Secondly, the spatial changes of mean variables such as salinity, temperature,

density, and dissolved oxygen are presented. For the validation data (second field study), both spatial and temporal changes of mean variables are presented in Chapter 5. Thirdly, contours of velocity are filed, including longitudinal velocity, shear, buoyancy frequency, and gradient Richardson number. Contours of turbulent properties such as the rate of dissipation of turbulent kinetic energy, Reynolds stresses, and buoyancy fluxes are given. So, all parts of the turbulent kinetic energy equation (Eq. 2.5) are directly measured. The results of this chapter will be used for studying vertical mixing in Chapter 6. Finally, the highlighted results are discussed and the chapter ends with a summary and conclusions.

4.2 Field measurements for initial conditions (on 27 August 2012)

4.2.1 Background environmental conditions

In this section a general review of tidal conditions, meteorological data such as wind, temperature, relative humidity and water temperature is presented. The first field sampling was carried out on 27 August 2012 when the estuary experienced spring tide conditions. Field measurement began at 07:40 am from the river mouth at Fremantle (Figure 2.2) and finished at 04:45 pm. During the period of study the sky was clear. Overall, 46 microstructure profiles of temperature, conductivity, dissolved oxygen and velocity were collected with the PFP. Moreover, some chemical and biological properties were measured that were not used for this study.

Figure 4.1a shows the changes in tidal level on 27 August relative to Australian Height Datum (AHD) recorded at the Fremantle tide gauge. The maximum water level of about 0.30 m happened at 06:15 am. The minimum water level of about -0.30 m was recorded at 03:15 pm. Throughout the period of sampling the range of difference in water levels was $0.54m$. Sampling was conducted during the ebb tide. The major part of the site is sheltered; therefore wind cannot affect the hydrodynamics of the domain, except for big events. Data from the LDS station showed wind conditions were generally calm over that day (Figure 4.1b). The biggest event was a wind with magnitude of about $1.78ms^{-1}$ that occurred at 06:30 pm.

During the sampling time a variable wind field was observed. The air temperature was recorded at the LDS. While the minimum atmospheric temperature was recorded at 06:45 am (11.5 $^{\circ}C$), the hottest time was measured at 03:00 pm (18.2 $^{\circ}C$) (Figure 4.1c).

Unlike the wind, the air temperature dramatically changed during the time of profiling (a range of about 6 $^{\circ}C$ was observed). Although there was a significant change in air temperature, water temperature was 16.67 $^{\circ}C$ at the commencement of sampling and changed to 17.74 $^{\circ}C$ at the end of profiling.

Relative humidity data collected at the LDS station during the period of study varied between 60 and 90 per cent. To present Figure 4.1, the data was averaged over 15-minute intervals.

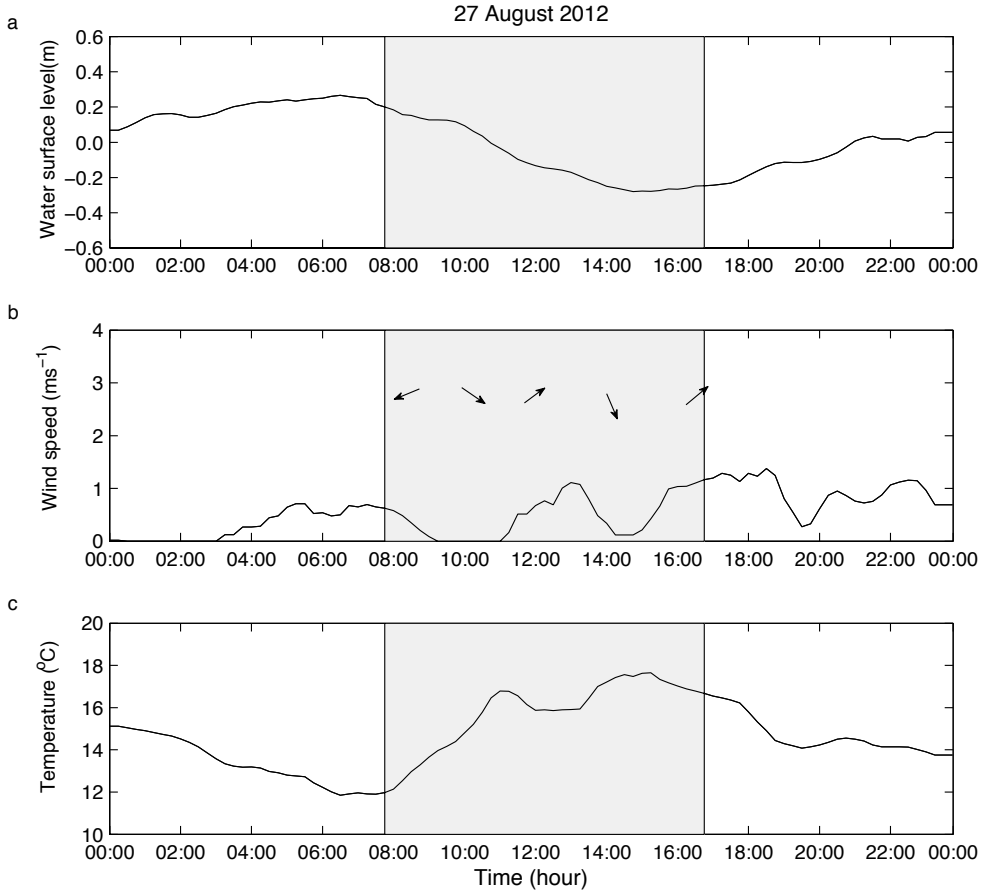

Figure 4.1 Water levels, wind speed (arrows show wind direction), and temperature recorded on 27 August 2012 in the lower part of the Swan River Estuary during spring tides. Shaded area shows the time at which the field measurement was conducted.

4.2.2 Mean Variables

In this section, contours of different variables such as salinity, temperature, density and dissolved oxygen that were collected with the PFP on 27 August are presented. It should be mentioned that as a convention, 'accumulated distance' means the distance of each profile relative to the lower boundary of the domain at Fremantle (Figure 2.2). The field measurement covered the entire duration of ebb tide; however, the first data sets that were collected during the first half period of ebb tide are presented here.

4.2.2.1 Salinity

The salinity contours showed strong stratification in the upper part of the domain and a weakly stratified water column in the lower part at Fremantle, as during the measurements fresh water from the upper part did not fill this area (Figure 4.2). Salt intrusion from the ocean at the bottom of the river mouth (Fremantle) was evident. In the other part of the river, discharging brackish waters from the upper Swan led to the presence of strong stratification. However, the vertical distance between isohaline contours in the surface layer was much less than at the bottom. The maximum salinity was observed in the bottom of the river mouth and the minimum salinity was recorded at the upper part of the domain. Figure 4.2 shows the relative distance of about 3.8 km is the boundary between strong and weak stratification (transient zone). The accumulated distance means the distance between the beginning of the domain at Fremantle to the station at which profiling was conducted.

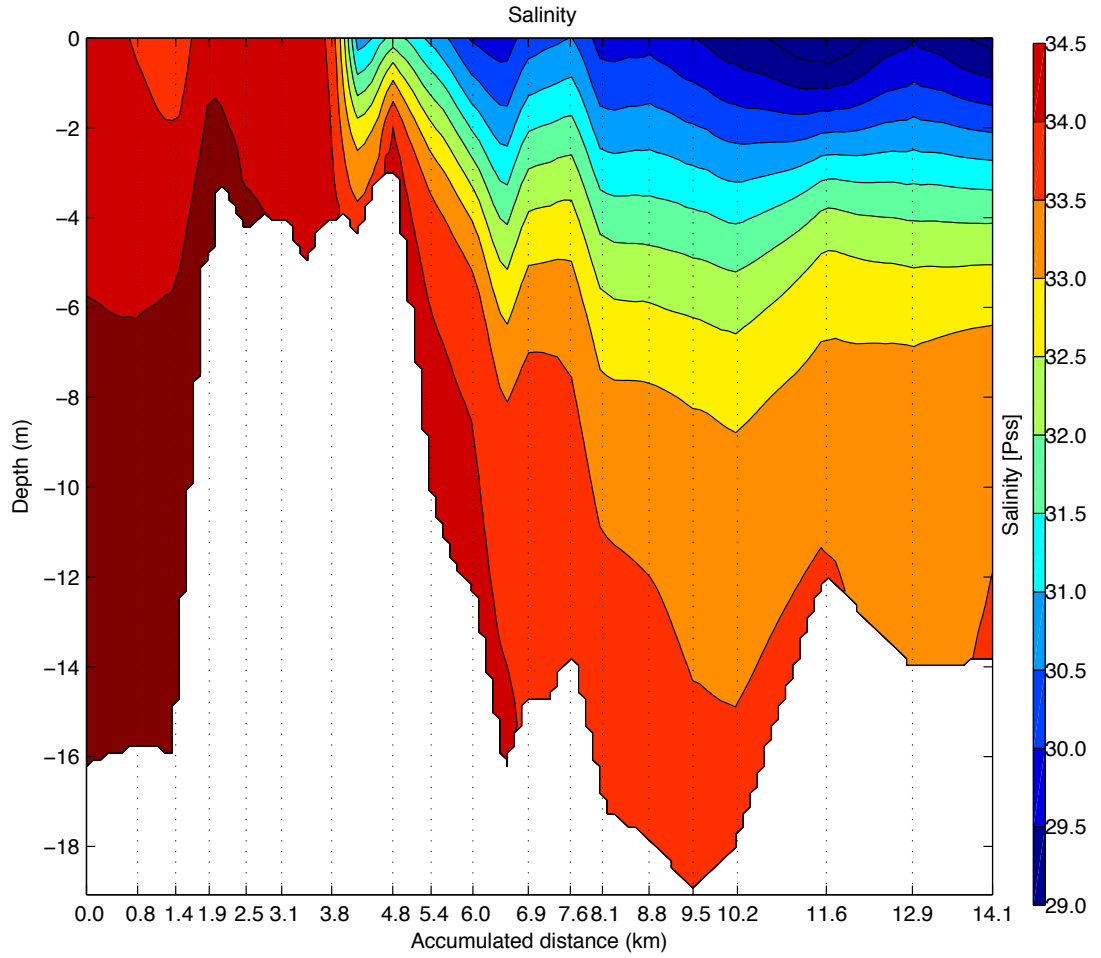

Figure 4.2 Salinity contours measured with the PFP on 27 August 2012 in the lower part of the Swan River Estuary.

4.2.2.2 Temperature

Unlike the salinity curtain, temperature profiles showed a very weak thermal stratification. The major portion of the site presented a well-mixed thermal structure. However, in some locations there was a difference of about (0.25 $^{\circ}C$) between the surface and the lower layer (weak thermal structure). At the transient zone between weak and strong stratification (accumulated distance of about 3.8 Km) due to salinity (Figure 4.2) there was a distinct water column with a temperature of about 17.25 $^{\circ}C$.

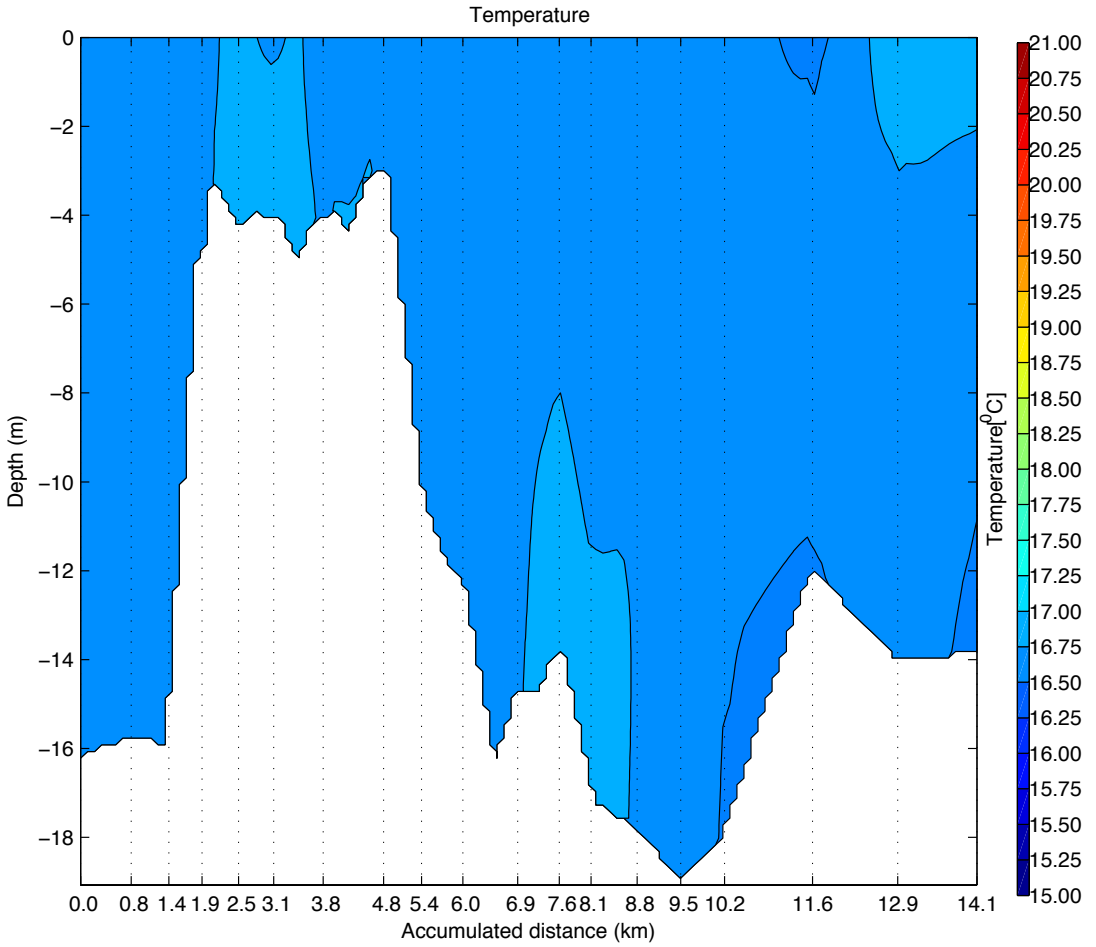

Figure 4.3 Temperature curtain recorded with the PFP on 27 August 2012 in the lower part of the Swan River Estuary.

4.2.2.3 Density

Density contours presented similar structures to salinity contours, where a strong stratification is dominant at the upper part of the domain and a weak stratification is evident in the lower part of the site. Although density is usually a function of temperature and salinity, the effect of temperature is negligible here. The difference between the lower density in the surface and greater density at the bottom was about 4 kgm^{-3}. The maximum density was observed at the river mouth (Fremantle) and water with least density was observed at the surface layer of the upper part of the domain.

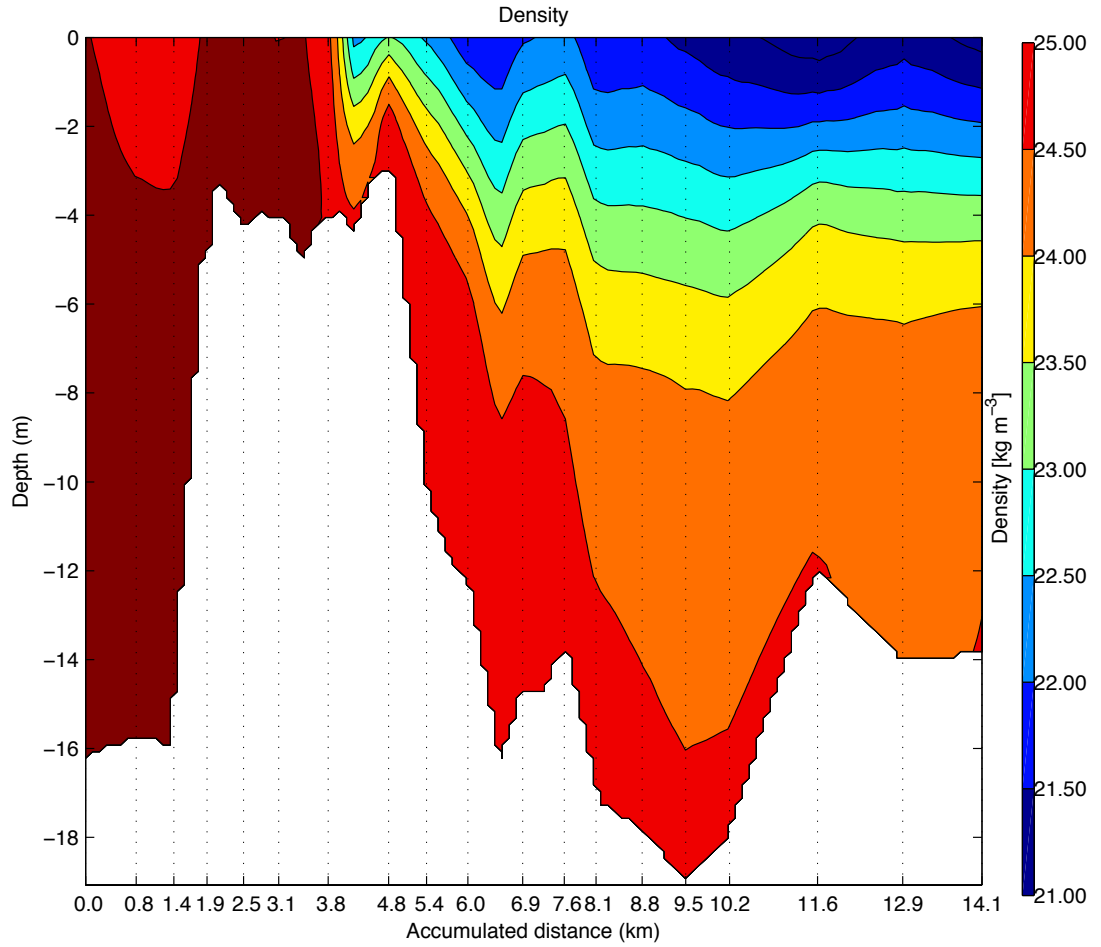

Figure 4.4 Density contours measured with the PFP on 27 August 2012 in the lower part of the Swan River Estuary.

4.2.2.4 Dissolved oxygen

While the maximum concentration of dissolved oxygen (9.20 mgl^{-1}) was in the surface layer, the minimum value (7.40 mgl^{-1}) was observed in the bottom layers, verifying that there was no quality issue such as an anoxia zone in the bottom layers. Maximum and minimum of dissolved oxygen was occurred in upper part of the domain and in surface and bottom layer, respectively. The occurrence of the maximum concentration of dissolved oxygen was consistent with the place of freshwater inflow from upstream (Figure 4.2). The location of the lower concentration of dissolved oxygen was in the deepest point of the estuary. The lower part of the domain showed fully-mixed layers of dissolved oxygen (8.40 mgl^{-1})

except a local area at the surface that had a dissolved oxygen concentration of about (8.60 mgl^{-1}).

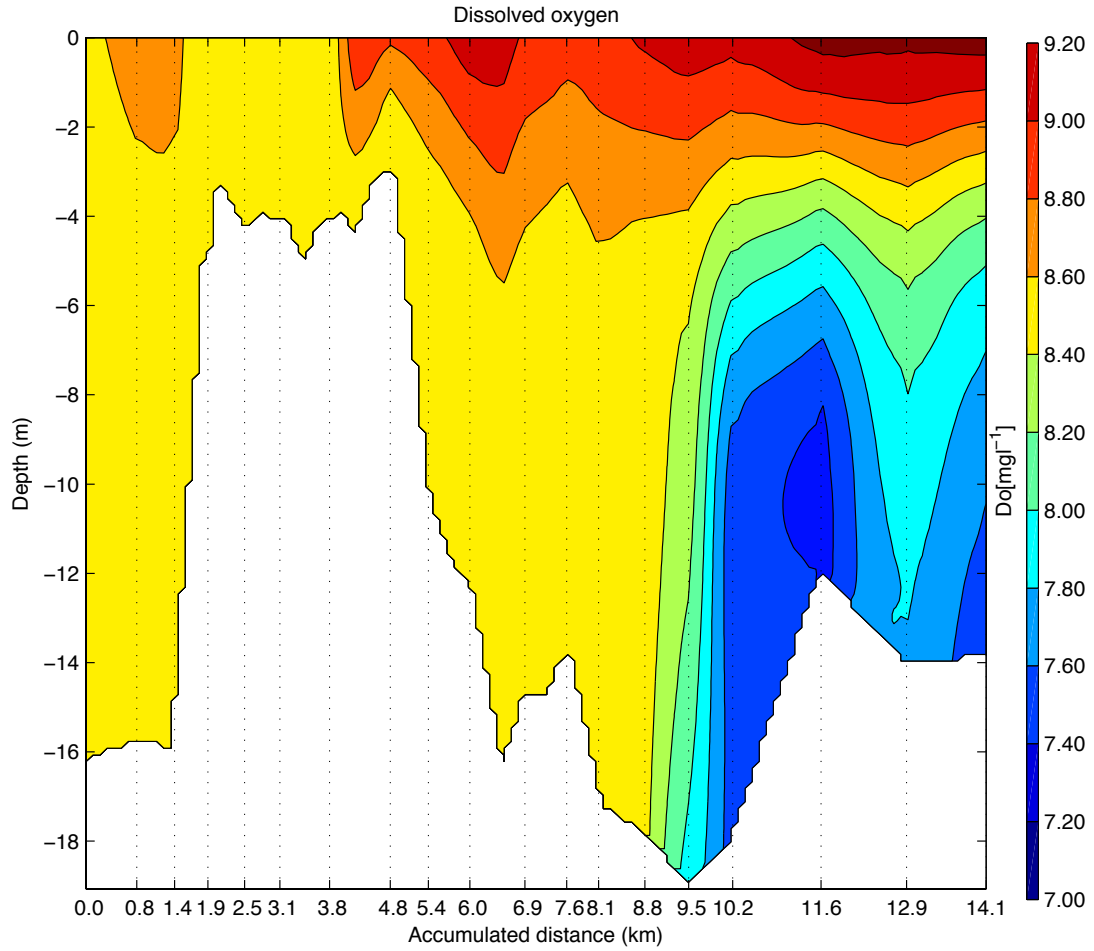

Figure 4.5 Contours of dissolved oxygen measured with the PFP on 27 August 2012 in the lower part of the Swan River Estuary.

4.2.3 Velocity field

4.2.3.1 Longitudinal velocity

Positive velocity was assumed to be oceanward. The velocity contours revealed that longitudinal velocity throughout the period of samplings was positive (Figure 4.6). In other words, water that was discharged out to the ocean was a combination of the ocean water that entered the estuary on high tide and fresh water from upstream creeks. Figure 4.6 shows that the major part of the study site showed longitudinal

velocity of about 0.10 ms^{-1}. However in some places the maximum velocity of about 0.5 $ms^{-1}$was observed in surface layers.

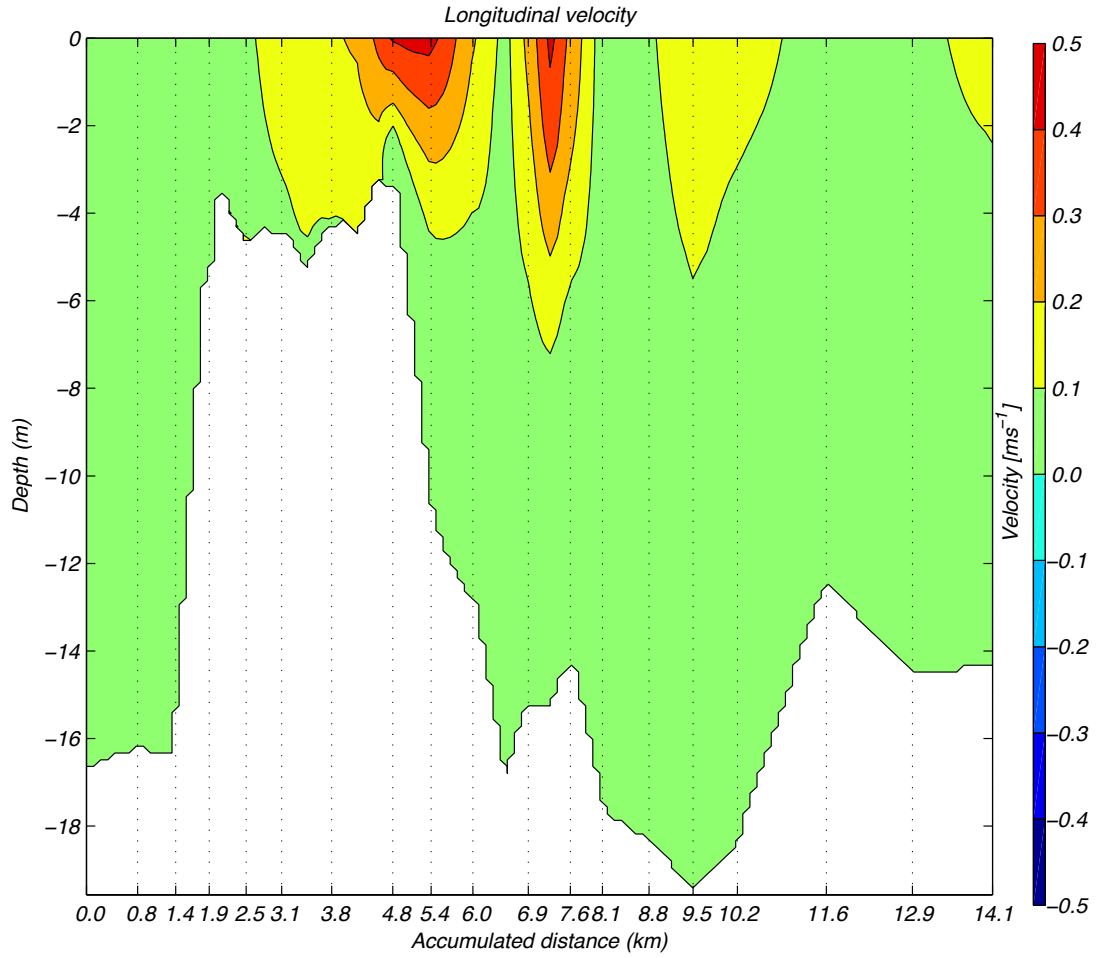

Figure 4.6 Longitudinal velocity measured with the PFP on 27 August 2012 in the lower part of the Swan River Estuary.

4.2.3.2 Shear

The curtain of shear is presented in Figure 4.7. Although the maximum shear was observed in surface layers, minimum shear was almost in the bottom layers. However, some profiles at which the total depth is considerably less than other places presented higher shear compared to other places at the bottom (accumulated distance between 1.4 and 1.8 Km). The maximum shear was 0.65 s^{-1} in the surface layer and minimum shear of about 0.1 $s^{-1}$was observed in the bottom layers. Except in the place with maximum shear, some other patches in the surface presented shear with considerable magnitude.

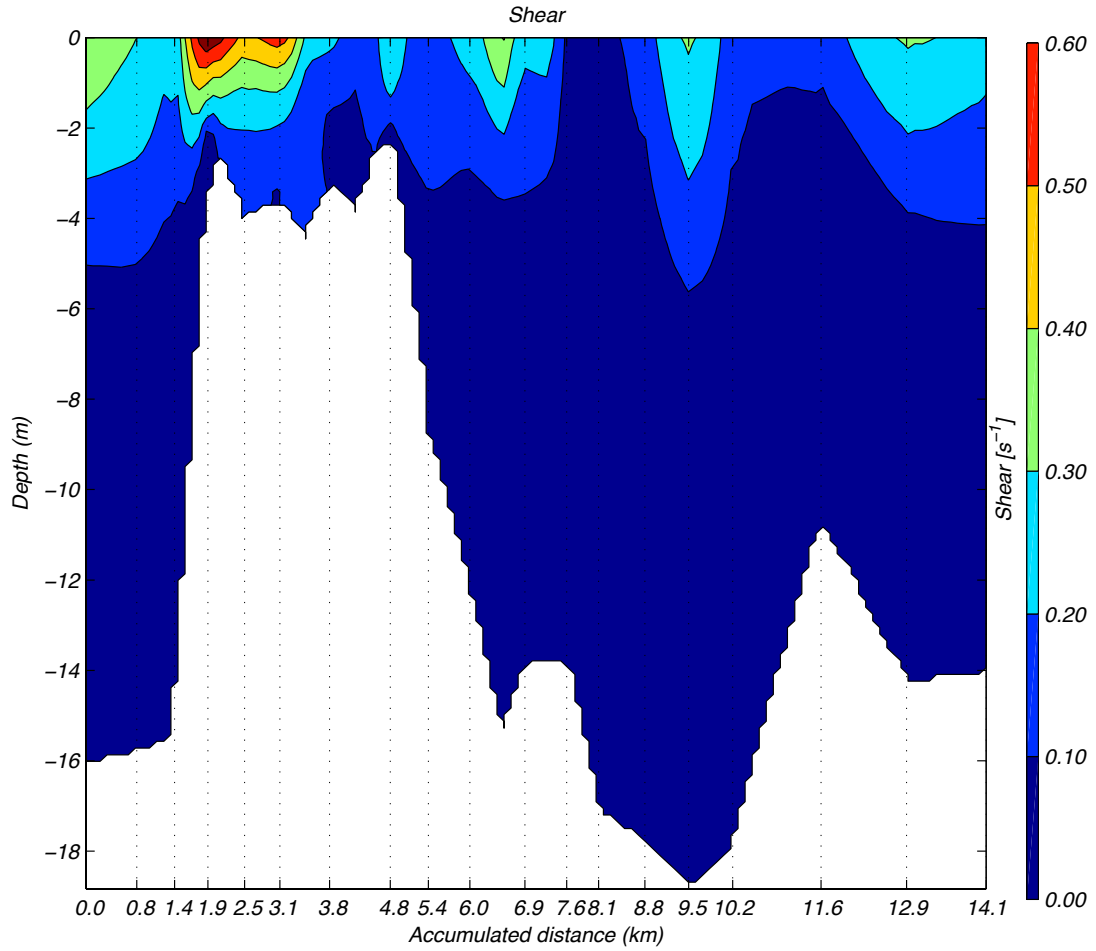

Figure 4.7 Shear estimated on 27 August 2012 in the lower part of the Swan River Estuary.

4.2.3.3 Buoyancy frequency

The buoyancy frequency curtain is presented in Figure 4.8. The maximum of the buoyancy frequency 10^{-2} s^{-2} happened in the surface layer in the upper part of the study site in the place with strong stratification (see Figure 4.4). Even in the lower part of the domain where there was weak stratification, buoyancy contours properly showed the variability of the stratification (the distance between 0.0 and 2.5 Km). Although the minimum of N^2 happened in both the surface and bottom layers, the occurrence of the minimum of buoyancy frequency at the bottom layers was larger than at the surface. The least value was about (10^{-5} s^{-2}).

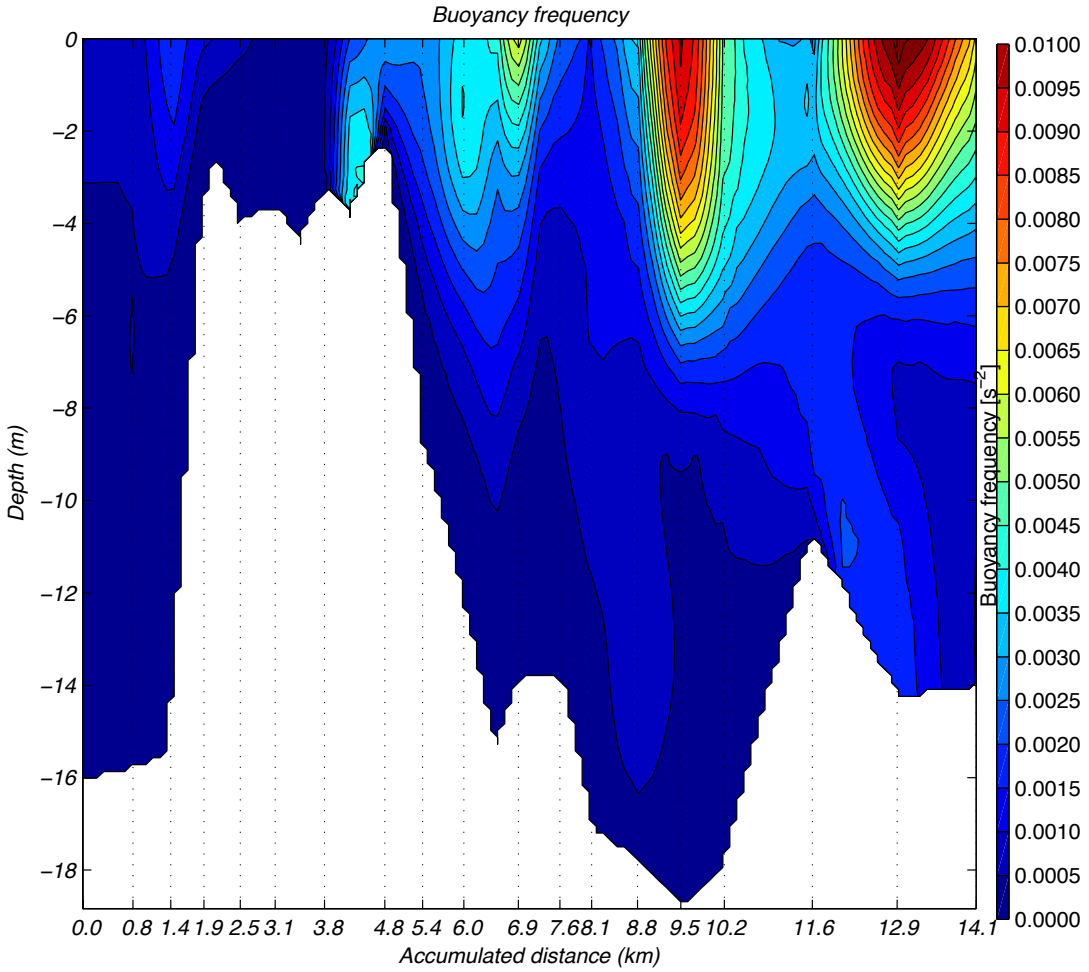

Figure 4.8 Buoyancy frequency estimated on 27 August 2012 in the lower part of the Swan River.

4.2.3.4 Gradient Richardson number

The gradient Richardson number showed extensive ranges of change. Although the maximum of about 3.5 was estimated in some places in the domain (upper boundary), some places with Ri_g<0.25 were observed. The minimum gradient Richardson number in the surface layer coincided with places with large shear (Figure 4.7).

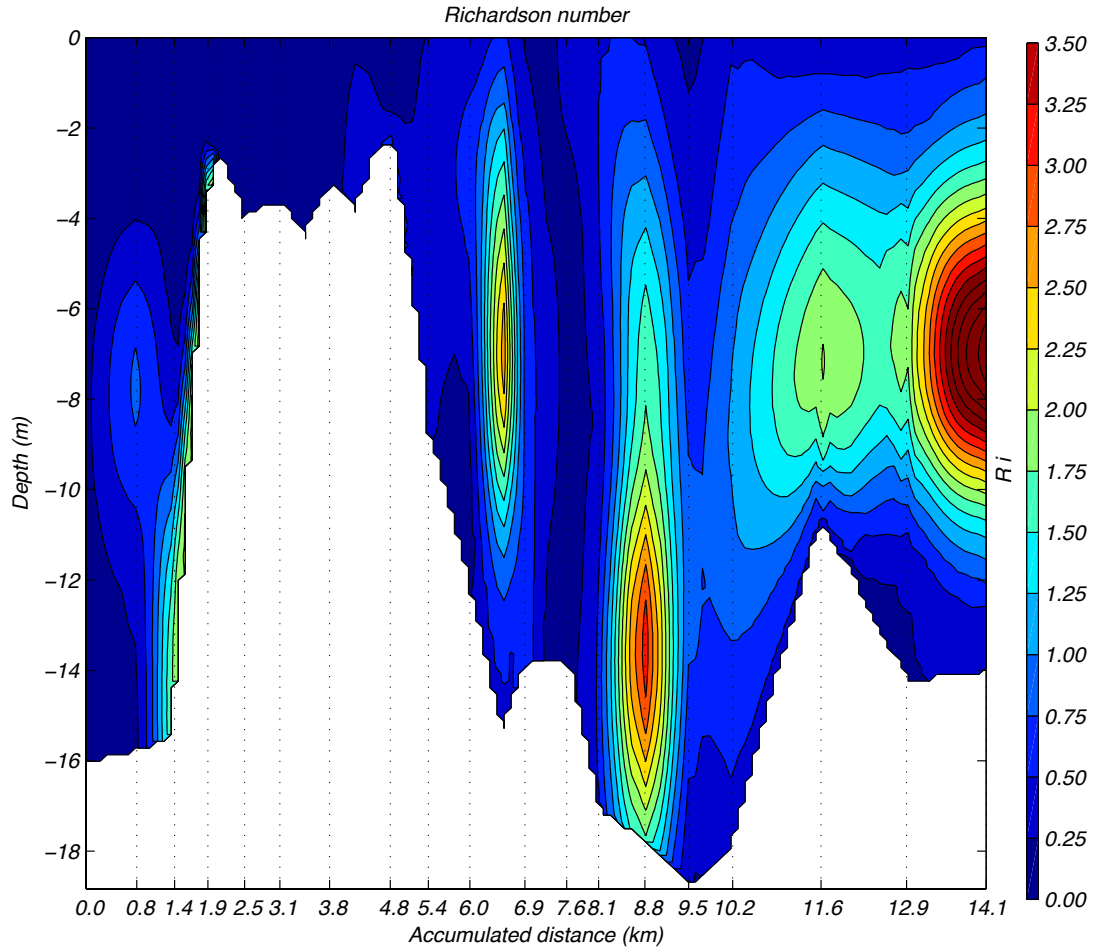

Figure 4.9 Gradient Richardson number calculated on 27 August 2012 in the lower part of the Swan River Estuary.

4.2.4 Turbulent properties

4.2.4.1 Shear dissipation

Contours of logarithmic values of shear dissipation are presented in Figure 4.10. Some patchy places with considerable dissipation were observed in the surface layer. The maximum value of shear dissipation occurred in the surface layer with a magnitude of about 10^{-5} m^2s^{-3}. In some locations of the study site, shear dissipation less than 10^{-8} m^2s^{-3} was observed. The range of shear dissipation varied between 10^{-8} and 10^{-5} m^2s^{-3}.

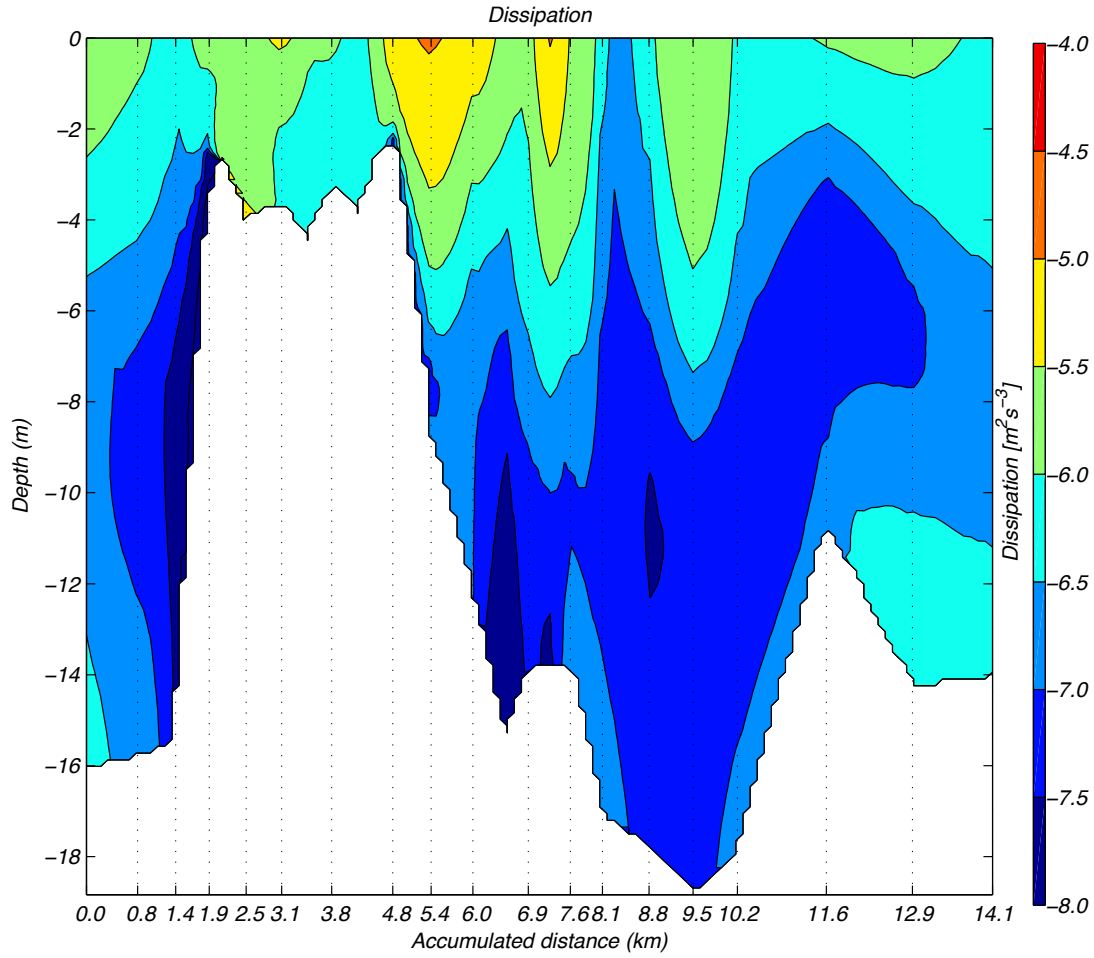

Figure 4.10 Curtain of logarithm of shear dissipation observed on 27 August 2012 in the domain of the field measurements.

4.2.4.2 Reynolds stress

Reynolds stress ($\rho v_1' v_3'$) varied between -0.5 and 0.5 $kgm^{-1}s^{-2}$ (Figure 4.11). It did not show significant events, either minimum values or maximum values. No particular structure was found in the curtain.

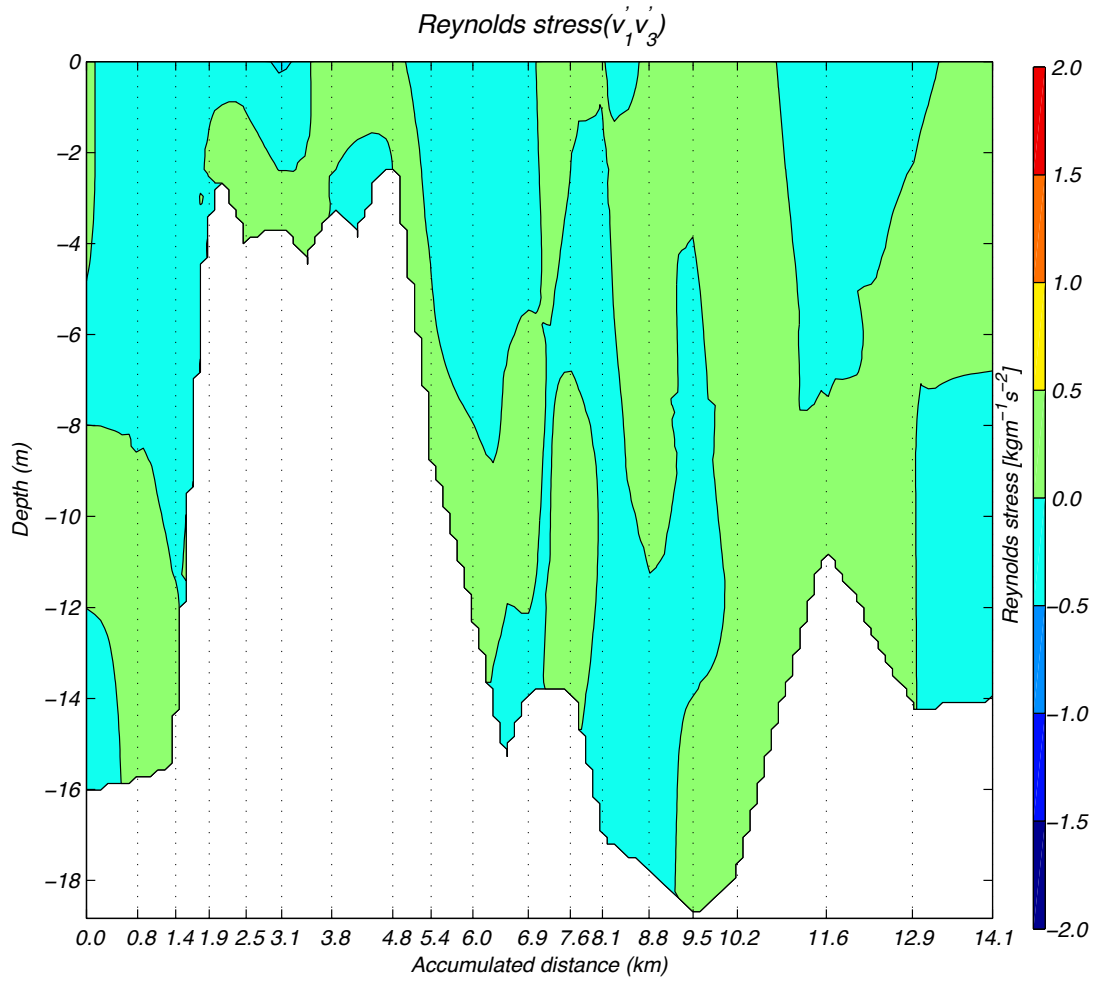

Figure 4.11 Reynolds stress ($\rho v_1' v_3'$) observed in the study area on 27 August 2012.

Unlike the previous component of Reynolds stress, another component of Reynolds stress ($\rho v_2' v_3'$) showed some small events (Figure 4.12). Two considerable events with a maximum of about 1.5 kgm^{-1}s^{-2} but with a small extent were observed in both the surface and bottom layers. Moreover, two local significant minima with a value of about -1 kgm^{-1}s^{-2} were recorded in the surface layer. However the major portion of the domain showed similar values to ($\rho v_1' v_3'$).

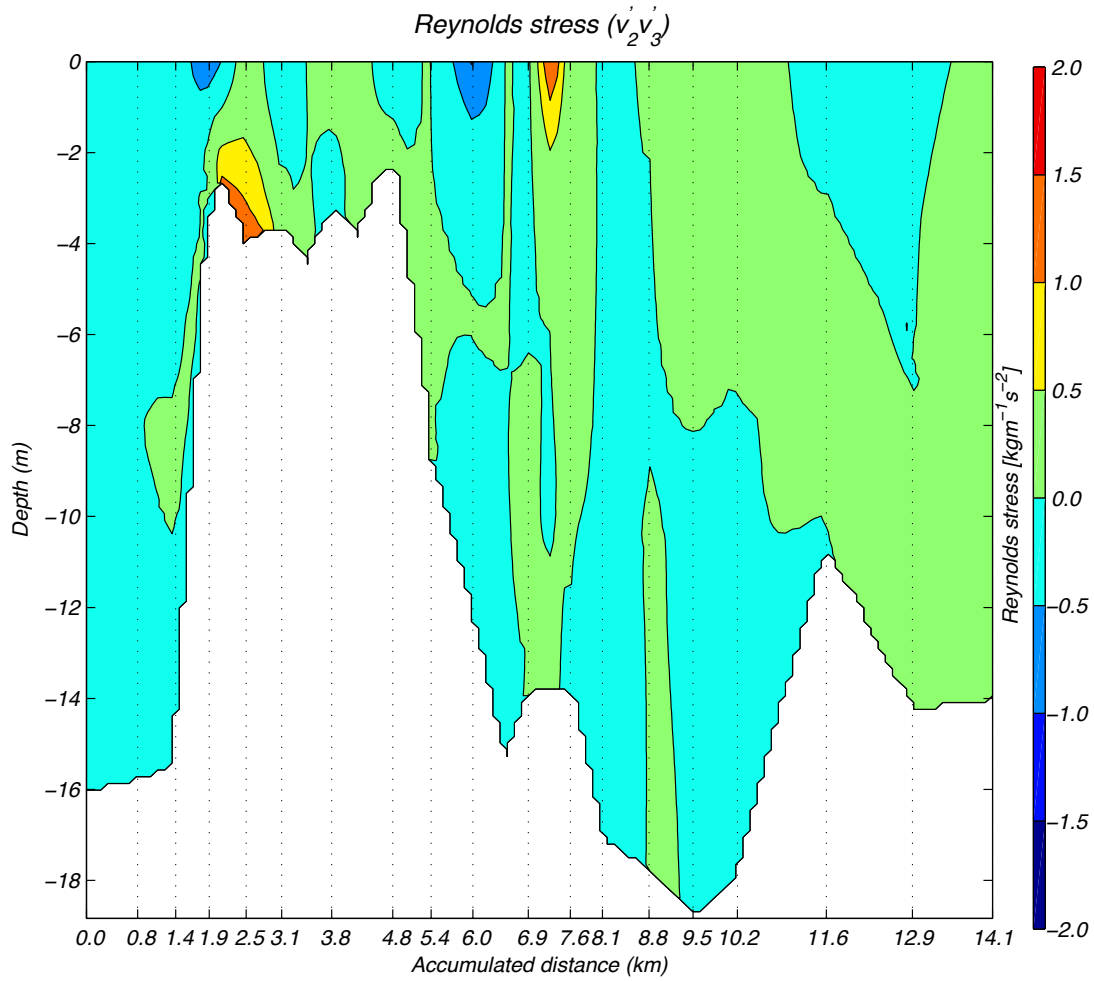

Figure 4.12 Reynolds stress ($\rho v_2' v_3'$) observed in the study area on 27 August 2012.

4.2.4.3 Buoyancy fluxes

The curtain of buoyancy flux is presented in Figure 4.13. Buoyancy fluxes varied between 10^{-8} and 10^{-6} m^2s^{-3}. The maximum value happened in the surface layer (two local patches). However, a local maximum with a limited extent was observed at the bottom of the river mouth. The maximum of the buoyancy fluxes revealed the same structure as shear dissipation (Figure 4.10). The maxima of dissipation and buoyancy fluxes coincided with each other.

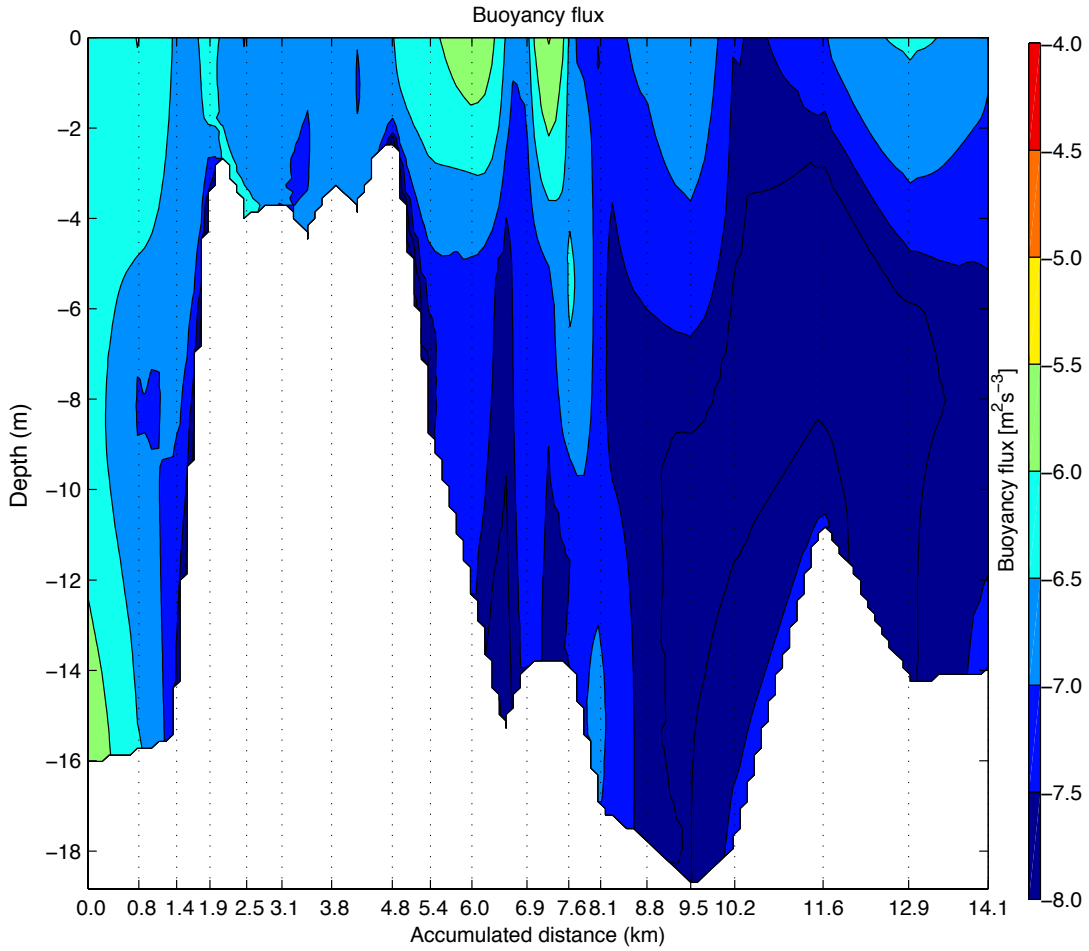

Figure 4.13 Buoyancy fluxes observed in the field measurements on 27 August 2012.

4.3 Field measurements for validation data (on 8 October 2012)

4.3.1 Background environmental condition

The field measurement on 8 October 2012 was carried out during the neap tides. Samplings were conducted during the ebb tides. While the maximum water level of about 0.20 m was recorded at 00:45 am, a minimum of about -0.25 m was observed at 01:45 pm (water surface level was relative to Australian Height Datum (AHD) and recorded at the Fremantle tide gauge). Throughout the period of study a decrease of about 0.12 m happened in the water surface (Figure 4.14a). Wind fields were recorded at the LDS station. Like the field measurements on 27 August, wind conditions were generally calm during the measurements (Figure 4.14b). However,

at the end of the field experiment wind speed increased. The maximum wind was observed at 07:00 pm with a magnitude of about 3.20 ms^{-1}. The minimum wind speed (0.5 ms^{-1}) occurred at 05:45 am. Like wind, air temperature was recorded at the LDS station. During the period of measurement the air temperature increased from 14.40 $^{\circ}C$ to 18.20 $^{\circ}C$ (Figure 4.14c). Water temperature increased from 18.15 $^{\circ}C$ at 07:00 am to 20.50 $^{\circ}C$ at 07:45 pm. The average of the relative humidity was about 70 per cent. Figure 4.14 uses the averaged data over 15-minute intervals.

4.3.2 Mean variables

As previously mentioned in Chapter 2, one of the objectives of the field trip on 8 October was to validate the velocity field obtained from the PFP by application of the inverse method. The inverse method is based on the temporal and spatial changes of some passive tracers (mean variables). Therefore, the contours of tracers in five consecutive transects such as salinity, temperature, dissolved oxygen, pH and turbidity are presented in Chapter 5. However, the velocity field and turbulent properties are presented in this chapter.

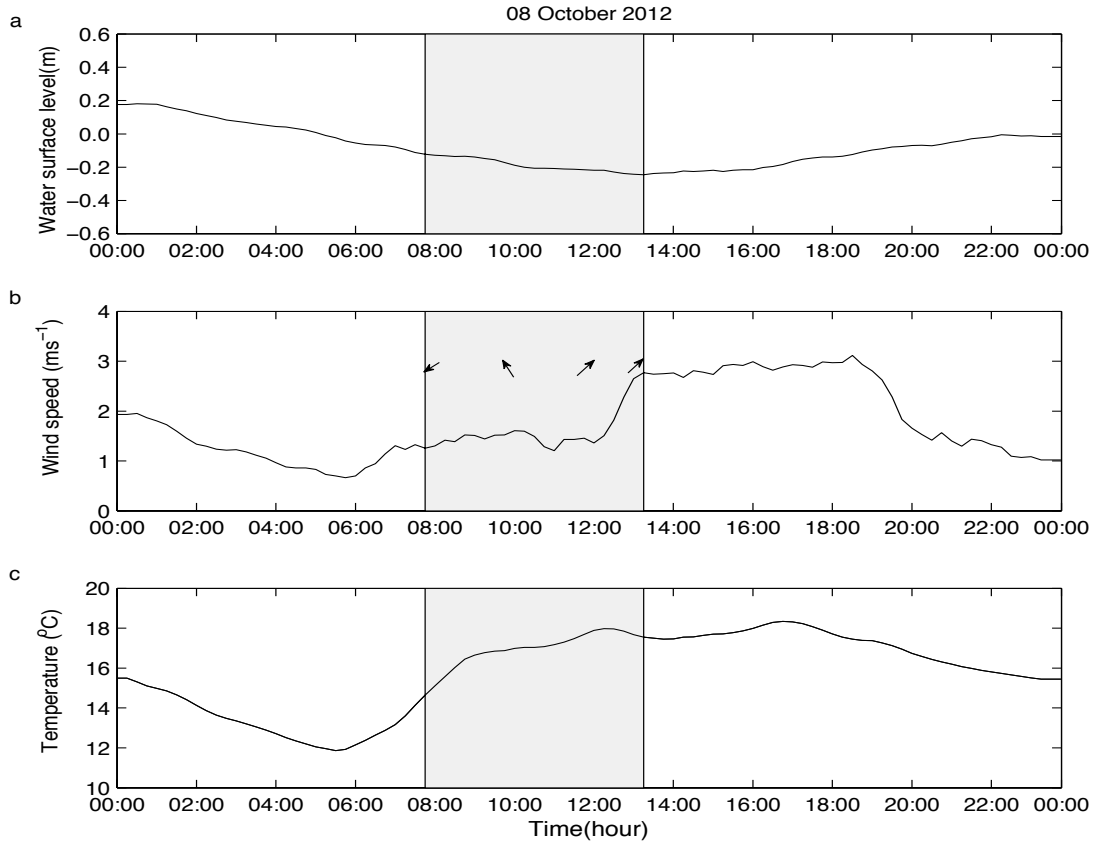

Figure 4.14 Water levels, wind speed (arrows show wind direction), and temperature recorded on 8 October 2012 in the lower part of the Swan River Estuary during the ebb tide of neap tides. Shaded area shows the time at which the field measurement was conducted.

4.3.3 Velocity field

Although the field measurement was conducted in five consecutive transects on 8 October 2012, the results from the second and fifth transects are presented for consistency with the inverse velocity field in Chapter 5. As previously mentioned in Chapter 2, all accumulated distances are relative to Fremantle as the reference point.

4.3.3.1 Longitudinal velocity

Longitudinal velocity is presented in Figure 4.15. During the second transect, the entire domain flow was oceanward. Longitudinal velocity was considerably larger in

the surface layer. The maximum velocity (0.55 ms^{-1}) occurred at the river mouth at Fremantle. Except for two small locations in the domain, velocity was larger than 0.10 ms^{-1} (Figure 4.15a).

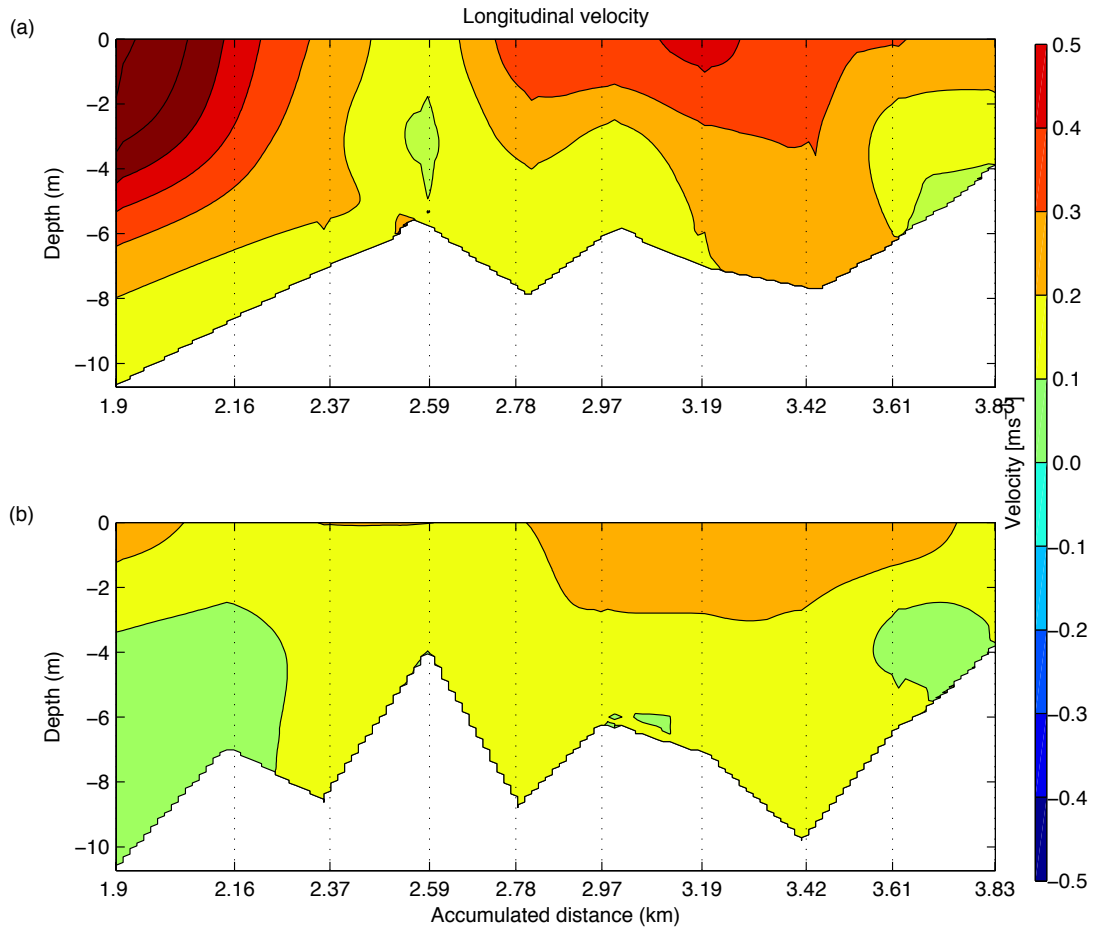

Figure 4.15 Longitudinal velocity measured with the PFP on 8 October 2012 in the study area. **(a)** Observed velocity at the second transect **(b)** Velocity measured at the fifth transect.

During the last transect of measurements, the maximum velocity—like transect two—was larger in the surface layer. However, compared to the second transect the velocity decreased. The magnitude of the maximum velocity was about 0.35 ms^{-1} and that was observed in the upper part of the study area. The major part of the domain had a velocity with a magnitude of 0.20 ms^{-1} (Figure 4.15b). Similar to the second transect, flow in the entire study area was positive (oceanward).

4.3.3.2 Shear

Figure 4.16 shows observed shear during the second and fifth transects. In both transects maximum shear with a magnitude of about (0.6 s^{-1}) was observed in the top layer. However, the locations of the occurrences were different. In the second transect the maximum happened at the river mouth (Figure 4.16a); while in the last transect the peak occurred in the upper boundary (Figure 4.16b). At the location of maximum shear in both transects, the large values of shear penetrated to a depth of about 4 m. Moreover, except for the maxima, some patches with large values of shear were observed in the surface layer in both transects. The considerable difference between the two transects related to a significant event with a value of about 0.25 s^{-1} that occurred at the bottom of the accumulated distance of about 3.40 Km.

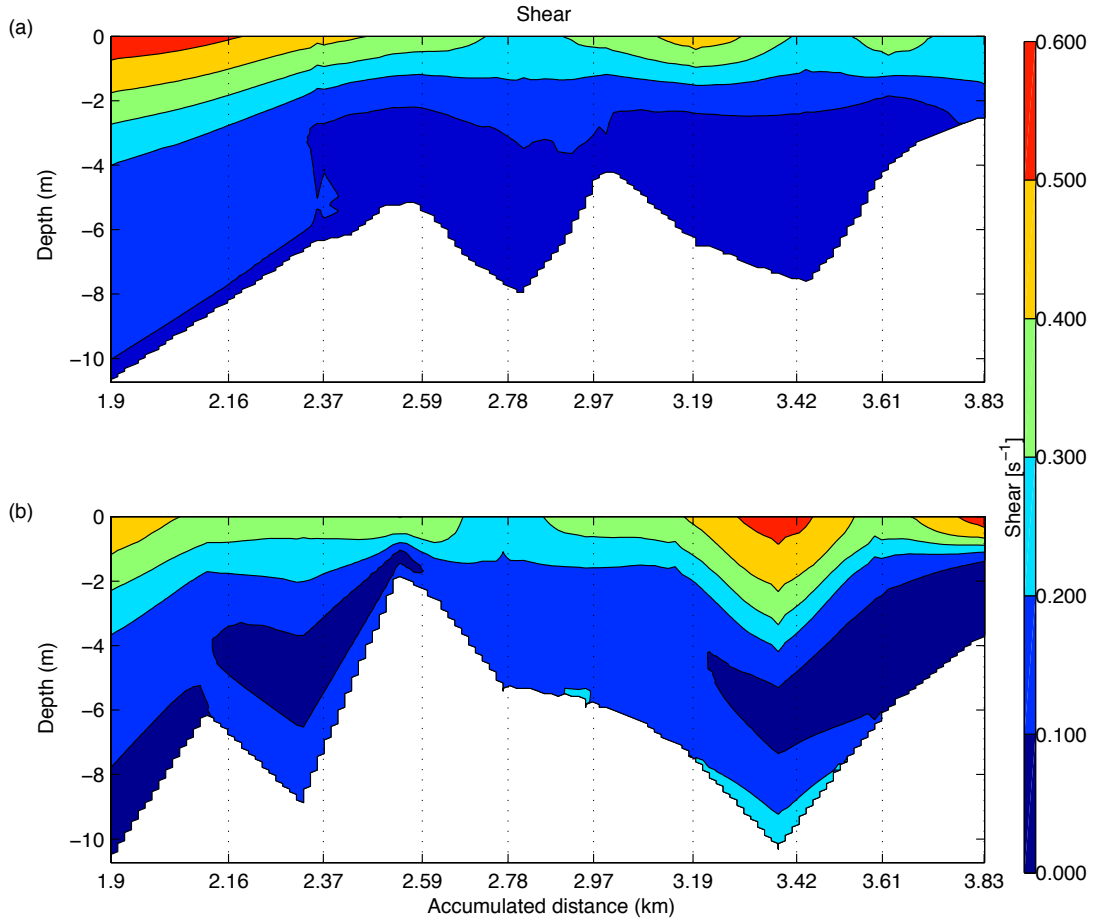

Figure 4.16 Shear based on the data collected with the PFP on 8 October 2012. **(a)** Observed shear during the second transect. **(b)** Observed shear in the last round of sampling.

4.3.3.3 Buoyancy frequency

Figure 4.17 presents buoyancy frequency. In the second duration of samplings a maximum value of about 4×10^{-3} s^{-2} was observed at the river mouth (Figure 4.17a) while the peak was about 10^{-2} s^{-2} for the last transect (Figure 4.17b). Both transects presented a minimum value of about 10^{-5} s^{-2}. While in the second transect the minimum values happened in both the surface and the bottom, in last transect the minimum only occurred at the benthic boundary. The contours of last transect (Figure 4.17b) implied more stratification compared to the second transect (Figure 4.17a).

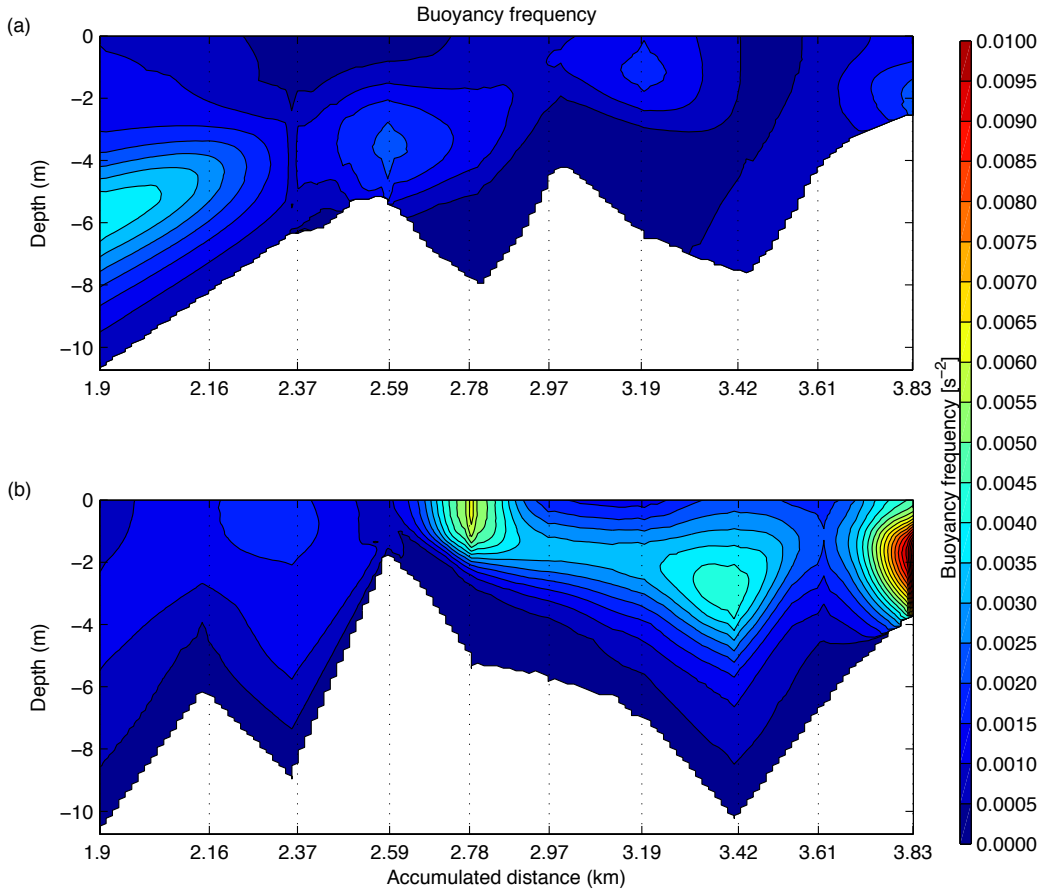

Figure 4.17 Buoyancy frequency estimated with data collected with the PFP on 8 October 2012 **(a)** Buoyancy frequency in the second transect **(b)** Buoyancy frequency in the fifth transect.

4.3.3.4 Gradient Richardson Number

The major part of the domain in both transects presented gradient Richardson numbers less than 0.25 (Figure 4.18). However, some local events with $Ri_g > 0.25$ were recorded too. These events were observed in the bottom layer. The value of the maximum gradient Richardson number increased from 2.25 in the second transect to 3 in the fifth transect. The contours of the fifth transect (Figure 4.18b) showed more values larger than the second transect (Figure 4.18a). As for buoyancy frequency, it implies more stratification in the water columns.

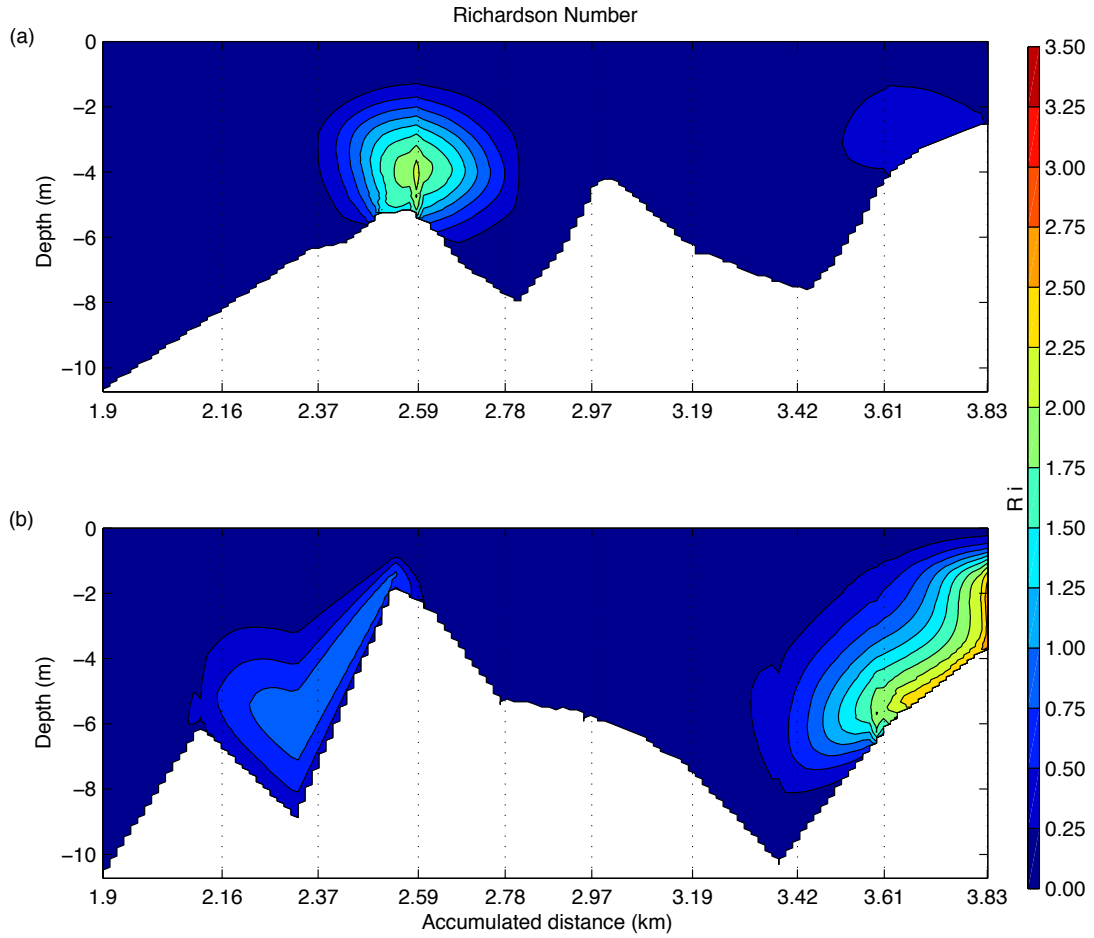

Figure 4.18 Gradient Richardson number observed on 8 October 2012 **(a)** Gradient Richardson number during the second transect **(b)** Gradient Richardson number during the fifth transect.

4.3.4 Turbulent properties

4.3.4.1 Shear dissipation

Figure 4.19 shows shear dissipation for both the second and fifth transects. In the second transect, shear dissipation varied between 10^{-7} and 10^{-5} m^2s^{-3}. The peak event occurred at the surface and the least value was observed at the bottom (Figure 4.19a). The rate of dissipation of turbulent kinetic energy changed between 10^{-8} and 10^{-5} m^2s^{-3} (Figure 4.19b). The maximum was limited to two small patches at the surface. The number of occurrences of maximum events in the second transect was larger than in the last transect.

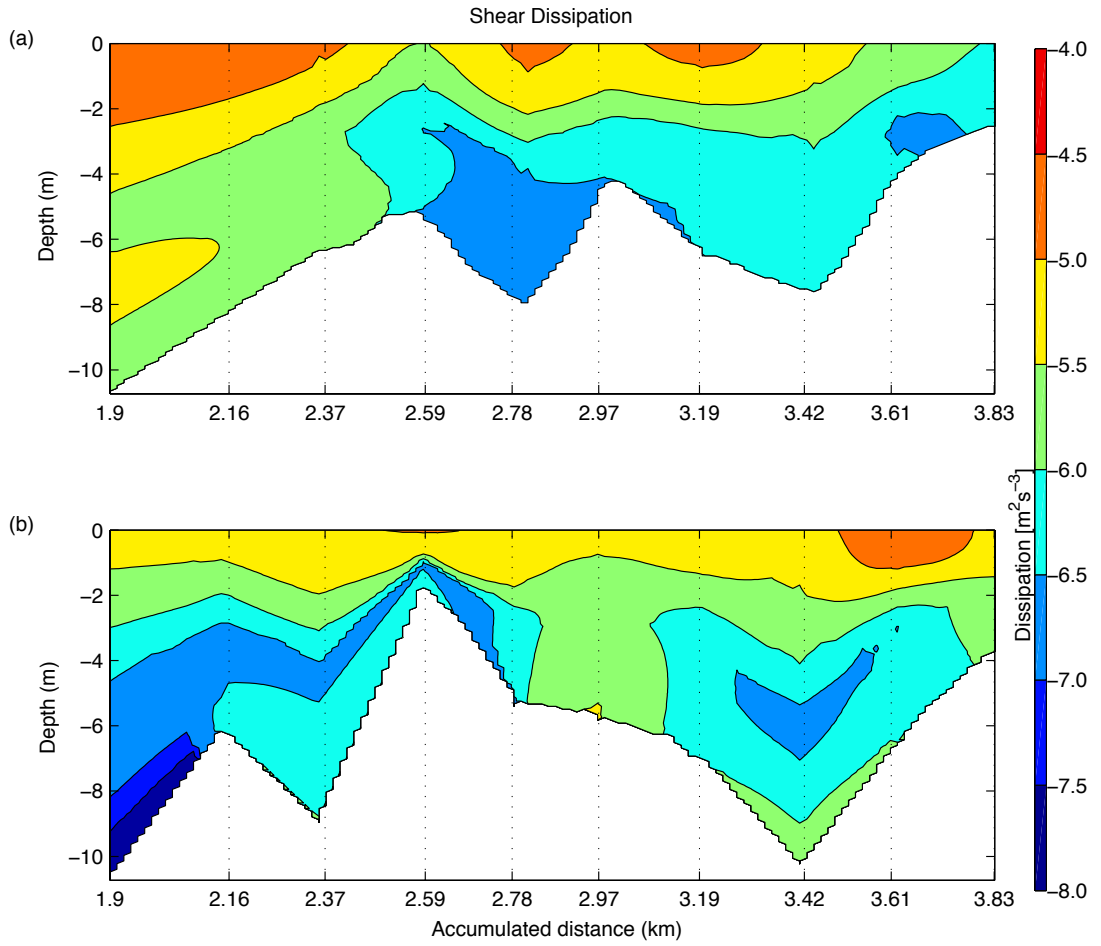

Figure 4.19 Shear dissipation estimated by data collected with the PFP on 8 October 2012 **(a)** Shear dissipation during the second transect **(b)** Shear dissipation in the fifth transect.

4.3.4.2 Reynolds stress

Reynolds stress ($\rho v_1' v_3'$) did not show any significant event except a minimum in the surface layer during the second transect with a magnitude of about 1 $kgm^{-1}s^{-2}$ (Figure 4.20a). During the last transect both maximum (2 $kgm^{-1}s^{-2}$) and minimum (-2 $kgm^{-1}s^{-2}$) was observed in the study area (Figure 4.20b). The maximum value was observed at the deepest point of the domain. A patch with a value of about 1 $kgm^{-1}s^{-2}$ was observed in the surface layer. Similarly to the maximum, the least values occurred in the surface and bottom layers. Minimum values were about -2 $kgm^{-1}s^{-2}$.

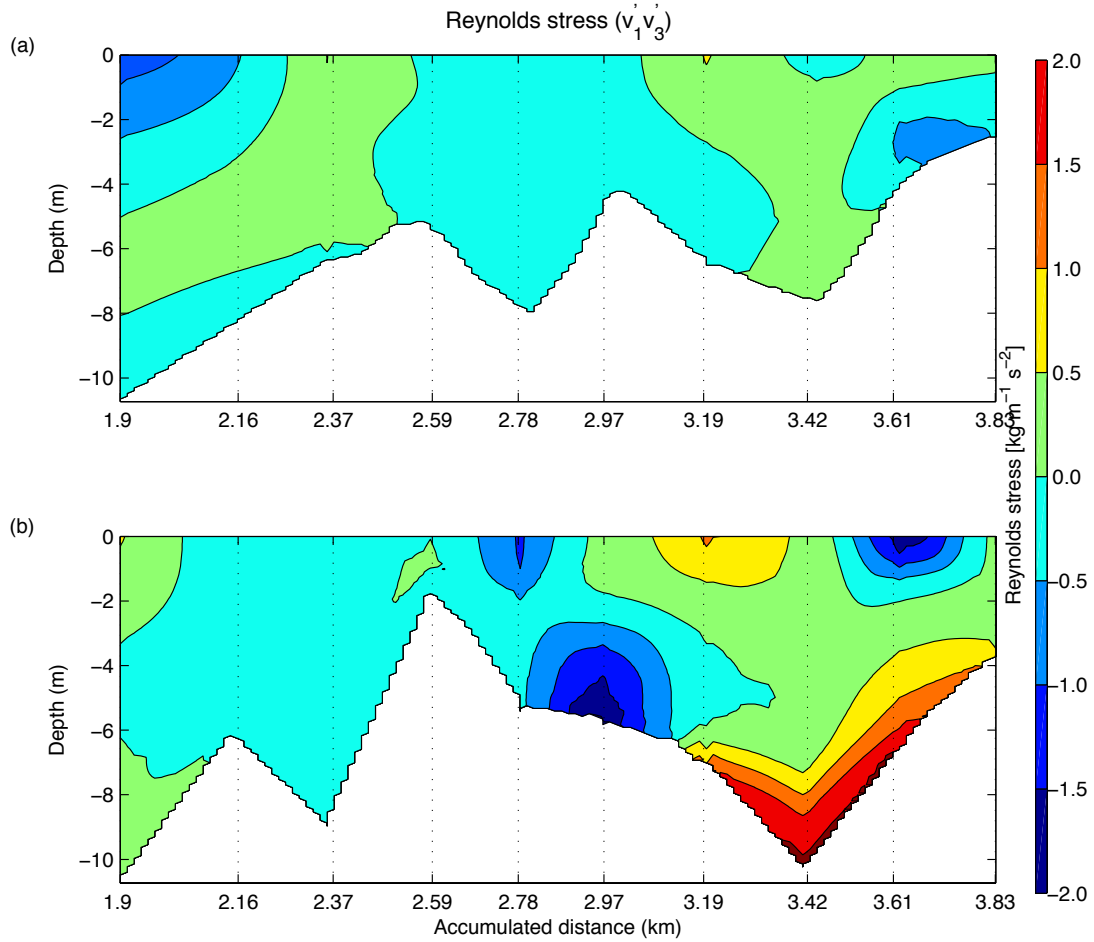

Figure 4.20 Reynolds stress $(\rho v_1' v_3')$ observed on 8 October 2012 (a) Reynolds stress observed throughout the second transect **(b)** Reynolds stress recorded during the fifth transect.

During the second transect the maximum of $\rho v_2' v_3'$ occurred in the surface layer at the upper boundary of the domain (Figure 4.21a). The maximum had a magnitude of about 2 $kgm^{-1}s^{-2}$. The minimum value was limited to a surface patch at the river mouth (-1 $kgm^{-1}s^{-2}$). The location of the minimum in the second transect was replaced with a maximum of about 2 $kgm^{-1}s^{-2}$ throughout the last transect. Moreover, a patch with a maximum of about 1.5 $kgm^{-1}s^{-2}$ was observed at the bottom of the upper boundary. Two places with minimum values of about -2 $kgm^{-1}s^{-2}$ were observed in the surface and bottom layers. However the extent of the minimum at the bottom was larger than the extent of the minimum at the surface layer.

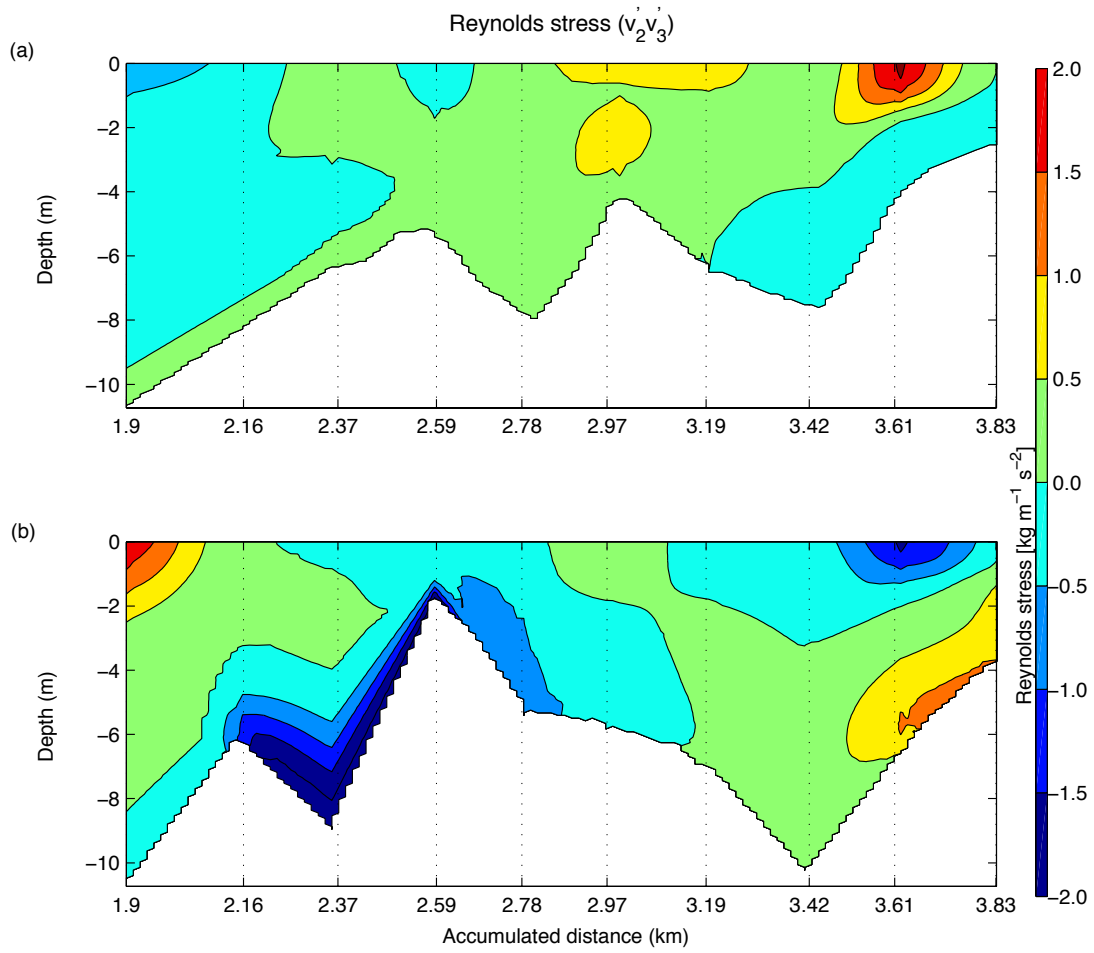

Figure 4.21 Reynolds stress $(\rho v_2' v_3')$ observed on 8 October 2012 **(a)** Reynolds stress during the second round of profiling **(b)** Reynolds stress during the final transect.

4.3.4.3 Buoyancy fluxes

Buoyancy fluxes for the second and fifth transects are presented in Figure 4.22. Buoyancy fluxes varied between 10^{-7} and 10^{-6} m^2s^{-3} throughout the second transect (Figure 4.22a). During the last set of sampling, buoyancy fluxes varied between 10^{-8} and 10^{-6} m^2s^{-3}. The minimum value was observed at the bottom of the river mouth. A considerable amount of buoyancy fluxes were observed at the deepest point of the river (Figure 4.22b).

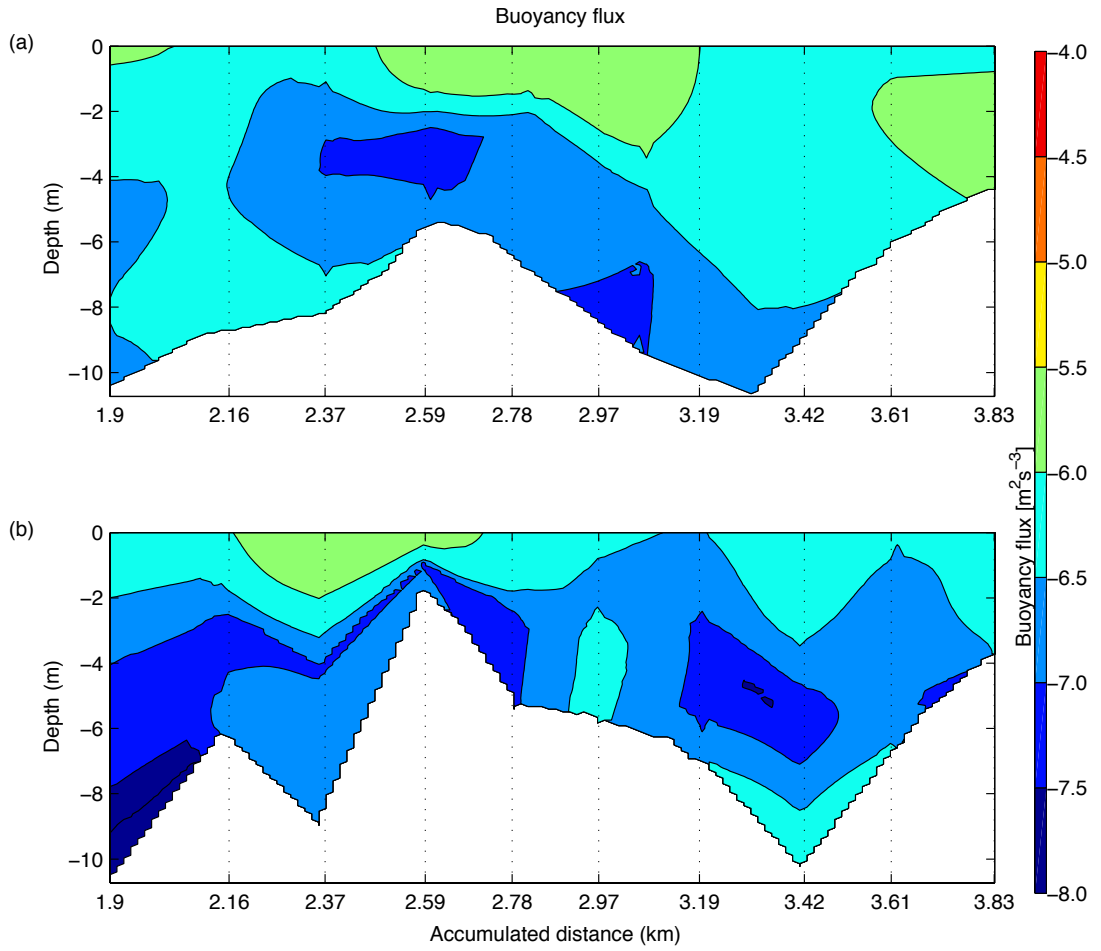

Figure 4.22 Buoyancy fluxes observed on 8 October 2012 **(a)** Buoyancy fluxes in the second transect **(b)** Buoyancy fluxes during the fifth transect.

4.4 Field measurements for supplementary data (on 2 November 2012)

4.4.1 Background environmental conditions

Water surface levels relative to Australian Height Datum (AHD) were recorded at the Fremantle tide gauge. The difference between high and low tide on 2 November 2012 was larger than 0.6 m. However, the difference in water surface levels during the period of field measurement was less than 0.02 m (Figure 4.23a). In fact, this field measurement was conducted during slack tide. Wind speed recorded at the LDS station was considerably larger than on the previous field trip. The average wind speed during the field measurements was 2.32 ms^{-1} (Figure 4.23b). The maximum air temperature (19.42 $^{\circ}C$) was recorded at 03:15 pm, and a minimum of about 15.71$^{\circ}C$

was measured at 03:45 am at the LDS station. The difference between the maximum and minimum air temperature throughout the field study was $0.09^{\circ}C$ (Figure 4.23c). The difference in the maximum and minimum of the water temperature on 2 November was 1.44 $^{\circ}C$, while the difference during the sampling was 0.3 $^{\circ}C$. Throughout the field experiment the water temperature increased from 19.75 $^{\circ}C$ to 20.06 $^{\circ}C$. The average relative humidity during the field study was 68 precent which was smaller than during previous field experiments. This field trip lasted two hours; therefore, no significant changes were observed in meteorological data. Figure 4.23 was built based on averaged data in 15-minute intervals.

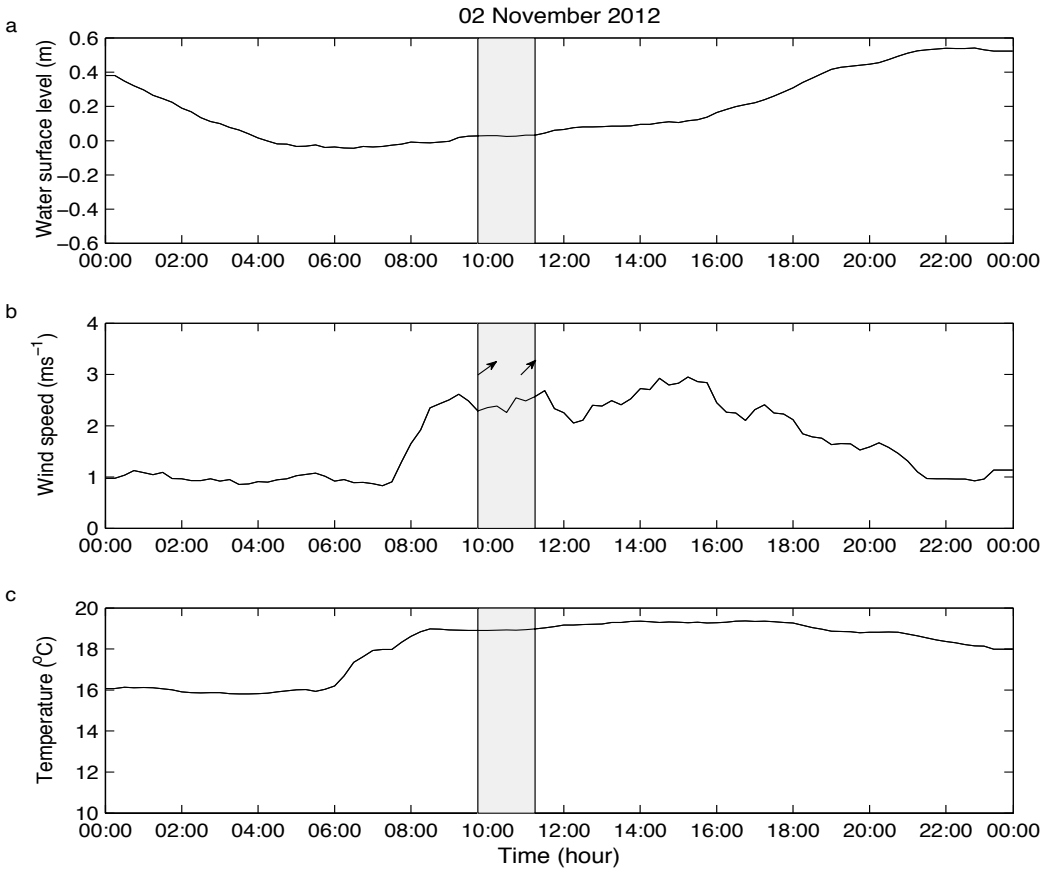

Figure 4.23 Water levels, wind speed (arrows show wind direction), and temperature recorded on 2 November 2012 in the lower part of the Swan River Estuary. (a) Water surface levels relative to AHD, (b) Wind speed recorded at LDS. (c) Air temperature observed at LDS.

4.4.2 Mean variables

4.4.2.1 Salinity

The salinity curtain shows a strong stratification, on 2 November 2012 (Figure 4.24). The stratified water filled the entire domain. Brackish waters originating from the upper part of the domain were on top of salty water and had the minimum salinity. This brackish water made for a stronger stratification in the upper part. The maximum salinity was observed in the bottom of the river mouth. Although water columns showed strong stratification, the vertical distance between isohaline contours in the upper part of the domain was smaller than at the lower boundary of the domain at Fremantle. Therefore the intensity of stratification in the upper part was larger than at the lower part of the domain.

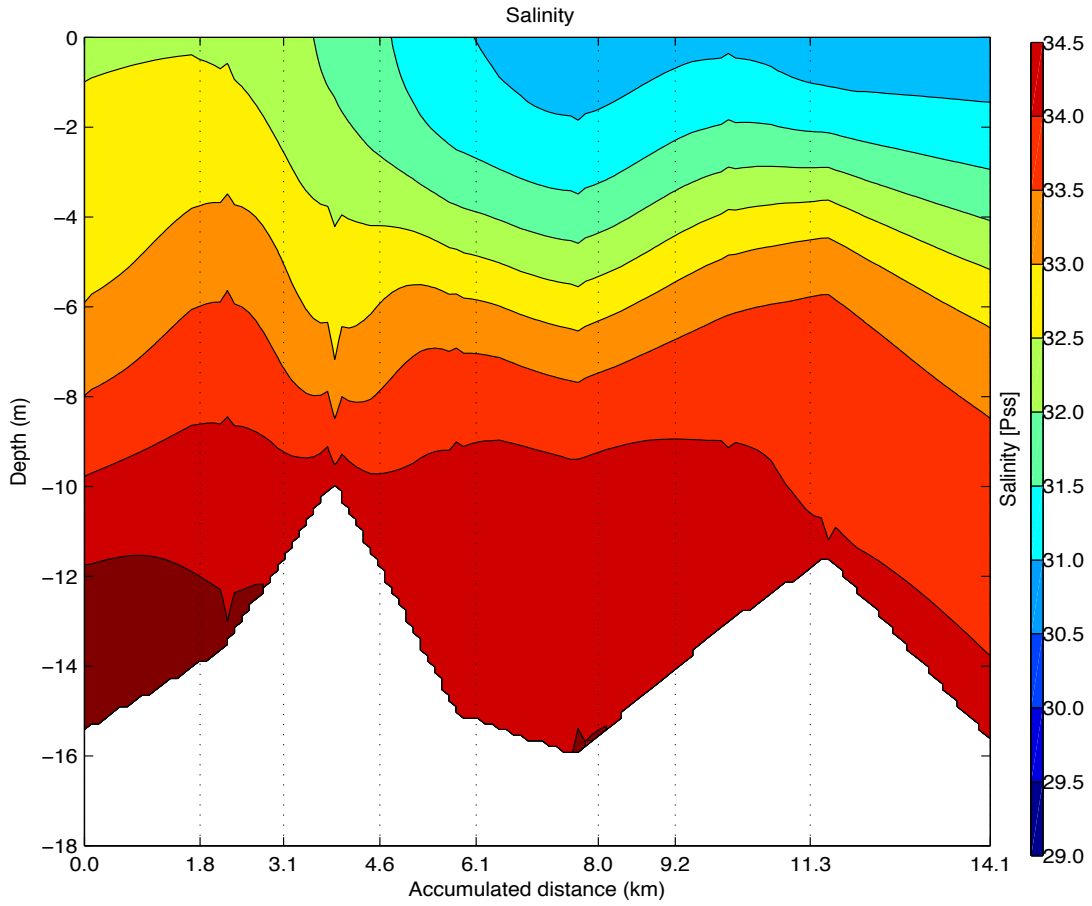

Figure 4.24 Salinity curtain collected with the PFP on 2 November 2012. The stratification filled the entire domain.

4.4.2.2 Temperature

Figure 4.25 presents temperature contours through the field of study conducted on 2 November 2012. There was an evident thermal stratification in the water column. The maximum water temperature was observed in the surface layer at the middle part of the domain. In the middle part of the domain the intensity of the stratification was stronger than in other parts. Water temperature at the surface layer in the lower part of the domain was less than in other parts. It implies the role of higher water temperature from upstream in building the thermal structure of the domain.

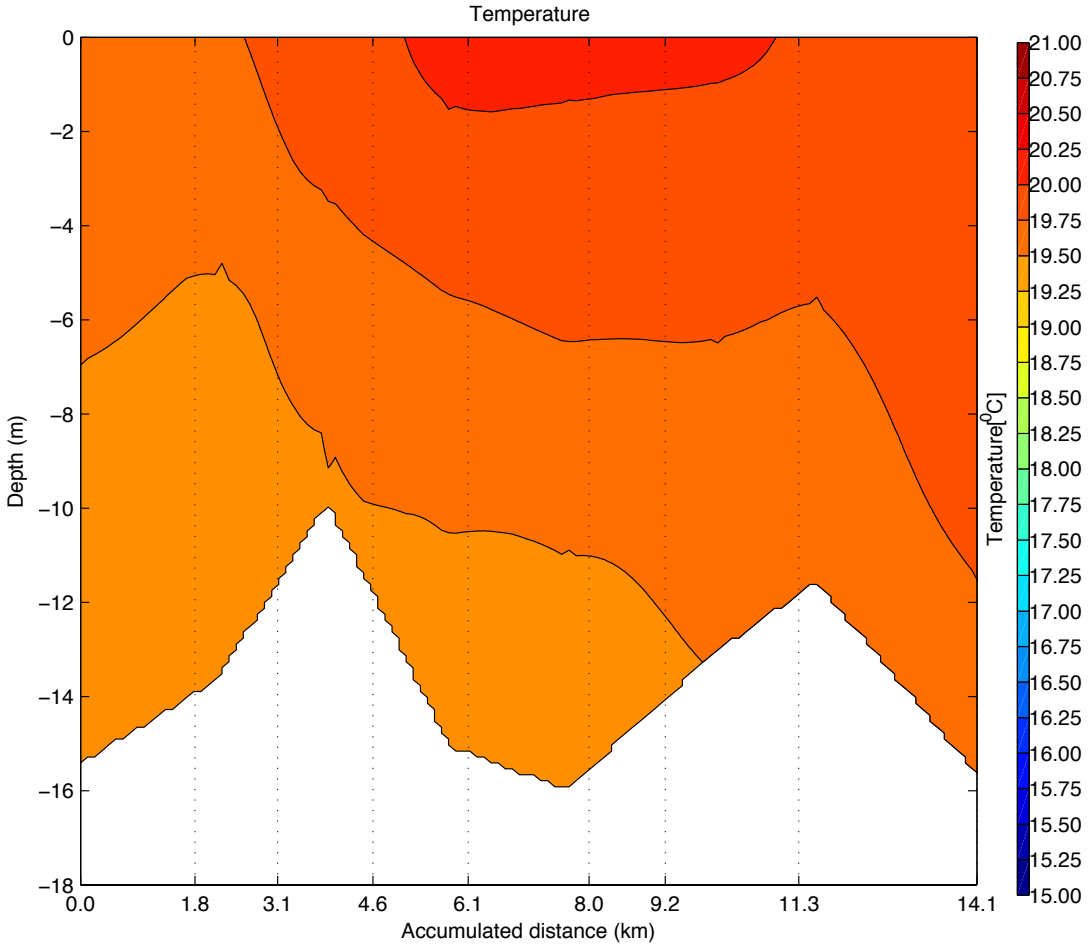

Figure 4.25 Temperature contour measured with the PFP on 2 November 2012.

4.4.2.3 Density

Density contours showed a similar structure to salinity contours (Figure 4.26). The contours showed stratification with a higher intensity in the upper part of the domain than in the lower part in Fremantle harbour. The minimum density was observed in the surface layer of the upper part of the domain, originating from the upper Swan. The maximum density corresponded to the ocean salt wedge observed at the bottom of the river mouth. Similarly to salinity, the intensity of stratification in the upper part was larger than at the river mouth. A large density spot was trapped at the deepest point of the river. The difference between the maximum and minimum density was about 3.5 kgm^{-3}.

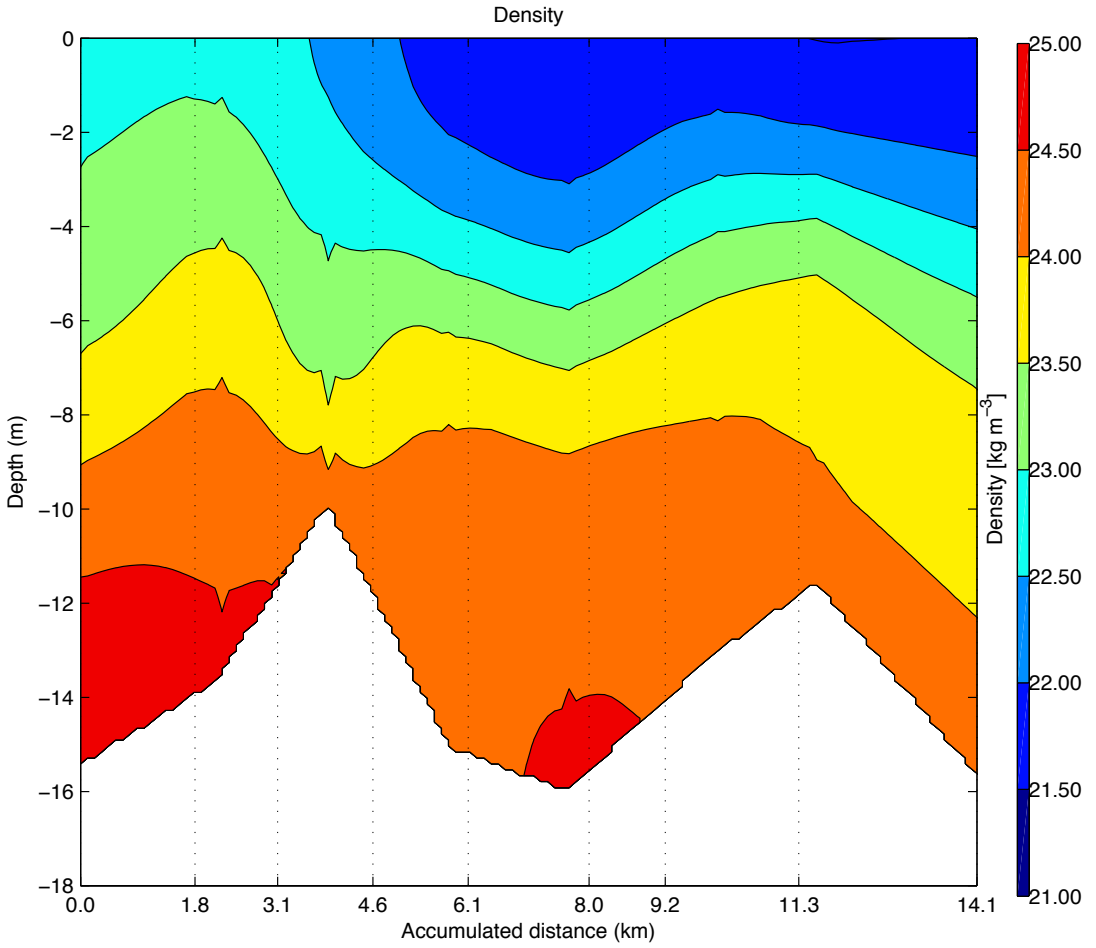

Figure 4.26 Density contours recorded with the PFP in the domain on 2 November 2012.

4.4.2.4 Dissolved oxygen

Dissolved oxygen varied between 7 and 8.40 mgl^{-1} on 2 November 2012 (Figure 4.26). While the lower part of domain was filled with fully-mixed water columns of dissolved oxygen with a magnitude larger than 8.20 mgl^{-1}, in the upper part, particularly in the bottom, a lower concentration of dissolved oxygen was observed. A local maximum of dissolved oxygen (8.40 mgl^{-1}) was observed in the surface layer in the middle part of the domain. The contours show that no dissolved oxygen issues, such an anoxia zone, were found in the domain.

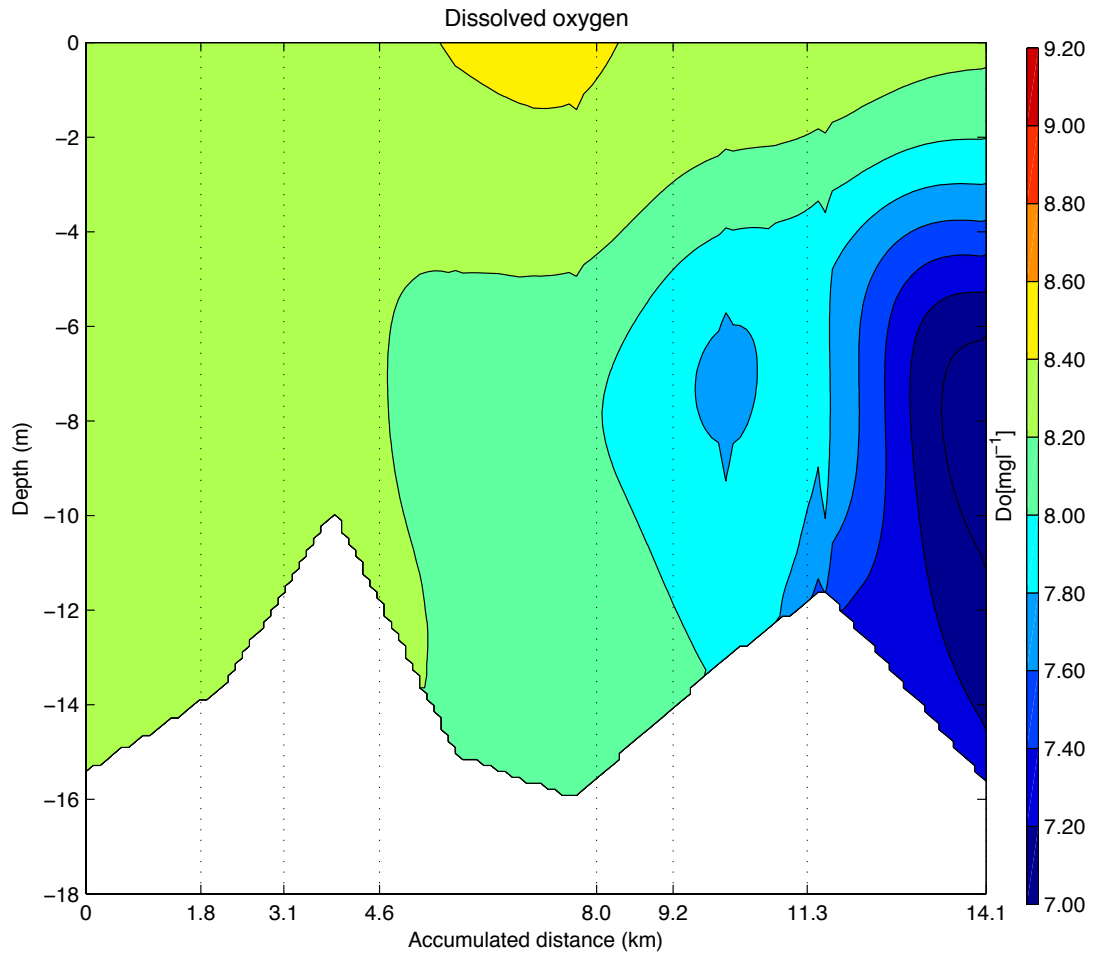

Figure 4.27 Dissolved oxygen curtain measured with the PFP on 2 November 2012.

4.4.3 Velocity field

4.4.3.1 Longitudinal velocity

Longitudinal velocity is shown in Figure 4.28. Longitudinal velocity varied between 0.1 and 0.2 ms^{-1} except in a very limited patch at the surface in the upper part of the domain with a velocity of about 0.30 ms^{-1}. Velocity contours showed that between a distance from the river mouth of about 3.1 and 8.0 Km all depths of water columns from the surface to the bottom had a velocity of about 0.20 ms^{-1}. A surface layer with a velocity of about 0.20 ms^{-1} at the river mouth was confined to a depth of 2 m compared to the upper part of the domain where this velocity filled a layer with 4 m depth.

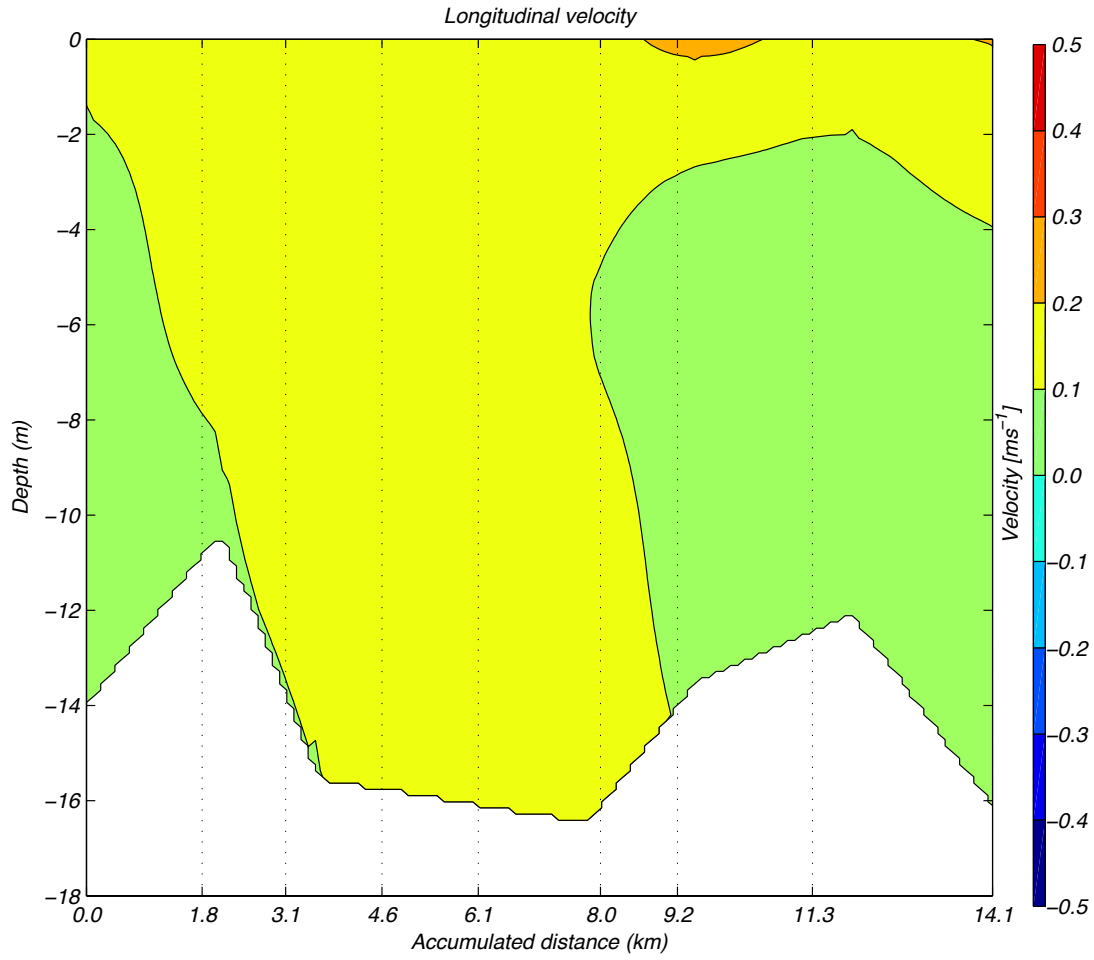

Figure 4.28 Longitudinal velocity measured with the PFP on 2 November 2012.

4.4.3.2 Shear

The shear curtain is presented in Figure 4.29. The maximum shear of about 0.65 s^{-1} was observed in the surface layer between the river mouth and up to 4.6 Km relative to the reference point. At the upper part of the domain, considerable shear with a magnitude of about 0.6 s^{-1} was observed at the surface layer. A minimum shear with a magnitude less than 0.1 s^{-1} was observed throughout the length of the river. Although the domain was in a sheltered area, wind affected surface layers.

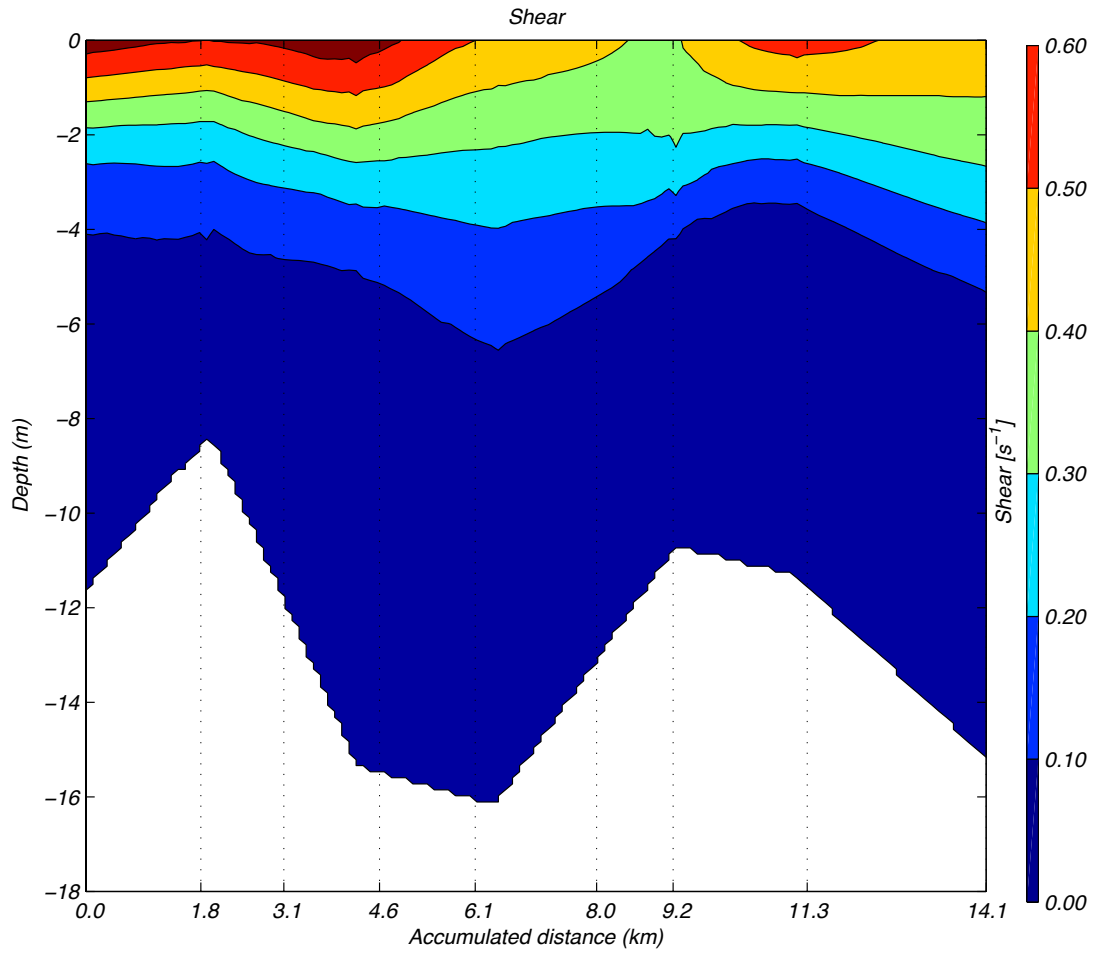

Figure 4.29 Shear observed in the domain on 2 November 2012.

4.4.3.3 Buoyancy frequency

Figure 4.30 shows buoyancy frequency on 2 November 2012. The maximum of about 4×10^{-3} s^{-2} was observed in the middle of the domain. The minimum buoyancy frequency was observed in both the surface and bottom layers. However the possibility of the occurrence of a minimum at the bottom was larger than at the surface. The magnitude of the minimum was 10^{-5} s^{-2} which was consistent with previous field measurements in the Swan River Estuary.

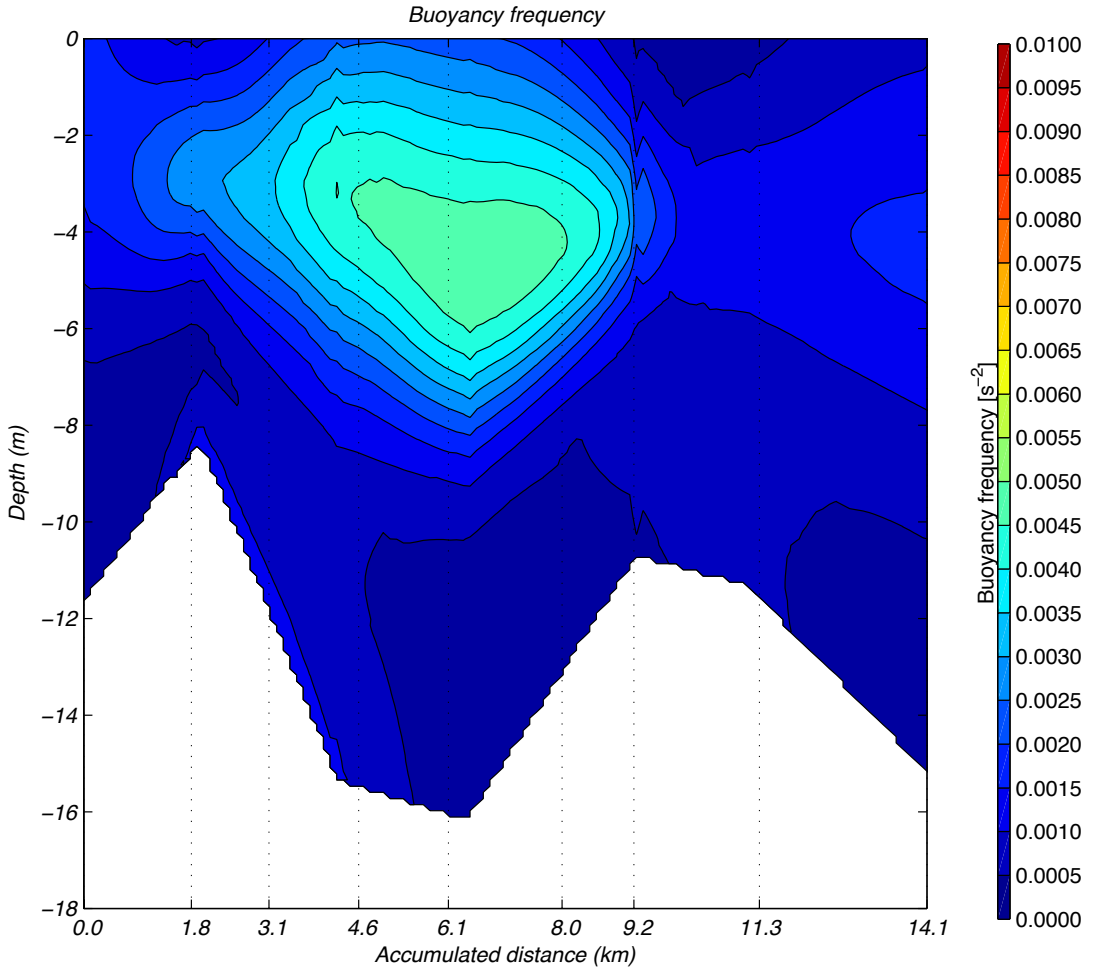

Figure 4.30 Buoyancy frequency observed on 2 November 2012. Maximum of about 4×10^{-3} was observed in the middle part of the domain.

4.4.3.4 Gradient Richardson number

The large value of the gradient Richardson number happened in the bottom layer of the domain (Figure 4.31). However, in surface layer a value of $Ri_g < 0.25$ was observed. Except for a small part at the bottom of the river mouth, the value of the gradient Richardson number was larger than 0.25 in the major part of the benthic boundary. In some places at the benthic layers, the gradient Richardson number exceeded 3.5.

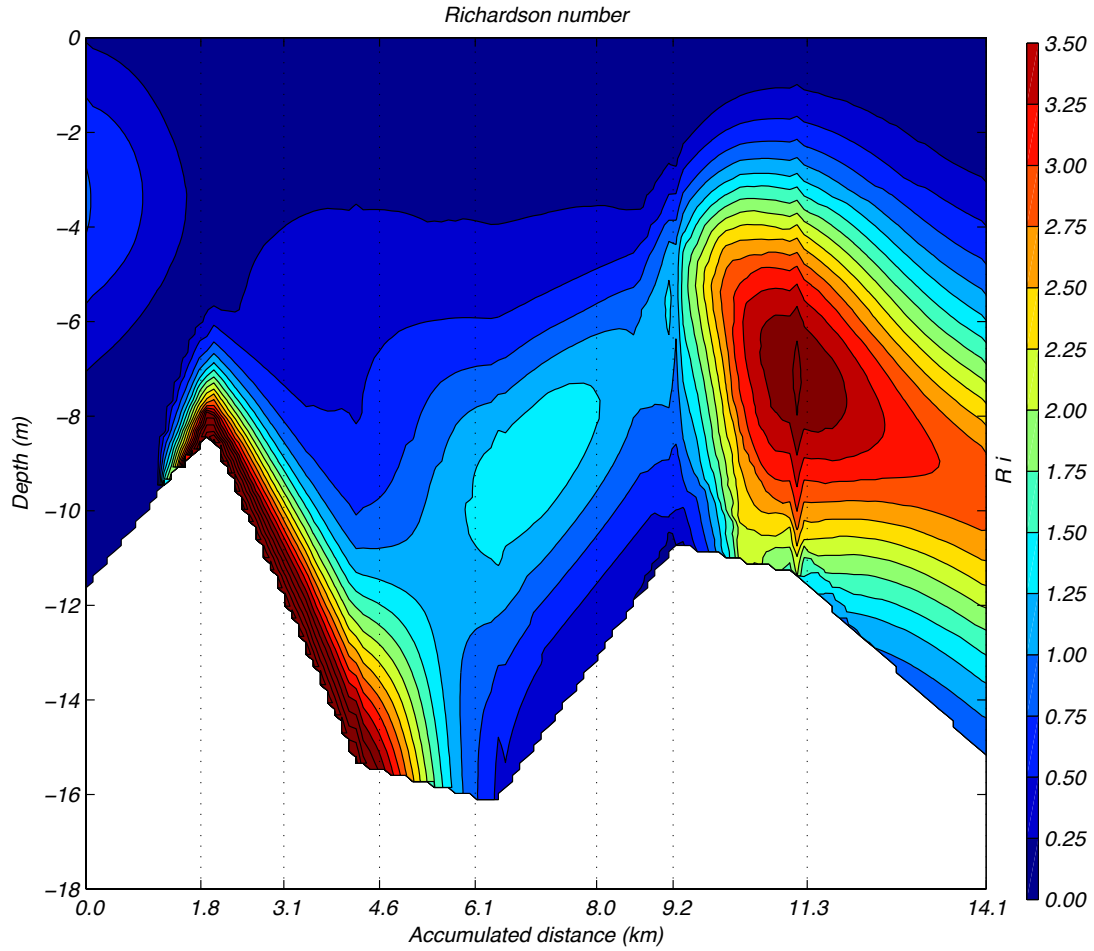

Figure 4.31 Gradient Richardson number observed on 2 November 2012. In the top layer the gradient Richardson number was less than 0.25.

4.4.4 Turbulent properties

4.4.4.1 Shear dissipation

The rate of dissipation of kinetic energy on 2 November 2012 is presented in Figure 4.32. A distinct layer with the dissipation rate of about 10^{-5} m^2s^{-3} was observed at the surface. Shear dissipation decreased with depth. However, at the benthic layer at a distance between 1.8 and 9 Km, the dissipation increased to 10^{-6} m^2s^{-3}. The minimum of about 10^{-8} m^2s^{-3} was observed at the layer close to the bottom in the upper part of the domain. In the middle of the domain a thin strip of a dissipation rate of about 10^{-7} m^2s^{-3} was observed in the benthic layer.

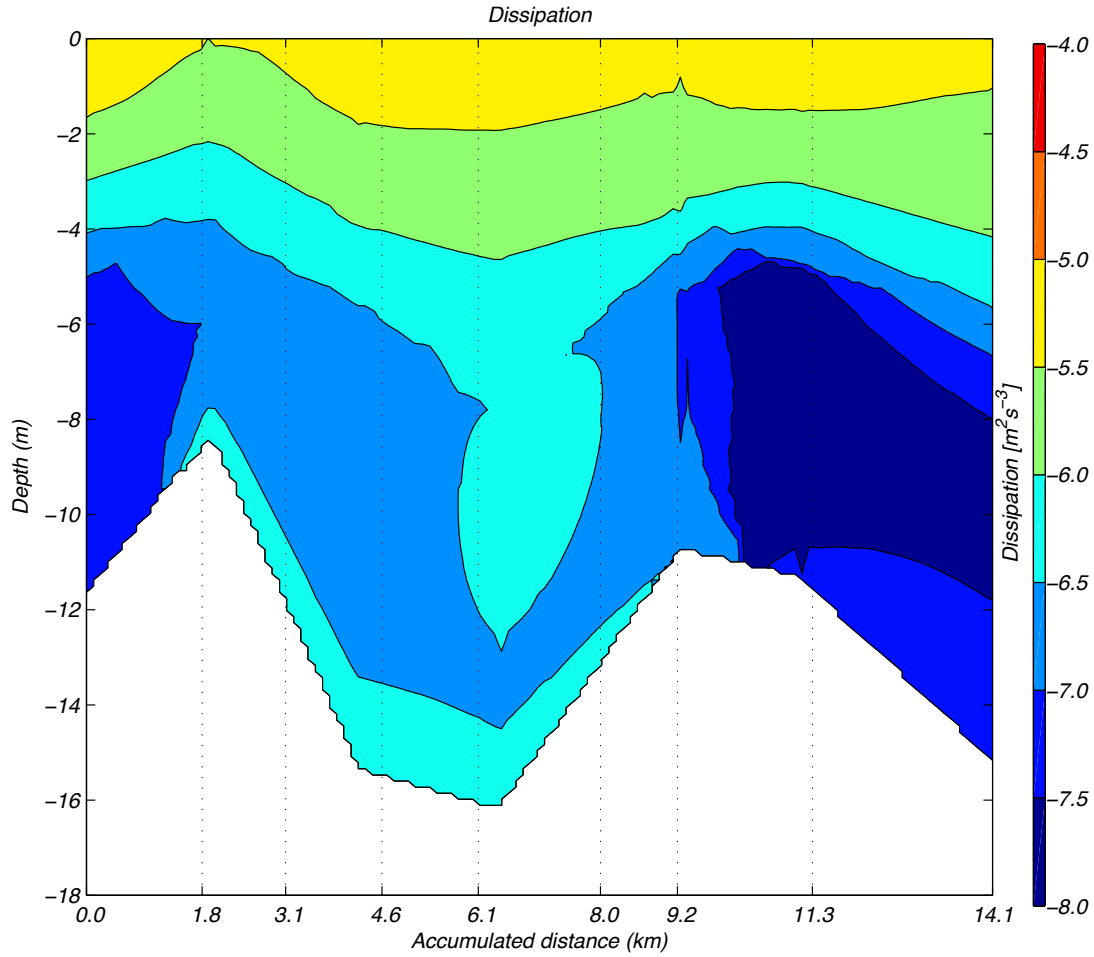

Figure 4.32 Shear dissipation observed in the domain on 2 November 2012.

4.4.4.2 Reynolds stress

The Reynolds stress $(\rho v_1' v_3')$ observed on 2 November 2012 is shown in Figure 4.33. The maximum of about 2 $kgm^{-1}s^{-2}$ was confined to a patch at the surface layer of the upper edge of the domain. The minimum of about -1 $kgm^{-1}s^{-2}$ was also observed in the surface layer but at the lower boundary. However, the majority of the domain showed a Reynolds stress in the range of -0.5-0.5 $kgm^{-1}s^{-2}$.

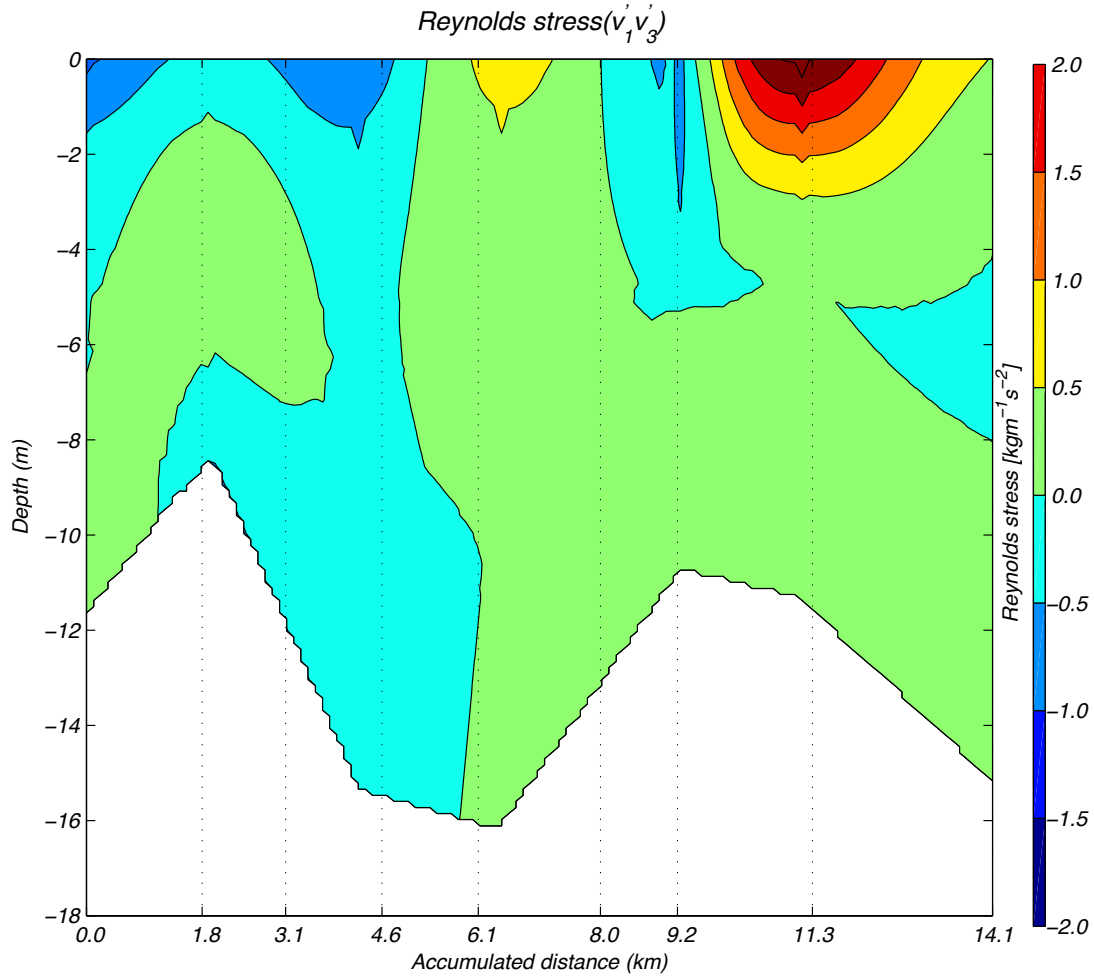

Figure 4.33 Reynolds Stress $(\rho v_1' v_3')$ observed during the field study on 2 November 2012.

Both maximum and minimum of Reynolds stress $(\rho v_2' v_3')$ were observed in the surface layer with magnitude of -2 and 2 $kgm^{-1}s^{-2}$. These extreme events were

confined to a limited local patch. While the event with the maximum extends from the surface to a depth of about 4 m, the event including the minimum was confined to a maximum depth of about 3m. In other parts of the study site there was a Reynolds stress between -0.5 and 0.5 $kgm^{-1}s^{-2}$.

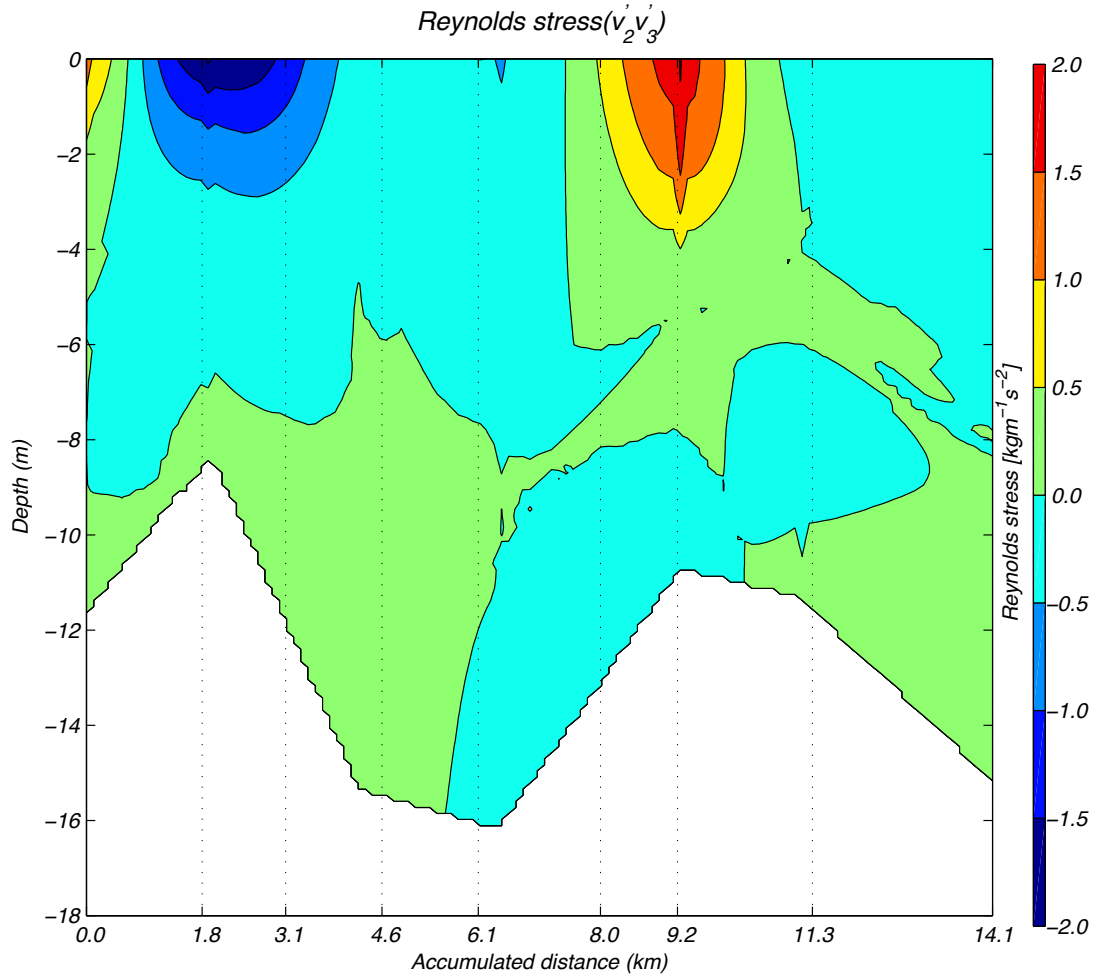

Figure 4.34 Reynolds stress $(\rho v_2' v_3')$ observed in the domain on 2 November 2012. A local minimum and maximum event was observed at the surface layer.

4.4.4.3 Buoyancy fluxes

Buoyancy fluxes contours observed during the field measurements on 2 November 2012 are presented in Figure 4.35. Fluxes varied between 10^{-8} and 10^{-6} m^2s^{-3}. There were a considerable patch of maximum values observed in the surface layers of the

middle part of the domain; however, a very tiny patch with a maximum value was observed at the surface of the river mouth. The minimum values were recorded at the bottom layer of both the upper and lower boundaries.

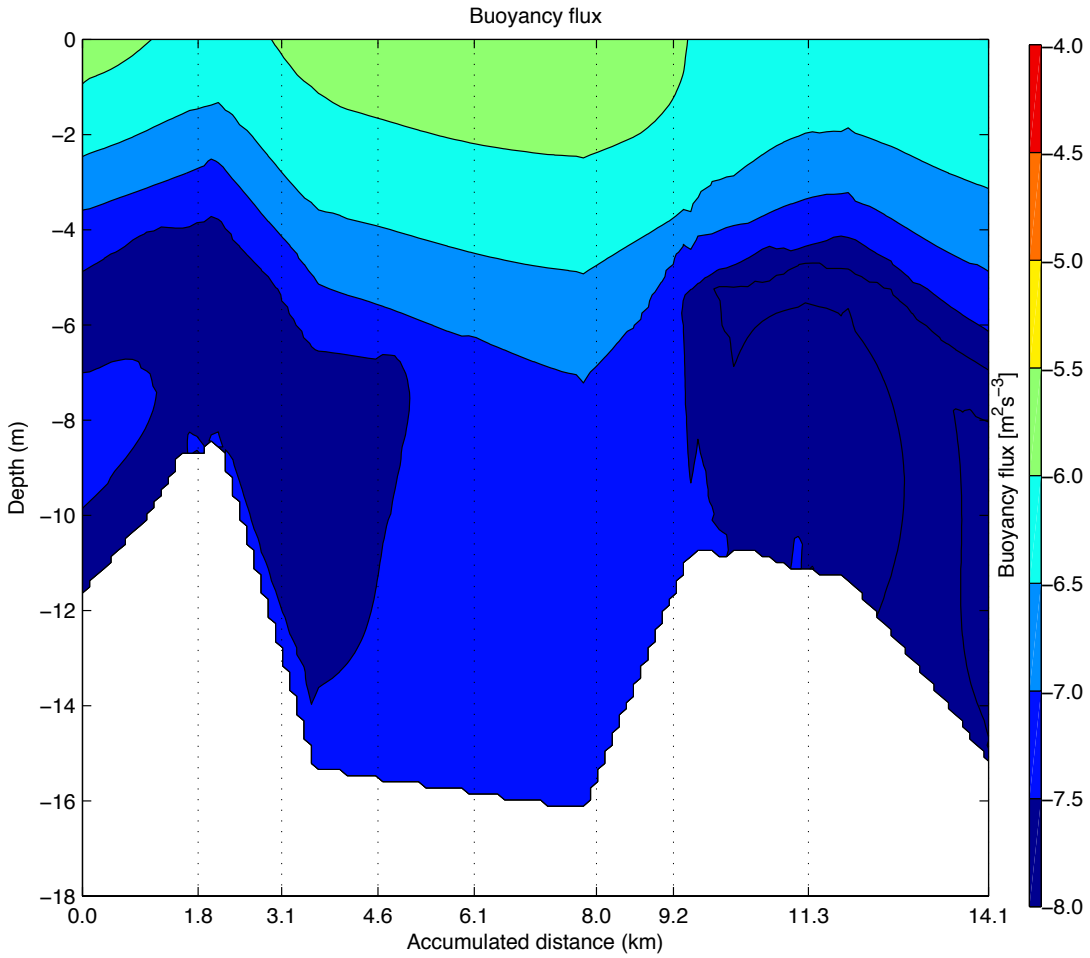

Figure 4.35 Buoyancy fluxes during the field measurement on 2 November 2012. The maximum value was observed in the surface layer.

4.5 Discussion

Salinity contours of three field measurements showed similar structure: a relatively strong pycnocline isolated a saline layer at the bottom from a brackish layer on the top, which is consistent with previous findings in the domain (Etemad-Shahidi and Imberger 2002). However, the intensity of stratification in the upper part was larger

than at the river mouth. At the final field study conducted in November, salinity in the surface layer of the upper boundary increased compared to the preceding field trip. This is due to a drop in rainfall in the region and consequently a decrease of fresh water inflow from tributaries and drains to the Swan River. Initial profiles of temperature showed nearly uniform thermal structure in the domain, consistent with previous findings (Etemad-Shahidi and Imberger 2002). The study conducted by (Etemad-Shahidi and Imberger 2002) was confined to a limited time. However, larger intervals between the three field trips showed the seasonal variations of water temperature within the estuary. Due to the increasing temperature during the hot season, the uniform structure was replaced with thermally stratified water. So, both diurnal thermal and seasonal stratification affected the estuary. Density curtains revealed that salinity was the dominant factor in changes in density. Contours showed a stable stratification throughout the field measurement, with a similar structure to salinity. Due to the lack of strong wind (and so wind energy), barotropic pressure was the dominant driving factor in the lower part of the Swan River Estuary. Among the different mean variables, dissolved oxygen underwent the most dramatic change. The curtains showed a dramatic drop in the dissolved oxygen concentration. This phenomenon can be explained due to reduced fresh water inflow to the river and algal bloom activity in the upper part of the Swan River (Stephens and Imberger 1996). The consequence is oxygen depletion in the water columns.

The maximum observed velocity in this study was larger than what was obtained $(0.2ms^{-1})$ by Etemad-Shahidi and Imberger (2002) in the Black Wall Reach in the Swan River. This difference is mainly due to the difference in the location of the study domain. Their study was conducted in the deepest part of the estuary, while the present study covers a larger area of the lower part of the Swan River Estuary. However, some locations of this research had a considerably shallower depth that caused larger velocity. Kay and Jay (2003) conducted a field measurement in a highly stratified estuary. They observed a horizontal velocity of about (0.8 – 1.25 ms^{-1}). The results of this study revealed that there is always an oceanward current during ebb tide. However, the velocity curtain highlighted that the maximum velocity occurred during the ebb tide (about the low tide) but before the slack time.

Shear contours showed similar structure (decrease with depth) to shear observed in a study by Etemad-Shahidi and Imberger (2002) in the Swan River Estuary. But they

observed smaller values than this study, probably due to a lesser velocity. The maximum shear usually coincided with a larger velocity. Yeates et al. (2013) observed a maximum shear value of about 1 s^{-1} at the surface layer in a stratified lake.

Shear dissipation showed a direct relationship to shear changes. Usually the maximum dissipation of turbulent kinetic energy happened in the area with higher shear values.

Reynolds stress had values consistent with a study by Chanson et al. (2012) during king tides in a small subtropical estuary. Moreover, the maximum value of Reynolds stresses happened within the region with higher shear values. Usually, in the region with higher Reynolds stresses, shear dissipation was larger. Lesser values of buoyancy fluxes compared to a larger value of shear dissipation verified that the bigger values of turbulent kinetic energy were lost to heat rather than a change of potential energy.

Moreover, It should be mentioned, as the profiling stations in different field trips were not at constant places; therefore, contouring procedure presented different bed profiles.

4.6 Summary

Three field measurements were conducted in the lower part of the Swan River Estuary during different tide conditions. Table 4.1 shows the detailed descriptions of the background environmental conditions during the field studies. These field measurements were carried out to provide comprehensive data sets for a numerical modelling or investigation of the performance of turbulent mixing closure schemes. To achieve the objectives, field studies were scheduled to present data sets covering all necessary data for initial (measurements on 27 August 2012) and validation (measurements on 8 October 2012) conditions. Further, supplementary data sets (measurements on 2 November 2012) were provided too. The mean variables of the second field measurement were used to compare the velocity field with direct measurements with the PFP and the inverse technique (Chapter 5) for validation of the field measurements. Microstructure profiles were used to study vertical mixing (Chapter 6).

Table 4.1 Detailed descriptions of environmental conditions during three field measurements

Date / Parameter	27 August 2012			8 October 2012			2 November 2012		
Experiment duration	Start 07:40		End 16:45	Start 07:40		End 13:10	Start 09:40		End 11:20
Tidal levels (m)	Min	Mean	Max	Min	Mean	Max	Min	Mean	Max
(24 hours)	-0.29	0.284	0.27	-0.25	0.22	0.19	-0.07	0.31	0.56
Tidal levels (m) (In the experiment)	-0.29	0.27	0.24	-0.24	0.06	-0.12	0.02	0.01	0.04
Wind speed (ms^{-1}) (24 hours)	0.0	0.53	1.77	0.57	1.75	3.35	1.93	1.68	3.26
Wind speed (ms^{-1}) (In the experiment)	0.0	0.46	1.40	0.90	1.56	2.84	2.25	2.32	2.56
Air temperature ($^{\circ}C$) (24 hours)	11.67	14.75	18.19	11.77	15.85	18.43	15.71	18.06	19.42
Air temperature ($^{\circ}C$) (In the experiment)	11.67	15.69	18.19	14.42	16.89	18.16	18.88	18.91	18.97
Water temperature ($^{\circ}C$) (24 hours)	16.67	17.31	17.92	18.15	19.08	20.5	19.33	20.11	20.78
Water temperature ($^{\circ}C$) (In the experiment)	16.67	17.21	17.92	18.22	18.87	20.33	19.75	19.90	20.06
Relative humidity (%) (24 hours)	60.82	82.45	92.40	54.48	71.33	84.88	59.57	71.10	84.11
Relative humidity (%) (In the experiment)	60.82	74.23	90.75	54.48	61.55	70.94	63.98	68.07	70.04

5
Estimating field velocity using a time dependent inverse method

Velocity measurement is one of the most important parts of field studies, as velocity directly affects turbulent fluxes. However, sometimes velocity measurement is a very difficult and tedious task. For example, in the study conducted by (Anokhin, Imberger et al. 2008), the velocity field was very complex due to some factors such as internal waves and surface winds. In this situation it is very important to use the method of measurement that presents acceptable results. In Chapter 4, a velocity field measured with the PFP was presented. However, the accuracy of a velocity field measured with the PFP should be verified with an alternative approach, so in this chapter a time-dependent inverse technique is introduced as an alternative to estimate the velocity field. It is based upon a two-dimensional advection-diffusion equation. To use the inverse method, profiles of passive tracers at profiling stations during consecutive transects are necessary. Using forward differencing in time and central differencing in space (FTCS), the equation of the advection-diffusion is solved based on measured data (Anokhin, Imberger et al. 2008). To achieve acceptable results using the inverse method, some factors such as accurate field measurements, intervals less than the diurnal tide period, suitable horizontal grid spacing between each profile station, and using passive tracers are essential. Results proved that velocity field generated by PFP and the inverse technique show similar direction. However, the magnitude is different, as the inverse method predicts average velocity during a particular time step, while the PFP measures instantaneous velocity. Moreover, using some tracers affected by some factors except the hydrodynamics of the estuary caused error in the inverse results (e.g. reactions).

5.1 Introduction

Direct measurement of the velocities of a large water body is one of the most problematic tasks in the study of the hydrodynamics of water environments. Sometimes in complex field environments, accurate measurement might be impossible. Different approaches are used to estimate flow velocity. One of the most useful techniques is the inverse method. It predicts flow velocity from the distributions of water properties. In other words, having profiles of a tracer in a different time and space reveals the dynamic and velocity field.

The inverse technique is built on a two-dimensional advection-diffusion equation (Anokhin, Imberger et al. 2008). Some assumptions, such as continuity, hydrostatic equilibrium, conservation of mass, quasi-geostrophic force, and the steady state of the system are considered in applying the inverse method (Wunsch 1987; Anohin, Imberger et al. 2006; Anokhin, Imberger et al. 2008).

By keeping the same grid space for both direct and inverse procedures, original information (flow velocity) with high accuracy is achieved. Choosing an appropriate grid space between the two profiling stations is one of the critical steps. Whatever the conditions, if the horizontal distance between two stations is chosen to be shorter, the results will be more accurate. Another important point in using the inverse technique is the duration of profiling (time of the field experiment). At least two profiles of tracers (mean variables) at each node (profiling station) during the field experiment are necessary. Moreover, to prevent any interfering factors it is suggested that the duration of the field measurement be smaller than the natural time scales of the water bodies. For example, a field experiment launched at high tide should be finished before low tide, or vice versa. The optimum situation is to perform sampling in more than two transects. The time interval between commencement of profiling at the first station and finishing at the last station is one transect.

Some studies (Wunsch 1978; Fiadeiro and Veronis 1984; Menke 1989) have defined the inverse model as an organized set of mathematical equations. Solving these equations provides useful information about the physical states of water bodies. The objective of these equations is to reduce the complexity of the velocity field. However, using these equations is based on the observational interferences of measurements of tracers in the study domain. Although usually salinity and

temperature have been used as tracers, Wunsch (1988) and (England and Maier‐Reimer 2001) have mentioned some other tracers such as the tritium-helium-3 pair, chlorofluorocarbons, radio-carbon , phosphate, nitrate, silicate and dissolved oxygen.

In fact all mathematic problems convert to a system of linear algebraic equations. These sets of equations can be either under-determined or over-determined. Fiadeiro and Veronis (1984) compared solutions of an advection-diffusion equation for under-determined (one tracer) and over-determined (two tracers) cases. Findings clearly showed that while in the under-determined system, inverted velocities and the resulting flow field was not representing the field data, the over-determined system presented acceptable results. Lee and Veronis (1989) developed a theory of inverse technique by introducing a third tracer and calculating the vertical diffusion coefficient besides field velocity. Calculations of the developed inverse model have shown that the system has to be strongly over-determined in order to obtain reasonable values for inverted coefficients and velocities.

The system of multiple tracers can be solved by different approaches. Menke (1989) used Singular Value Decomposition to solve the set of equations, whereas General Least Squares was proposed by Press et al. (1992). Fiadeiro and Veronis (1984) improved the inverse method. They proposed a method that predicted two components of velocity (longitudinal and vertical velocities). Later, Lee and Veronis (1989) made a comprehensive model that presented both flow velocity and diffusion coefficient. Ostrovskii and Piterbarg (1997) applied a modification on Fiadeiro and Veronis (1984) by using Maximum Likelihood Estimator (MLE) to estimate velocities and eddy diffusivity from tracer distributions. Maximum Likelihood Estimator is a procedure in which the parameters of statistical models are estimated. The application of MLE predicted accurate diffusivities if induced velocities were small compared to the diffusive term (Anokhin, Imberger et al. 2008).

One of the most important parameters that directly affect turbulent fluxes is velocity. As was presented in Chapter 4, velocity was measured directly with the PFP. However, one of the objectives of this research is to study turbulent mixing, outlined in Chapter 6. So, it is essential to measure velocity with highest accuracy. In fact, the objective of this chapter is to use the inverse method to validate the velocity field measured with the PFP by comparing it with the velocity field that has resulted from the inverse method. Tracers measured with the PFP during five consecutive transects on 8 October 2012 were used to run the inverse method. This chapter is arranged as

follows: firstly, the equation of transport is derived; secondly, the methodology is presented. Then the results and important outcomes are discussed. Finally, a summary of the chapter is presented.

5.2 Derivation of transport equation

The inverse approach is presented based on a two-dimensional advection-diffusion equation that states (Anokhin, Imberger et al. 2008):

$$\frac{\partial C}{\partial t} = -\nabla\left(vC\right) + \nabla^2\left(KC\right) + S \tag{5.1}$$

where S is source or sink term.

By rewriting (5.1):

$$\frac{\partial C}{\partial t} = -C\left(\frac{\partial v_1}{\partial x_1} + \frac{\partial v_2}{\partial x_2} + \frac{\partial v_3}{\partial x_3}\right) - \left(v_1\frac{\partial C}{\partial x_1} + v_2\frac{\partial C}{\partial x_2} + v_3\frac{\partial C}{\partial x_3}\right) + K_{x_1}\frac{\partial^2 C}{\partial x_1^2} + K_{x_2}\frac{\partial^2 C}{\partial x_2^2} + K_{x_3}\frac{\partial^2 C}{\partial x_3^2} + S \tag{5.2}$$

Assuming the system to be 2-D (neglecting the y-component) and the diffusion in the x-direction to be negligibly small compared to the advection, it can be written:

$$\frac{\partial C}{\partial t} = -C\left(\frac{\partial v_1}{\partial x_1} + \frac{\partial v_3}{\partial x_3}\right) - \left(v_1\frac{\partial C}{\partial x_1} + v_3\frac{\partial C}{\partial x_3}\right) + K_{x_3}\frac{\partial^2 C}{\partial x_3^2} + S \tag{5.3}$$

For a case with no sources or sinks (S) of fluid within the study area, the transport equation can be rewritten as follows:

$$\left(v_1\frac{\partial C}{\partial x_1} + v_3\frac{\partial C}{\partial x_3}\right) = -\frac{\partial C}{\partial t} + K_{x_3}\frac{\partial^2 C}{\partial x_3^2} \tag{5.4}$$

Considering the conservation of mass and the definition of stream function that states:

$$\frac{\partial v_1}{\partial x_1} + \frac{\partial v_3}{\partial x_3} = 0\,, \qquad v_1 = \frac{\partial \psi}{\partial x_3}\,, \qquad v_3 = -\frac{\partial \psi}{\partial x_1} \tag{5.5}$$

Rewriting velocities by using stream function:

$$\left(\frac{\partial \psi}{\partial x_3}\frac{\partial C}{\partial x_1} - \frac{\partial \psi}{\partial x_1}\frac{\partial C}{\partial x_3}\right) = -\frac{\partial C}{\partial t} + K_{x_3}\frac{\partial^2 C}{\partial x_3^2} \tag{5.6}$$

where C is the tracer concentration, v_1 is the horizontal velocity (longitudinal velocity), v_3 is the vertical velocity, K_{x_3} is vertical eddy diffusivity, and ψ is the stream function.

As the horizontal advection term was one order of magnitude bigger than the eddy diffusivity $K_{x_1}\frac{\partial^2 C}{\partial x_1^2}$, it was neglected. Moreover, transverse transports across the estuary were neglected too. So, the important factor to be calculated was vertical eddy diffusivity, which is one of the advantages of using the inverse method.

Using the stream function and rewriting different parts in terms of finite difference equations yields:

$$\frac{1}{2}\left\{\left(\frac{\psi_{12}-\psi_{11}}{\Delta x_3}\frac{C_{22}-C_{12}}{\Delta x_1}-\frac{\psi_{21}-\psi_{11}}{\Delta x_1}\frac{C_{22}-C_{21}}{\Delta x_3}\right)+\left(\frac{\psi_{22}-\psi_{21}}{\Delta x_3}\frac{C_{32}-C_{22}}{\Delta x_1}-\frac{\psi_{22}-\psi_{12}}{\Delta x_1}\frac{C_{23}-C_{22}}{\Delta x_3}\right)\right\}=$$

$$-\frac{C_{22}^{t2}-C_{22}^{t1}}{\Delta t}+K_{x_3}\frac{\left(C_{21}+C_{23}-2C_{22}\right)}{\Delta x_3^2} \qquad (5.7)$$

Rearranging different terms it can be written:

$$\left(\psi_{12}C_{22}-\psi_{11}C_{22}-\psi_{12}C_{12}+\psi_{11}C_{12}-\psi_{21}C_{22}+\psi_{11}C_{22}+\psi_{21}C_{21}-\psi_{11}C_{21}\right)+$$

$$\left(\psi_{22}C_{32}-\psi_{22}C_{22}-\psi_{21}C_{32}+\psi_{21}C_{22}-\psi_{22}C_{23}+\psi_{12}C_{23}+\psi_{22}C_{22}-\psi_{12}C_{22}\right)=$$

$$=-\frac{2\Delta x_3\Delta x_1}{\Delta t}\left(C_{22}^{t2}-C_{22}^{t1}\right)+K_{x_3}\frac{2\Delta x_1}{\Delta x_3}\left(C_{21}+C_{23}-2C_{22}\right) \qquad (5.8)$$

By definition of $xx=\Delta x_{11}\Delta x_{12}$, $A_1=\Delta x_{11}(\frac{\Delta x_{11}+\Delta x_{12}}{2})$, and $A_2=\Delta x_{12}(\frac{\Delta x_{11}+\Delta x_{12}}{2})$ the equation can be written:

$$\left(A_2\left(\psi_{12}-\psi_{11}\right)\left(C_{22}-C_{12}\right)-xx\left(\psi_{21}-\psi_{11}\right)\left(C_{22}-C_{21}\right)\right)+$$
$$\left(A_1\left(\psi_{22}-\psi_{21}\right)\left(C_{32}-C_{22}\right)-xx\left(\psi_{22}-\psi_{12}\right)\left(C_{23}-C_{22}\right)\right)= \qquad (5.9)$$
$$2\Delta x_3\Delta x_{11}\Delta x_{12}\frac{\left(\Delta x_{11}+\Delta x_{12}\right)}{2}\left\{-\frac{C_{22}^{t2}-C_{22}^{t1}}{\Delta t}+K_{x_3}\frac{\left(C_{21}+C_{23}-2C_{22}\right)}{\Delta x_3^2}\right\}$$

By rearrangement of (5.9) a new form of equation is presented:

$$\left(\psi_{12}C_{22}A_2-\psi_{11}C_{22}A_2-\psi_{12}C_{12}A_2+\psi_{11}C_{12}A_2-\psi_{21}C_{22}xx+\psi_{11}C_{22}xx+\psi_{21}C_{21}xx-\psi_{11}C_{21}xx\right)+$$

$$\left(\psi_{22}C_{32}A_1-\psi_{22}C_{22}A_1-\psi_{21}C_{32}A_1+\psi_{21}C_{22}A_1-\psi_{22}C_{23}xx+\psi_{12}C_{23}xx+\psi_{22}C_{22}xx-\psi_{12}C_{22}xx\right)=$$

$$2\Delta x_3\Delta x_{11}\Delta x_{12}\frac{\left(\Delta x_{11}+\Delta x_{12}\right)}{2}\left\{-\frac{C_{22}^{t2}-C_{22}^{t1}}{\Delta t}+K_{x_3}\frac{\left(C_{21}+C_{23}-2C_{22}\right)}{\Delta x_3^2}\right\} \qquad (5.10)$$

Eventually the transport equation is presented as:

$$\psi_{12}\left(\frac{\left(C_{22}-C_{12}\right)}{\Delta x_{11}}+\frac{\left(C_{23}-C_{22}\right)}{\left(\Delta x_{11}+\Delta x_{12}\right)/2}\right)+\psi_{22}\left(\frac{\left(C_{32}-C_{22}\right)}{\Delta x_{12}}+\frac{\left(C_{22}-C_{23}\right)}{\left(\Delta x_{11}+\Delta x_{12}\right)/2}\right)=$$

$$=-\frac{2\Delta x_3}{\Delta t}\left(C_{22}^{t2}-C_{22}^{t1}\right)+K_{x_3}\frac{2}{\Delta x_3}\left(C_{21}+C_{23}-2C_{22}\right) \qquad (5.11)$$

5.3 Methodology

A graphical description of the inverse method is presented in Figure 5.1. Using forward differencing in time and central differencing in space (FTCS), the equation of the advection-diffusion is discretized (Anokhin, Imberger et al. 2008). The result is a linear equation $Ax=b$, where A is a sparse matrix including the spatial gradients derived from first tracer transect, vector b defines the rate of tracer over the time interval of profiling, and x are the unknowns such as stream function. The detailed description of the method can be found in (Anokhin, Imberger et al. 2008).

The domain of the field measurements on 8 October 2012 consisted of 10 profiling stations with an average horizontal distance of about 200 m between each station. Velocity was calculated in the domain by inverting the transects of tracers measured with the PFP. The main criterion for choosing a tracer was not only to present the advective/diffusive process but also to keep its properties during the field experiment. So, sampling was conducted during the second half of ebb tide to avoid interference with the inverse method. The duration of the field experiment (six hours) was large enough to allow the tracers to move an appreciable distance, but short compared to the diurnal tidal period. The profiles of tracers were recorded in five consecutive transects. The time interval between each transect was 1-1.5 hours. Implicit was the assumption that the tracers, affected by chemical or biological activity, were changed predominantly by advection, rather than the reaction of the duration between transects.

Salinity, temperature, dissolved oxygen, pH and turbidity were used to run the inverse method. Having five different transects, there were 10 different possibilities for each pair of transects. For example, if (a) was selected as the first transect, the possibilities for a pair of transects would be (a-b), (a-c), (a-d), and (a-e) where b, c, d, e are second, third, fourth and fifth transects, respectively. Once a pair of transects

was selected, the appropriate combinations of tracers were chosen. Caution was exercised in choosing a tracer, especially for those affected by chemical or biological activities during sampling. For example, if photosynthesis increases dissolved oxygen in some transects, using dissolved oxygen deflects the inverse method from its path.

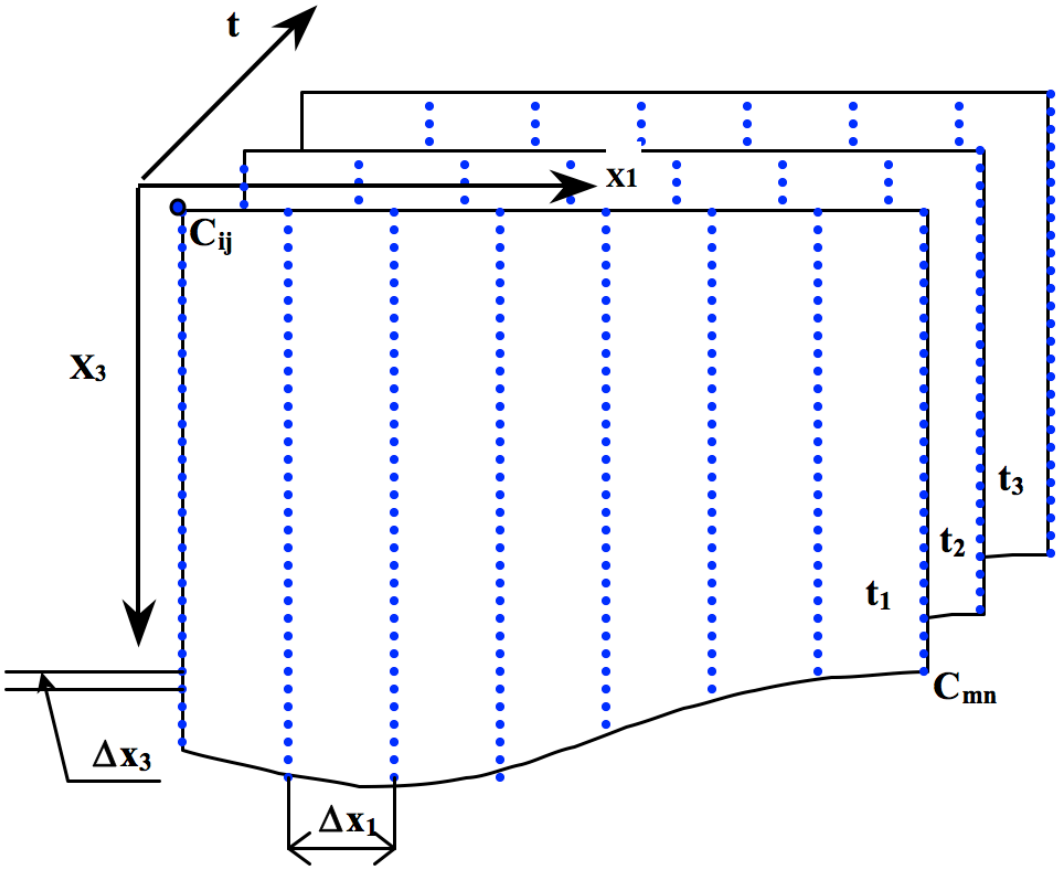

Figure 5.1 Graphical description of the inverse method.

5.4 Results and discussion

5.4.1 Mean variables (tracers)

Contours of tracers during five consecutive transects are presented in panel (a) (first transect), panel (b) (second transect), panel (c) (third transect), panel (d) (fourth transect), and panel (e) (fifth transect).

5.4.1.1 Salinity

Salinity contours during different transects showed a similar structure to each other. A relatively strong pycnocline isolated a saline layer at the bottom from a brackish layer on the top (Figure 5.2). Salinity contours during different transects showed in the bottom of the upper part of the domain a salt intrusion moved toward the river mouth. This salt intrusion originated from ocean water propagated during high tide to the upper part of the Swan River Estuary. The salt intrusion caused a stronger stratification in the domain that persisted in time due to a lack of enough energy to achieve mixing in the water column. There was a weak stratification zone (at relative distance between 2.16 and 2.59 Km) (Figure 5.2a-d); however, this weak stratified zone was replaced with a strong stratification at the end of the study (Figure 5.2e). Except for the mentioned area, other parts of the domain were strongly stratified. In the major part of the domain there was an oceanward current throughout the time of measurements. Barotropic pressure was the dominant driving force in the area with oceanward flow (positive velocity). However, at the bottom of the river mouth baroclinic pressure outweighed the barotropic pressure. The consequence was a persisting salt intrusion at that spot.

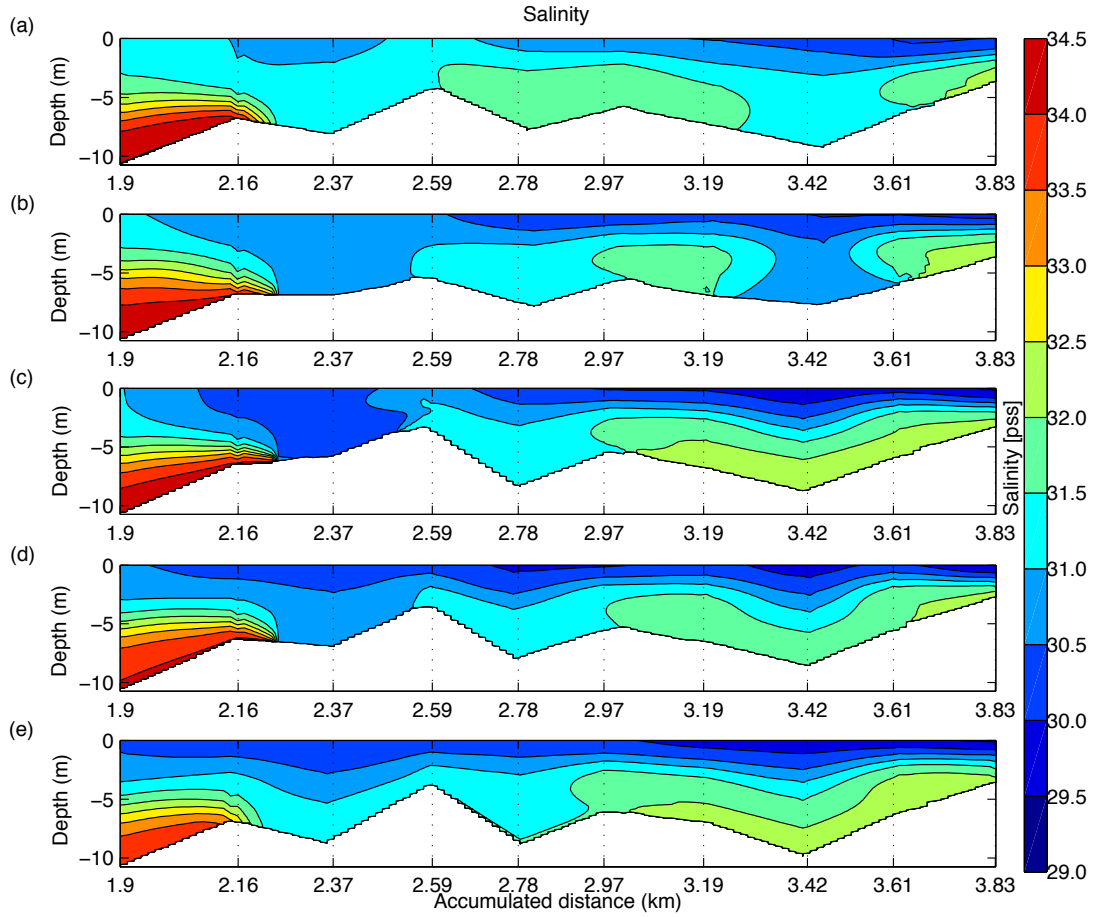

Figure 5.2 Salinity curtains observed with the PFP on 8 October2012. Panels **(a-e)** show salinity changes in five consecutive transects. The start time and finish time for each transect was: Firs transect 7:42-8:26, second transect 9:02-9:52, third transect: 10:08-10:55, fourth transect 11:16-11:59, and fifth transect 12:28-13:10.

5.4.1.2 Temperature

Temperature curtains are presented in Figure 5.3. Initial profiles of temperature showed nearly uniform thermal structure in the domain (Figure 5.3a). From the second transect onward, the uniform structure was replaced with thermal stratification, however, the difference between the surface and the bottom temperature was less than 1 $^{\circ}C$ (Figure 5.3b-e). Water temperature increased due to the effects of air temperature and solar radiation, which is clearly evident in the temperature of the surface layer. Field measurements were conducted on 8 October 2012 under a clear sky. The air temperature increased dramatically throughout the field measurements. Moreover, the field experiment was performed in an area with

small to medium depth that amplified the effects of solar radiation on water temperature. Solar radiation could penetrate a considerable depth into the water column.

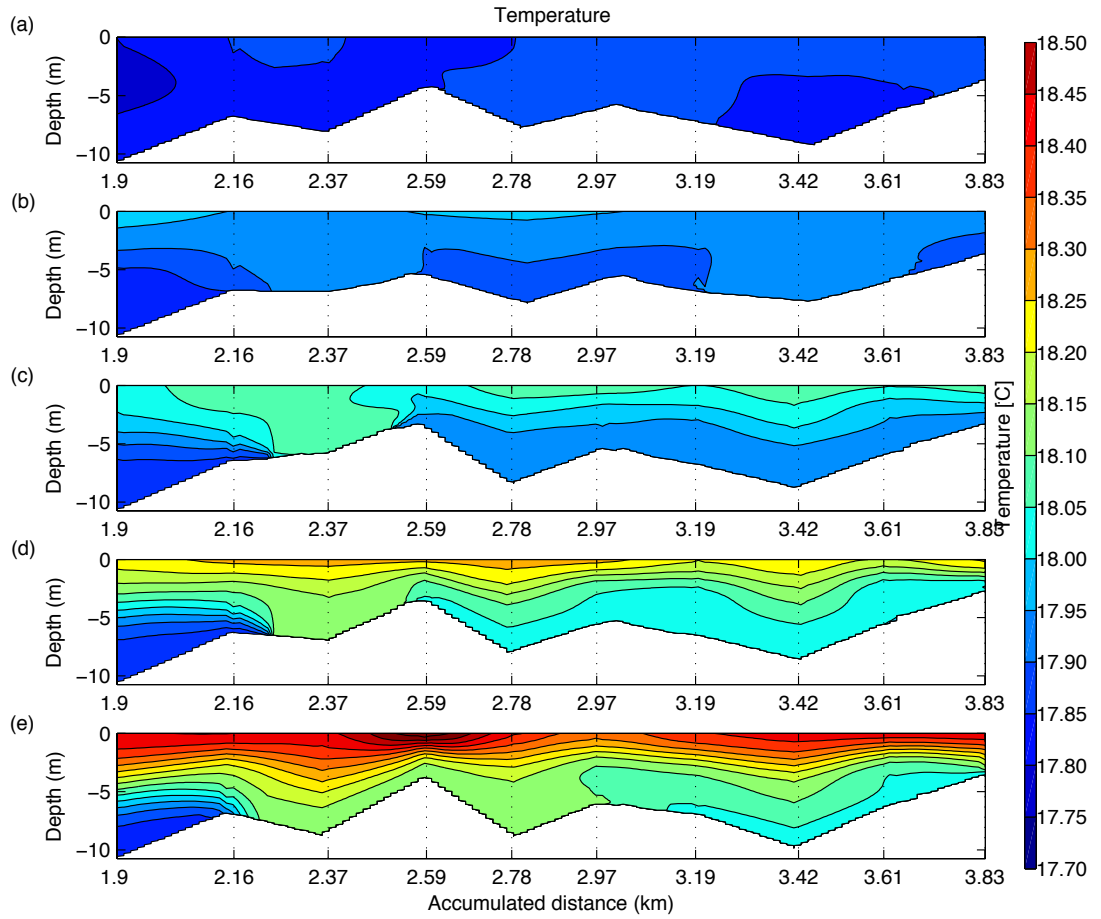

Figure 5.3 Temperature contours measured with the PFP on 8 October2012 during five consecutive transects. Panels **(a-e)** show temperature changes in each transect.

5.4.1.3 Density

Density contours showed a stable stratification throughout the field measurement, which was similar to salinity (Figure 5.4). Water with greater density filled the domain from both sides of its boundaries. As time elapsed from the first to last transects, the intensity of stratification increased. The maximum density was observed at the bottom of the river mouth, while minimum density was observed in the surface layers. The difference in density between the surface and the bottom was about 4 kgm^{-3}.

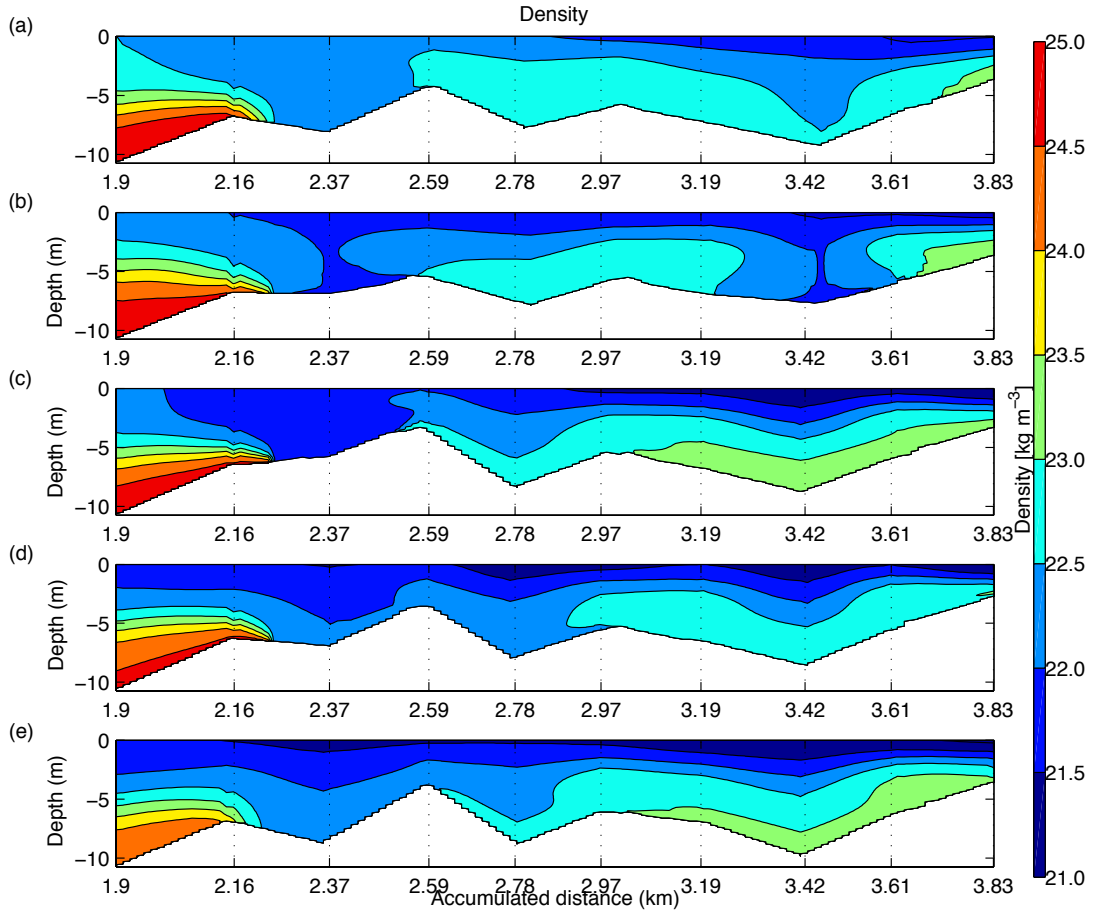

Figure 5.4 Density curtains observed in the domain on 8 October 2012. All transects are shown in panel **(a-e)**.

5.4.1.4 Dissolved oxygen

Figure 5.5 shows the variability of dissolved oxygen concentration in the study domain. The concentration of dissolved oxygen increased during the measurements. The peak concentration was observed in the surface layer (> 9.10 mgl^{-1}). Dissolved oxygen increased during the time of sampling. Previous research by Stephens and Imberger (1996) in the Swan River Estuary stated that blooms of dinoflagellate in summer time could be responsible for this increase. In this study, measurements were conducted in ebb tide; therefore, oxygen-rich ocean water didn't affect the amount of oxygen in the estuary. As water temperature increases, its capacity to keep gases is reduced, which is contrary to observations on 8 October 2012. So the reason of increase in the concentration of dissolved oxygen can be explained by saying that favourable solar radiation and water temperature might make desirable conditions for

species that produce oxygen by increasing the photosynthetic rate during the day.

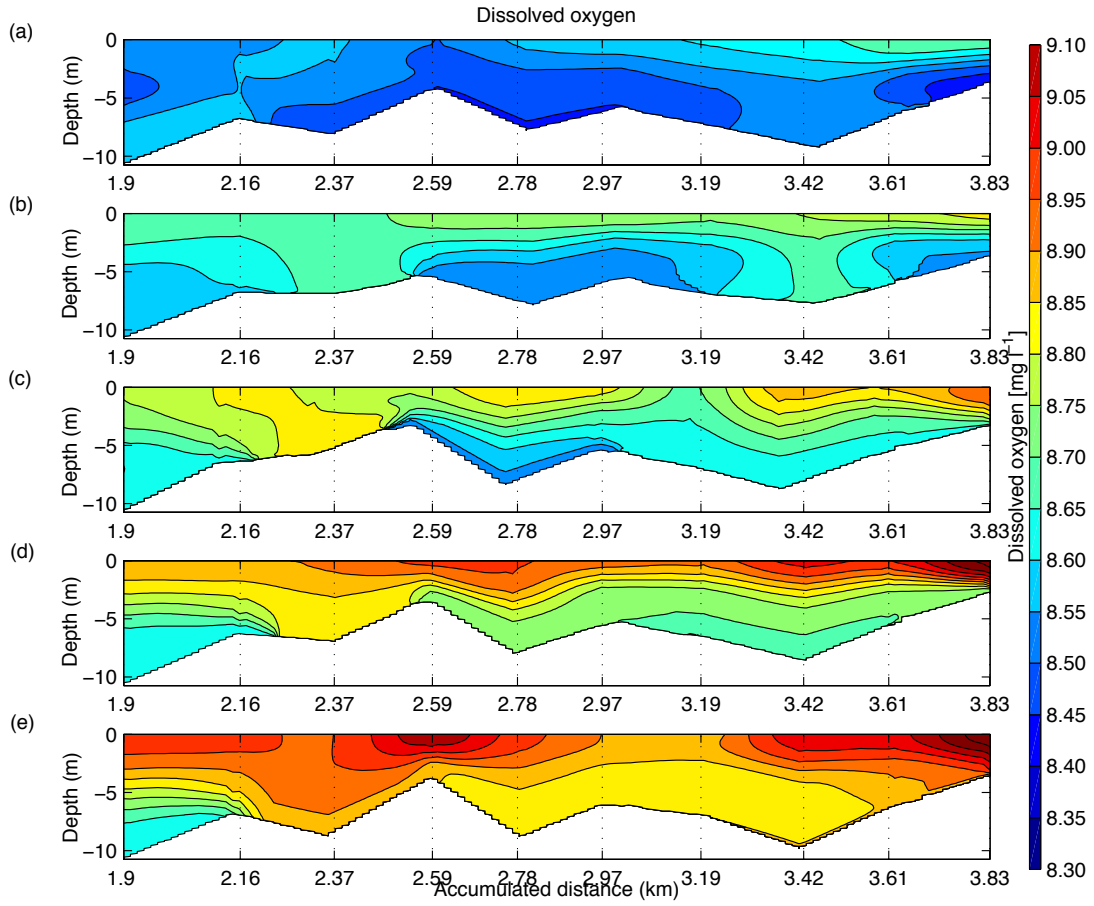

Figure 5.5 Dissolved oxygen contours. The concentrations of dissolved oxygen during different rounds of samplings measured with the PFP on 8 October 2012 are presented in panel **(a-e)**.

5.4.1.5 Turbidity

Turbidity contours are presented in Figure 5.6. The maximum turbidity was observed near the riverbed during the third transect (Figure 5.6c). The least turbidity was recorded in the first transect. The turbidity varied between values with a maximum larger than 1 FTU and minimum of about 0.5 FTU. The maximum turbidity was observed near the riverbed and coincided with maximum salinity, which is consistent with the Hamilton et al. (2001) study in the estuary.

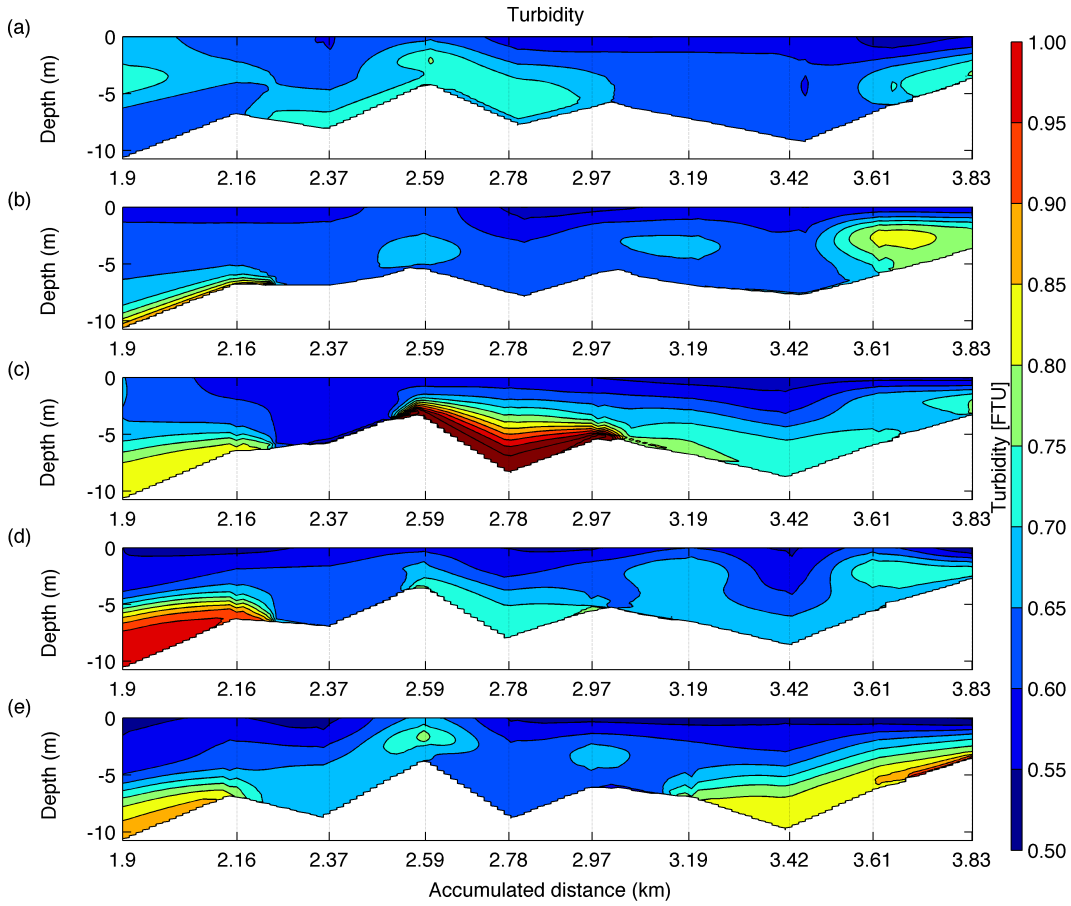

Figure 5.6 Turbidity curtains measured with the PFP in lower part of Swan River Estuary.

5.4.1.6 pH

The pH increased throughout the period of study (Figure 5.7). The minimum pH was observed during the first transect (Figure 5.7a) in the upper part of the domain with a magnitude of about 8.24. In the first three transects the maximum pH (8.34) was observed at the bottom of the river mouth. However, in the fourth transect the maximum was recorded at the bottom of the river mouth as well as at the surface layer of the upper boundary. During the last transect the domain was filled with water with either pH of about 8.32 or pH of about 8.33. The bottom layers in the entirety of the domain had a pH of about 8.33. The maximum was reduced, compared to previous transects.

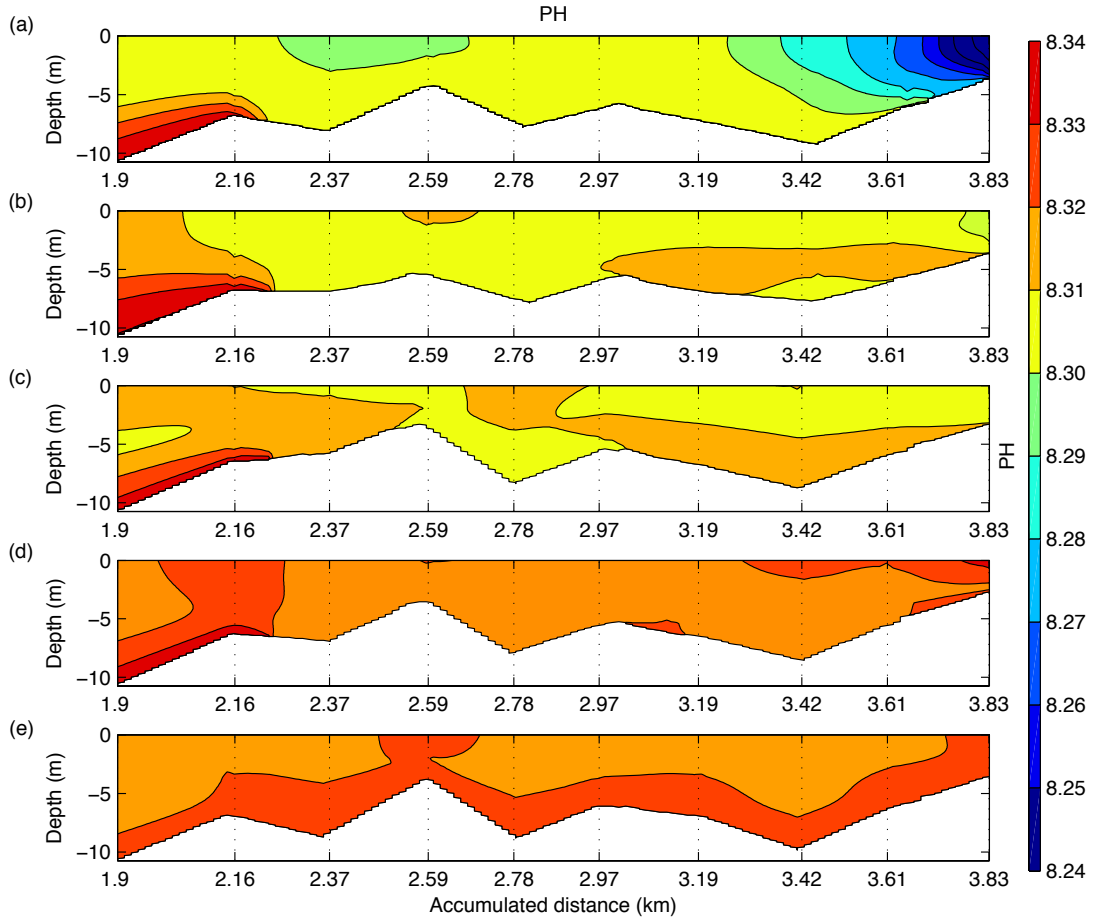

Figure 5.7 pH profiles. Observed pH in the lower part of the Swan River Estuary in the domain on 8 October 2012. Panel **(a-e)** show consecutive transects of pH.

5.4.2 Velocity field

Longitudinal velocity that has resulted from the inverse technique is presented in Figure 5.8 where positive velocity indicates an oceanward flow. The first run was conducted by choosing the first and second transects. The interval between these two transects was about one hour. Different combinations of tracers (mean variables) were tried. The optimum result was obtained when the inverse method ran with all five tracers. The result showed that time averaged horizontal velocity in the surface layer varied between 0.1 and 0.2 ms^{-1} (Figure 5.8a), which is consistent with the spatial changes of the salinity contours during the interval of about one hour.

The performance of the inverse technique was examined for another pair of transects. The fourth and fifth transect were chosen to run the inverse method. Figure 5.8b

presents the time-averaged longitudinal velocity for the two last transects. Different combinations of tracers were examined. Finally, the optimum result was achieved by using salinity, turbidity, and pH. The inverse method showed a larger current at the bottom of the upper boundary with a positive velocity heading to the ocean. This circumstance is consistent with the variability of salinity contours throughout the time interval between the fourth and fifth transects.

Velocity that resulted from the inverse method (Figure 5.8) and the PFP (Figure 4.15) showed similar trends. They showed that water flowed to the ocean (positive velocity). However, the magnitude of these two methods was different. The interpretation is that the observed velocity obtained with the PFP shows instantaneous velocity, while the inverse method presents an average velocity during the interval between two transects.

Although accurate measurements, suitable time intervals, and precise grid space are central to the inverse technique, the combinations of tracers play an indispensible role in this inverse method. In other words, the tracers that are influenced by external parameters except the hydrodynamics of natural waters deflect the method from producing accurate results. For example, application of the inverse technique for the pair of fourth and fifth transects was deflected by using water temperature and dissolved oxygen, because water temperature varied due to the influence of the air temperature and the solar radiation during the period of study. Moreover, dissolved oxygen was affected by biological activity from the first to last transect. Although the magnitude of the two methods was different due to reasons already mentioned, the direction of flow from the inverse method and the PFP was similar, showing the accuracy of measurements with the PFP.

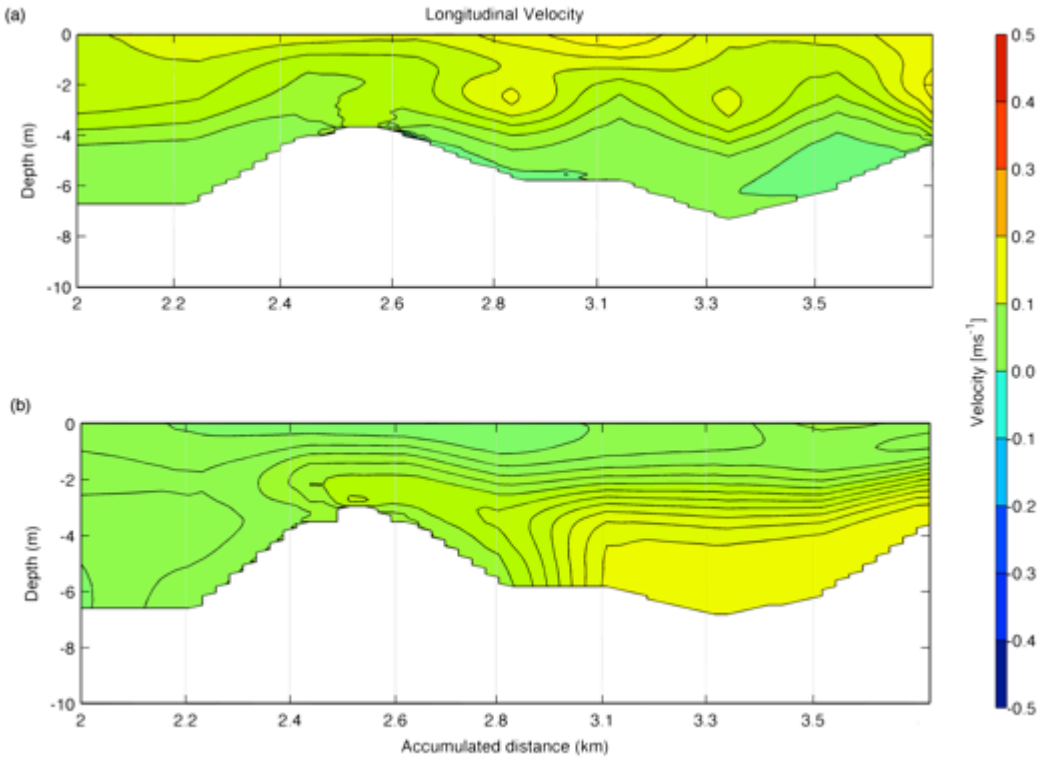

Figure 5.8 Inverse velocity field. (a) Averaged longitudinal velocity that resulted from inverting the tracers field between the first and second transect. (b) Averaged longitudinal velocity using the inverse method for fourth and fifth transects.

5.5 Summary

A field trip was conducted in the lower part of the Swan River Estuary on 8 October 2012. The sampling was repeated in five consecutive transects. The profiling stations were approximately 200 m apart from each other. The average time intervals of each transect was about six hours. The collected profiles of tracers such as salinity, temperature, dissolved oxygen, turbidity and pH with the PFP were used to run a time-dependent inverse method to estimate flow velocity. Using the first and second transects, the inverse method was applied to estimate field velocity with a combination of all tracers. The results showed a contour of positive velocity (oceanward currents). The method was examined for another pair of transects (transect four and five). The combination of all tracers showed that the inverse method could not predict velocity well. Different combinations of tracers were examined. The optimum result was achieved by using a combination of salinity,

turbidity and pH because the water temperature and dissolved oxygen were affected by factors other than estuary hydrodynamics. Water temperature was increased by air temperature and solar radiation. Photosynthesis increased dissolved oxygen concentration. Therefore, using water temperature and dissolved oxygen was a source of error that mentioned as a limitation in using inverse method. Moreover, it was conclude that by increasing the distance between each profiling the accuracy of the model is decreased. Comparison between velocities estimated from the PFP and the inverse method showed positive velocity (oceanward current) in both methods, verifying the results of the PFP. However, the magnitude was different as the PFP measures instantaneous velocity while the inverse technique presents average velocity during the time interval between two transects.

6
Vertical mixing in stratified shear flow

Turbulence plays an indispensible role in stratified water. Turbulence influences momentum and heat transfer, vertical transport of organic and inorganic substances and the aquatic habitat for microorganisms. Vertical transport of contaminants, heat and nutrients is controlled by vertical fluxes. Therefore, vertical transport (diapycnal mixing) is very important not only for geophysical science but also for environmental engineering. It plays an indispensible role in the understanding of aquatic environmental ecology, as it influences the nutrient cycle that is crucial for ecological chains. Moreover, it is very important for hydrodynamics and quality modelling of water bodies. Vertical mixing in numerical models is usually presented by a turbulence closure scheme due to nonlinear interactions between the shear production of turbulence, dissipation of kinetic energy and buoyancy fluxes. In fact, closure schemes estimate the rate of vertical mixing based upon some measureable variables. However, different closures use different variables. For example, some of the closures present eddy diffusivity as a variable dependent on gradient Richardson number, while others estimate the vertical mixing based on both gradient Richardson number and Schmidt number (turbulent Prandtl number Pr_t). In this chapter, vertical mixing is studied based on microstructure data collected in the estuary and a thermally stratified lake. Eddy diffusivity of mass and turbulent viscosity as a function of gradient Richardson number presented three different ranges, a weak stratification regime ($Ri_g < 0.01$), an intermediate range ($0.01 < Ri_g < 0.25$) and more stable regime ($Ri_g > 0.25$). Within the first two regions, eddy diffusivity was larger than eddy viscosity. However, for $Ri_g > 0.25$ in some places eddy viscosity was larger than eddy diffusivity. The variability of Pr_t versus Ri_g was studied in four different zones where: (1) down-gradient buoyancy and momentum fluxes (2) down-gradient buoyancy fluxes and up-gradient momentum fluxes (3) up-gradient buoyancy and momentum fluxes (4) up-gradient buoyancy fluxes and down-gradient momentum fluxes. The figures showed that due to a large population in each zone, neglecting the up-gradient fluxes in turbulence studies is not an appropriate approach. While the Schmidt number increased with increasing gradient Richardson number, it showed an asymptote in $Ri_g < 0.01$.

6.1 Introduction

Stratification in natural waters usually happens when water with different mass builds several distinct layers. The stratification can be attributed to the difference in salinity (halocline), temperature (thermocline), and density (pycnocline). Apart from the mechanism by which stratification occurred, heavier water always sits underneath less dense water. So, distinct layers are observed in water columns: a well mixed surface layer, an intermediate zone with a high gradient in density or temperature and a weakly stratified zone under the highly-stratified zone (Boehrer and Schultze, 2008). Further, there is a fully mixed zone above the bottom of the water body that is called the turbulent benthic boundary layer (Marti and Imberger, 2006). During the warm season, solar heating at the surface acts to increase the intensity of stratification provided there is a large depth of water (Boehrer and Schultze, 2008), however, wind energy causes a natural convective effect during the cooling period by forcing vertical circulation and bottom boundary frictions erode the stratification (Marti and Imberger, 2006; Yeates, 2007). Some water bodies experience stratification for a particular time period, others might be always under stratification and do not undergo a complete overturn (Boehrer and Schultze, 2008). During stratification, horizontal transport rates are usually several orders of magnitudes bigger than vertical transport (Imboden and Wüest, 1995). Stratification acts as barrier to vertical mixing. This can affect primary production in the surface area (Spigel and Imberger, 1987). Due to stratification, decomposition of sediment materials in the hypolimnion causes nutrient release in the bottom layers. At the same time, photosynthesis occurs in the top layers. For organisms to survive and continue their activities, they must be supplied with both light and nutrients. While the availability of light is supported by solar radiation in the surface layer, nutrients can be entrained from the bottom to the upper layers by diapycnal mixing that overcomes the intense density gradient.

Events that erode stratification by producing buoyancy fluxes have been studied by researchers for many years (Boehrer and Schultze, 2008). The main role of buoyancy fluxes is to supply nutrients from the enriched benthic bottom water to primary producers in the surface and in the opposite direction to supply enriched oxygen layers to anoxia zones in the bottom layers. Several methods have been proposed to estimate the mixing rate, which usually is referred to as turbulent diffusivity of mass

K_ρ. All the diverse approaches can be grouped into direct and indirect methods. For a direct method using field measurement of turbulent fluxes, vertical eddy diffusivity of mass is given by:

$$K_\rho = -\frac{\overline{v_3' \rho'}}{d\rho / dx_3} \tag{6.1}$$

One of the most widely used indirect methods is the Osborn equation (Osborn, 1980). Using Ellison's theoretical arguments (Ellison, 1957), he assumed for a steady flow without any spatial gradient of turbulent kinetic energy (TKE), buoyancy flux is $b \leq 0.2\varepsilon$, where ε is the rate of dissipation of TKE, therefore turbulent mass diffusivity is given by :

$$K_{OS} \leq \frac{0.2\varepsilon}{N^2} \tag{6.2}$$

where N^2 is the buoyancy frequency. He mentioned an upper band for the rate of vertical eddy diffusivity. (Stillinger et al., 1983) and (Itsweire et al., 1993) used the Osborn method for stationary and shear and mesh generated turbulence in the laboratory. They found a good agreement between their results and the application of the Osborn method. In his method, Osborn assumed a constant mixing efficiency, while another study (Peters and Bokhorst, 2001) in the Hudson River showed that using a constant mixing efficiency could not be the right assumption as mixing efficiency is directly related to gradient Richardson number. Direct measurements in ocean, lake, and estuary environments (Etemad-Shahidi and Imberger, 2001; Etemad-Shahidi and Imberger, 2005; Saggio and Imberger, 2001; Yamazaki and Osborn, 1993) showed that this method cannot estimate the rate of vertical eddy diffusivity for up-gradient fluxes where water has undergone re-stratification.

The Osborn and Cox method (Osborn and Cox, 1972) is one of the indirect approaches used to estimate the rate of eddy diffusivity. Having a steady, laterally homogenous flow, production of temperature variance by velocity fluctuations is balanced with dissipation of temperature variance(Etemad-Shahidi and Imberger, 2005). Therefore vertical eddy diffusivity is given by:

$$K_{OC} = \frac{\chi / 2}{(\partial T / \partial x_3)} = 3kC_3 \tag{6.3}$$

where k is the molecular diffusivity of species and $C_3 = (\partial T' / \partial x_3)^2 / (\partial T / \partial x_3)^2$ is the vertical Cox number.

A correlation between the available potential energy (APEF) and the buoyancy frequency, molecular diffusivity, and the Cox number was found in the ocean in a study by (Dillon and Park, 1987). In fact, APEF is a measure of the maximum potential energy that can be released after turbulent events(Etemad-Shahidi and Imberger, 2005). They proposed their vertical eddy diffusivity as:

$$K_{DP} = (APEF) / N \tag{6.4}$$

Using the laboratory experiments and scaling arguments of (Ivey and Imberger, 1991), an alternative indirect method was proposed by (Barry et al., 2001). Using the value of $\frac{\varepsilon}{\upsilon N^2}$ as an indicator of a different regime in salt-stratified flow, they proposed:

$$K_{Bet} = 0.9\upsilon^{2/3}k^{1/3}\left(\frac{\varepsilon}{\upsilon N^2}\right) \qquad \text{if } \frac{\varepsilon}{\upsilon N^2} < 300 \tag{6.5}$$

$$K_{Bet} = 24\upsilon^{2/3}k^{1/3}\left(\frac{\varepsilon}{\upsilon N^2}\right)^{1/3} \qquad \text{if } \frac{\varepsilon}{\upsilon N^2} > 300 \tag{6.6}$$

where υ is molecular viscosity and k molecular diffusivity. They tried the Osborn method and found that it overestimates the vertical eddy diffusivity by a factor of two in a low energetic.

(Etemad-Shahidi and Imberger, 2005) examined the performance of the mentioned indirect method in the Swan River Estuary. They stated that all of the indirect methods overestimate the turbulent mass diffusion and amongst all methods, the Osborn equation yielded the poorest results. However, the method of Osborn and Cox presented the closest estimate to direct measurements. In another attempt (Etemad-Shahidi and Imberger, 2006) tried the accuracy of these approaches in Lake Kinneret. The results were consistent with what was observed in the Swan River.

Estimating vertical turbulent diffusion has a crucial importance in hydrodynamics and water quality modelling. The issue of nonlinear interactions between shear production of turbulence, dissipation of kinetic energy and buoyancy fluxes are commonly solved using various turbulence closure schemes in numerical models (Ivey et al., 2008). The rate of vertical mixing and advection of passive scalars can be attained by solving the equations governing the motion and flow properties. While the well-known Navier–Stokes equation is used for momentum conservation, the continuity equation guarantees conservation of mass. However, it is very difficult to solve the Navier-Stokes equation due to the nonlinear nature of this equation and

different other constraints (Elliott and Venayagamoorthy, 2011; Ferziger and Peric, 2002; Tennekes and Lumley, 1972). Reynolds decomposition is a practical approach to solving this problem. Using decomposition, variables are decomposed to their mean and fluctuating parts. This procedure is called Reynolds-Averaged Navier-Stokes (RANS). However, the decomposition leads to six extra terms in the momentum equation named Reynolds stresses and one additional term in the equation of transport of the scalar called the turbulent scalar flux. These additional terms in turbulent flow are named commonly as closure (Elliott and Venayagamoorthy, 2011). To close these sets of equations, some additional equations are essential, as for an unknown variable, one equation is necessary.

However, there is no consensus about the selection of variables/parameters for closing the sets of equations. While (Mellor and Yamada, 1982) proposed a combination of turbulent kinetic energy k and the turbulence length scale l (Rodi, 1987) presented a closure scheme based on k and the rate of dissipation, ε. A detailed description of different closures can be found in many publications such as (Umlauf and Burchard, 2003), (Price et al., 1986), (Large and Gent, 1999), (Wijesekera et al., 2003) , and (Simanjuntak et al., 2011). Some key considerations in the choice of a closure scheme include how it performs in regions with strong stratification, variable wind field and variable bathymetry (Durski et al., 2004) .

(d'Alessio et al., 1998) tested a new second-order closure scheme, similar to a Mellor-Yamada level 2.5 in terms of difficulty. They proposed their scheme for the oceanic surface layer. The basis of their model was to use turbulent kinetic energy as an independent variable. So, other turbulent properties were functions of TKE. Their assumption was that the momentum flux is down-gradient. The performance of the model was examined against different forcing conditions such as natural convection, heating or a windy surface. Comparison of simulated results and observed data at NOAA Ocean Weather stations in the Pacific Ocean agreed well.

In another attempt by (Zaron and Moum, 2009), an alternative set of parameterizations for vertical mixing, consisting of large-scale kinetic energy, shear, and Richardson number was proposed. The proposed closure scheme was tested using field measurements in the equatorial Pacific. The results showed good agreement between measured and simulated results. (Forryan et al., 2013) proposed a new closure scheme for turbulent eddy diffusivity. Direct observations of vertical turbulent diffusivity from three separate ocean regions in the North Atlantic and

Southern Ocean was used to examine the performance of the proposed closure scheme. They found a good agreement between the new closure scheme and measured data.

(Simanjuntak et al., 2011) used microstructure profiles of temperature and velocity to study turbulent vertical mixing in benthic and interfacial regions of a shallow, tidal estuary. The study was conducted throughout a period of maximum freshwater discharge via a barrage and under large shear. They used the concept of percentage down-gradient flux to propose a new closure scheme based on gradient Richardson number Ri_g as an alternative to a general mixing routine in an explicit mixing model for the three-dimensional estuary, lake and coastal ocean model (ELCOM) (Dallimore et al., 2003; Hodges and Dallimore, 2006; Hodges, 2000; Hodges and Imberger, 2001; Hodges et al., 2000; Laval et al., 2003).

(Yeates et al., 2013) used microstructure data collected in a thermally stratified lake to study the relationship between microstructure patches and Ri_g. They found three distinct ranges of gradient Richardson number: a range where inertia was dominant in the surface layer of the lake, an intermediate band where turbulence was generated primarily by shear instabilities and a super-critical Ri_g where turbulence was dominated by a strong buoyancy force.

Some of the closures are based on the relation between gradient Richardson number and Schmidt number (turbulent Prandtl number Pr_t). This number can be used as a scale of turbulent mixing. The Schmidt number is given by:

$$\mathrm{Pr}_t = \upsilon_t / K_\rho \qquad (6.7)$$

where υ_t is turbulent viscosity.

(Elliott and Venayagamoorthy, 2011) examined four different turbulent models in stable stratified flow in which the Schmidt number was a function of the gradient Richardson number. They examined the sensitivity of mixing routines to stratification. In other words, which models presented the larger mixing and which suppressed the turbulent fluxes due to stratification. However, due to the different basis of the models, the results showed variability. The results were used to emphasize the importance of choosing accurate parameterizations of Pr_t to present an acceptable turbulent mixing routine.

In this chapter the microstructure data collected with the PFP in the Swan River Estuary during three field trips (Chapter 4) and microstructure data measured in Lake Kinneret in 2001 (Saggio and Imberger, 2001; Yeates et al., 2013) was used to study vertical turbulent mixing in natural waters. The data from Lake Kinneret have just been used for vertical mixing. Detailed descriptions of other turbulent properties of the lake can be found in (Etemad-Shahidi and Imberger, 2001; Etemad-Shahidi and Imberger, 2006; Gómez-Giraldo et al., 2008b; Marti and Imberger, 2006; Saggio and Imberger, 2001; Yeates and Imberger, 2003; Yeates, 2007; Yeates et al., 2013; Yeates et al., 2008).

Different studies have been conducted to study turbulent vertical mixing in natural waters. However, the majority of studies considered active turbulence where $Ri_g < 0.25$ (Saggio and Imberger, 2001). In this chapter, both active and decaying turbulence $Ri_g > 0.25$ were used for turbulent mixing. Moreover, the variability of Pr_t as a function of Ri_g is investigated. Different studies in atmospheric boundary layers examined a closure scheme based on the Schmidt number (Canuto, 2002; Esau and Grachev, 2007; Pardyjak et al., 2002; Zilitinkevich et al., 2007; Zilitinkevich et al., 2013; Zilitinkevich et al., 2010). However, there are fewer research studies in natural waters focusing on Pr_t. These studies were limited to lab experiments in certain ranges of Schmidt number (Ivey and Imberger, 1991; Rohr et al., 1988).

This study is distinguished from previous studies due to two important characteristics. Firstly, here data from direct field measurements with very high resolution (1 mm) in vertical space is used, while preceding studies were confined to some numerical simulations (Elliott and Venayagamoorthy, 2011) or lab experiments (Ivey and Imberger, 1991). Even in atmospheric measurements of boundary layers there were some uncertainties (Esau and Grachev, 2007). However, the velocity measurement that is central to the estimation of direct turbulent fluxes (Chapter 4) was validated by the inverse method as an alternative approach (Chapter 5). Secondly, the changes of Pr_t as a function of Ri_g are investigated in four distinct zones. These regions are $(+K_\rho + \upsilon_t)$, $(+K_\rho, -\upsilon_t)$, $(-K_\rho, +\upsilon_t)$, and $(-K_\rho, -\upsilon_t)$ that previously have not been published in the literature.

The aim of this chapter is not only the study of variability of eddy diffusivity and eddy viscosity as a function of gradient Richardson number, but also the study of the Schmidt number as a function gradient Richardson number. To do so, firstly the

results of this study are presented. Secondly, the important outcomes are discussed. Finally, a summary of the chapter is presented.

6.2 Results

6.2.1 Eddy diffusivity and eddy viscosity

The microstructure data collected in the Swan River and Lake Kinneret was used to study vertical mixing. To do so, the variability of eddy diffusivity and eddy viscosity as a function of gradient Richardson number was studied. The normalised eddy diffusivity of mass and turbulent viscosity was plotted against Ri_g (Figure 6.1). Eddy diffusivity of mass was normalised by molecular mass diffusion and turbulent viscosity was normalised by kinematic viscosity. Each point means one stationary temperature gradient segment. The depths of segments were shown by different colours. The data from the estuary and the lake showed a similar structure: a weak negative relationship between normalised eddy diffusivity and small gradient Richardson number, a gradual increase in the slope of the relationship for the intermediate range of Ri_g and a dramatic fall for gradient Richardson numbers larger than 0.25. Therefore, three distinct ranges of gradient Richardson number were proposed. While Ri_g <0.01 made the first region, the second zone included 0.01< Ri_g < 0.25. The third part consisted of Ri_g > 0.25.

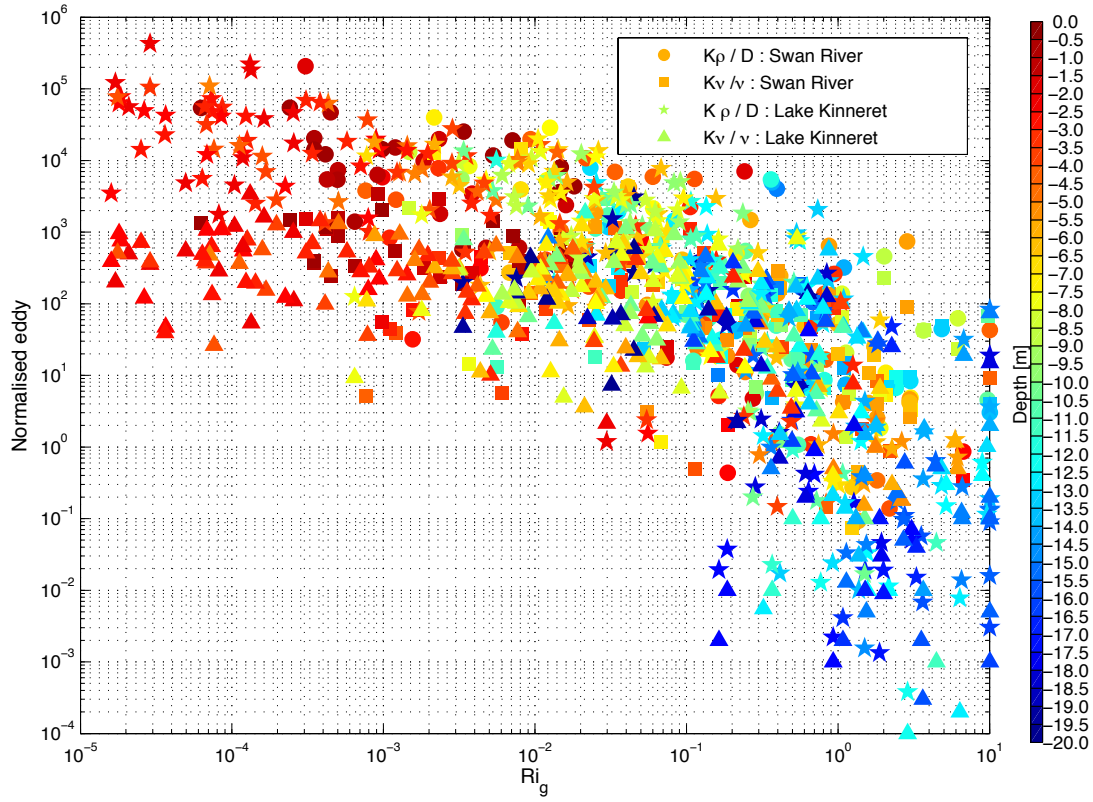

Figure 6.1 Eddy diffusivity of mass and turbulent viscosity as a function of gradient Richardson number.

6.2.1.1 Lower range Richardson number ($Ri_g < 0.01$)

The majority of segments in the lower range of gradient Richardson numbers were in the surface area of both sites. More than 82 per cent of segments in the Swan River Estuary had a depth of less than 5 m, where there was usually a weak to moderate stratification with a median value of buoyancy frequency of about 4×10^{-5} s^{-2}. Studies in Lake Kinneret by (Etemad-Shahidi and Imberger, 2001; Saggio and Imberger, 2001; Yeates et al., 2013) showed weak stratification in the surface layer with a buoyancy frequency of about 10^{-5} s^{-2}. The average value of the Ozmidov scale was significantly larger than the Thorpe scale within this area. The mean values of L_o and L_T were 1.39 and 0.43 m, which is consistent with (Dillon, 1982), where he reported

a significant difference between these two length scales in the mixing layer.

Eddy diffusivity of mass and turbulent viscosity showed a similar trend to Ri_g. Both mass diffusion and eddy viscosity slightly decreased with increased Ri_g. Eddy diffusivity of mass varied between 10^{-2} and 10^{-4} m^2s^{-1}. Turbulent viscosity changed between 10^{-3} and 10^{-5} m^2s^{-1} (Figure 6.1).

6.2.1.2 Intermediate range of Richardson number ($0.01 < Ri_g < 0.25$)

In this range, the major portion of the segments had an intermediate depth. However 2 per cent of the segments in the estuary with lower Ri_g had depths of more than 10 m. While the shear decreased with increased Ri_g, buoyancy frequency increased. Median values for shear and buoyancy frequency in the estuary were 0.09 s^{-1} and 7×10^{-4} s^{-2}. The Thorpe and Ozmidov scales dramatically decreased with increased Ri_g, $R_{OT} = L_O / L_T = 0.9$, which is consistent with (Dillon, 1982). However, the Kolmogorov length scale increased with growth in Ri_g compared to the previous range.

In the intermediate ranges of Richardson number, the normalized eddy diffusivity decreased slightly more than in the previous part as Ri_g increased. Diffusion coefficient of mass varied between 10^{-4} and 10^{-6} m^2s^{-1}. As for the previous range, eddy viscosity showed the same structure, but with smaller values than eddy diffusivity of mass. (Stevens et al., 2011) observed bin-averaged values of about 10^{-3} m^2s^{-1} for eddy diffusivity of the scalar in the pycnocline of the ocean.

6.2.1.3 Supercritical range of gradient Richardson number ($Ri_g > 0.25$)

Almost the majority of segments with a large depth were in this range, where shear

was small and stratification was strong. The eddy values dramatically dropped as the gradient Richardson number approached a larger value than $Ri_g = 0.25$. In almost all of the segments the molecular diffusion coefficient dominated turbulent diffusivity. The turbulent viscosity was less than eddy diffusivity of mass for $0.25 < Ri_g < 1$, however, some segments with $Ri_g > 1$ showed larger turbulent viscosity than eddy diffusivity of mass. A low value of dissipation was the consequence of having low energy levels, insufficient to sustain a considerable turbulent segment. Therefore, buoyancy and viscosity dominated the majority of segments in this zone.

6.2.2 Schmidt number

In this section the variability of the Schmidt number versus gradient Richardson number in four different regions is presented. Not only Pr_t of each temperature gradient stationary segment is presented, but also the binned values are given. The data was arranged into one-tenth log bins of Ri_g throughout all ranges of gradient Richardson number. There were at least 10 values within each bin. If the numbers of samples within each bin were less than 10, the bin was merged with its adjacent bin (ascending). Then a curve was fitted to binned values using the least square error.

6.2.2.1 Down-gradient buoyancy and momentum fluxes

Figure 6.2 shows Pr_t within the region of positive eddy diffusivity (down-gradient buoyancy fluxes) of mass and positive turbulent viscosity (down-gradient momentum fluxes). While individual values showed a wide scatter in $10^{-5} < Ri_g < 1$, the spread decreased for gradient Richardson numbers larger than 1. The bin-averaged value dramatically showed minor scatter. Considering best fit, in the area with $10^{-5} < Ri_g < 1$

binned values showed a good agreement with the proposed curve. For $Ri_g > 1$ the binned values showed a larger scatter to best fit. The maximum difference between the curve and grouped values occurred at the bin with the largest gradient Richardson number (Ri_g=5.5). In the weak stability regime $Ri_g < 0.01$, the binned value showed an asymptotic value of about Pr_t=0.6. However, in the strong stability regime ($Ri_g >$ 0.25), the Schmidt number increased with the gradient Richardson number increase.

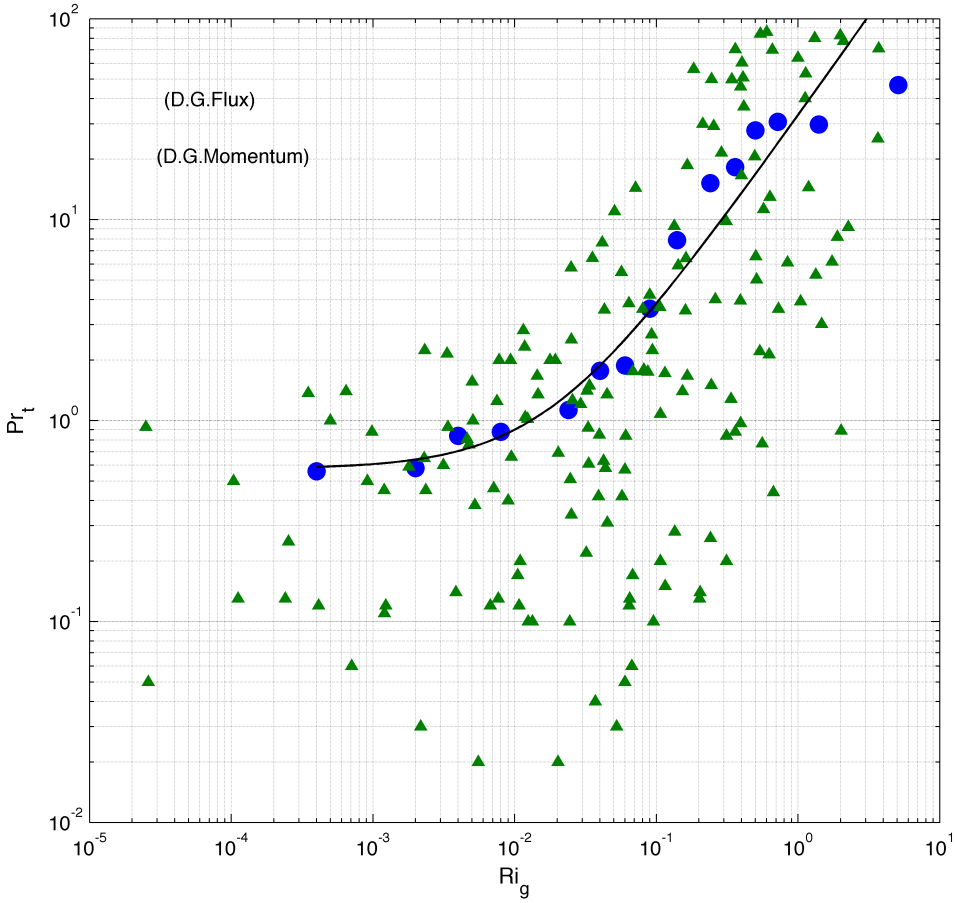

Figure 6.2 Schmidt number in the region with positive mass diffusion and turbulent viscosity. Triangles show individual segments and dots represent bin-averaged values.

6.2.2.2 Down-gradient buoyancy and up-gradient momentum fluxes

Figure 6.3 presents the Schmidt number within a region of positive eddy diffusivity of mass and negative turbulent viscosity. Individual segments showed large scatter in $10^{-5}<Ri_g< 1$, then the scatter decreased for values $Ri_g > 10^{-1}$. Similarly to the previous region $(+K_\rho + \upsilon_t)$, scatter dramatically decreased using binned average values. However, in the regions with $Ri_g < 10^{-4}$ and $Ri_g >1$, difference to best fit increased. Between these two gradient Richardson numbers, bin-averaged values presented acceptable agreement with the curve. Similarly to the part with down-gradient flux and down-gradient momentum, the asymptotic line was observed in the weak stratification regime ($Ri_g < 0.01$). The asymptotic value was about $-Pr_t=0.4$.

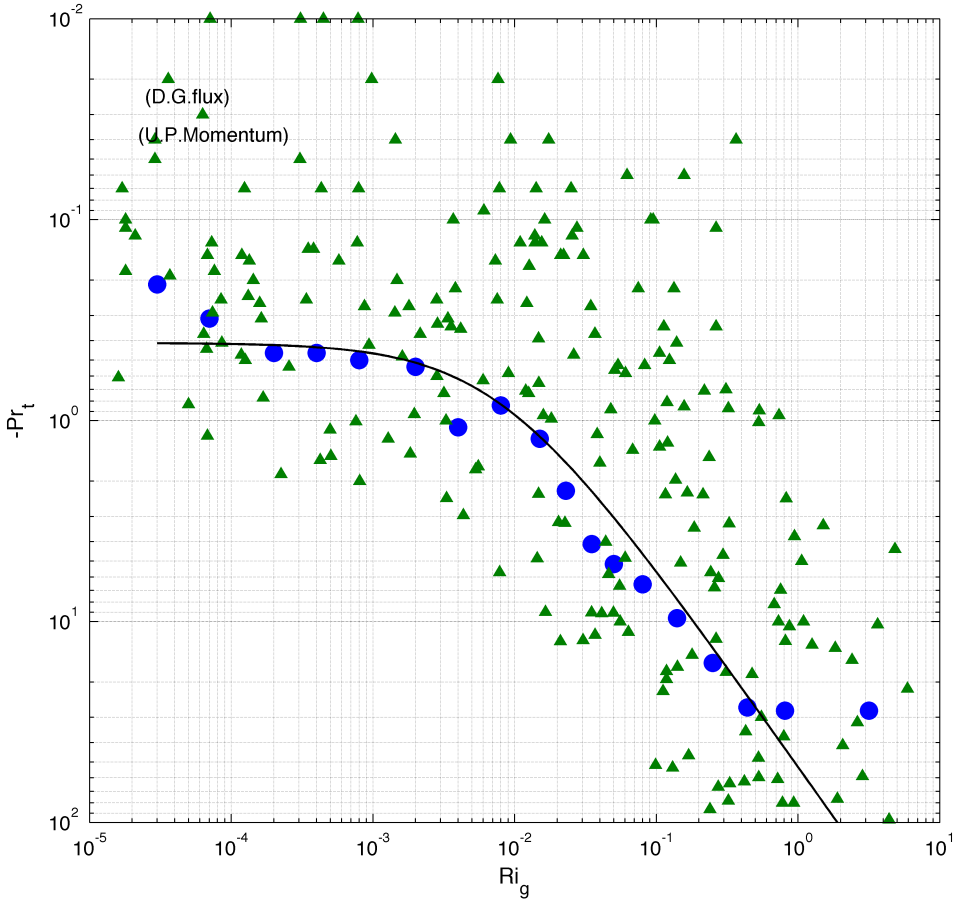

Figure 6.3 Schmidt number for the region with down-gradient buoyancy fluxes and up-gradient momentum fluxes. Triangles show individual segments and dots represent bin-averaged values.

6.2.2.3 Up-gradient buoyancy and up-gradient momentum fluxes

Schmidt numbers for the condition for negative eddy diffusivity of mass and eddy viscosity are presented in Figure 6.4. Individual segments showed scatter in both strong stable conditions ($Ri_g > 0.25$) and weak stability regimes ($Ri_g < 0.01$). The difference between grouped values and the curve of best fit was considerable. Bin-averaged values presented scatter through all ranges of gradient Richardson number. While the curve of best fit increased with increased Ri_g, small gradient Richardson number present an asymptotic curve. The asymptotic Schmidt number was 0.7.

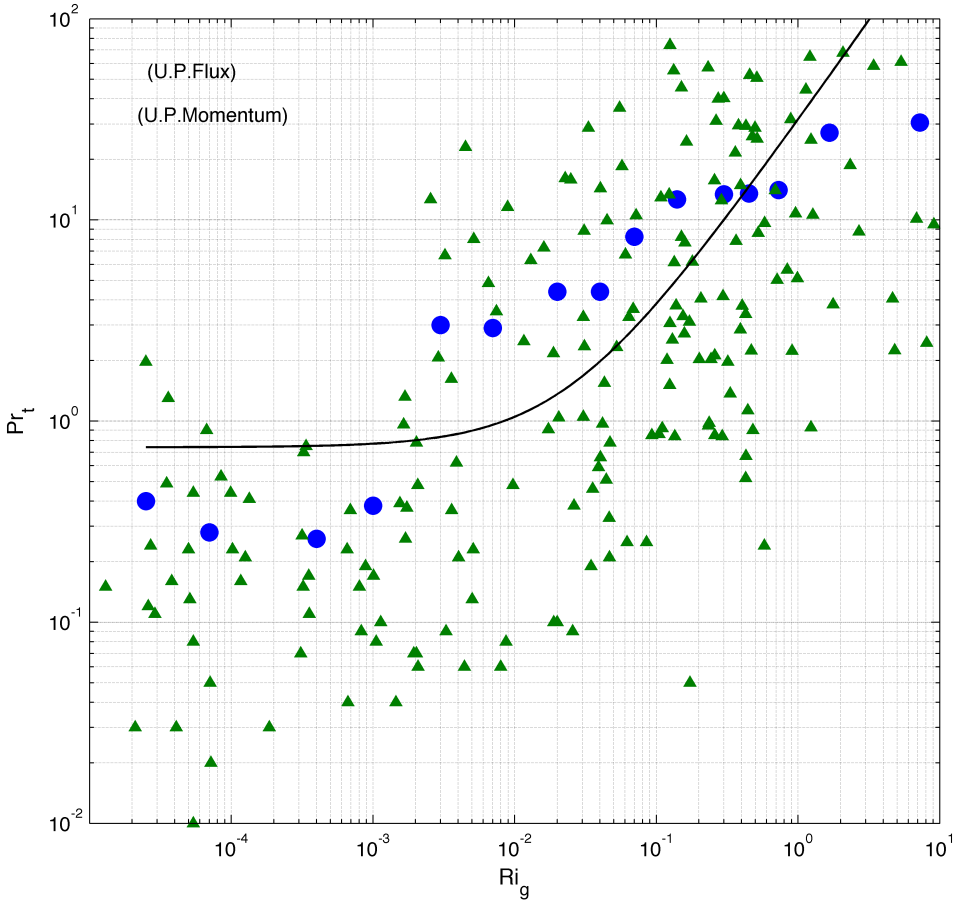

Figure 6.4 Schmidt number in the region with up-gradient buoyancy fluxes and up-gradient momentum fluxes. Triangles show individual segments and dots represent bin-averaged values.

6.2.2.4 Up-gradient buoyancy and down-gradient momentum fluxes

Schmidt numbers with up-gradient buoyancy fluxes and down-gradient momentum fluxes are presented in Figure 6.5. Here again, individual temperature gradient stationary segments showed large scatter. However, with increased Ri_g the scatter slightly decreased. The bin-averaged groups presented scatter through all ranges of gradient Richardson number. The Schmidt number for bin-averaged values of $Ri_g < 10^{-3}$ and $Ri_g > 1$ showed a large difference to the best fit curve. Like previous regions, the fitted curve showed an asymptotic line of about Pr_t=0.8.

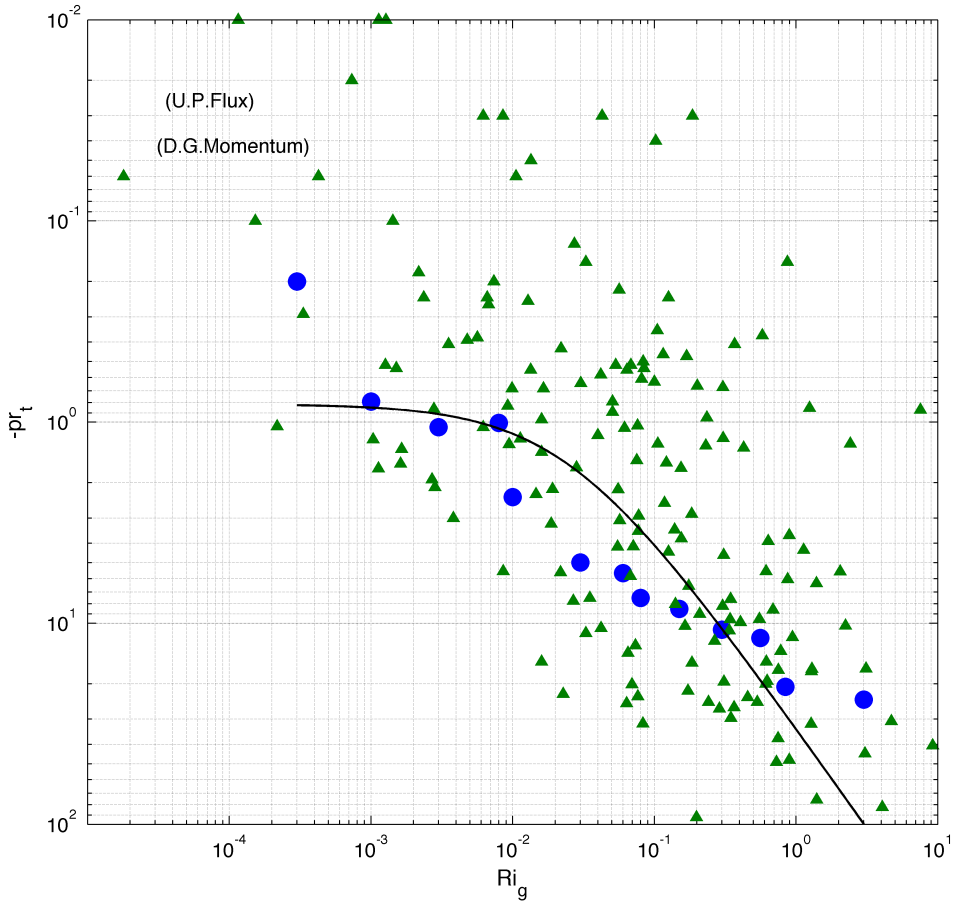

Figure 6.5 Schmidt number for up-gradient buoyancy fluxes and down-gradient momentum fluxes. Triangles show individual segments and dots represent bin-averaged values.

6.3 Discussion

The structure of eddy diffusivity of mass as a function of Ri_g is similar to what (Yeates et al., 2013) found in Lake Kinneret, using microstructure data collected with the PFP. However they didn't examine the variability of turbulent viscosity due to changes in gradient Richardson number. The turbulent viscosity from both estuary and lake showed that eddy viscosity presented a similar structure to eddy diffusivity of mass (three distinct zones of Ri_g).

Microstructure data collected in the Swan River Estuary showed that in the first region, where there existed a weak stratification, the presence of significant shear with a median value of about 0.35 s^{-1} and its action on weak stratification caused gradient Richardson numbers much less than 0.25 (Ri_g <0.01) in the Swan River's surface layer. The same structure of Ri_g was found in Lake Kinneret. However, in Lake Kinneret some values of gradient Richardson numbers even smaller than those for the Swan River were observed. It might be caused by the effect of wind at the surface layer, while the Swan River studies were carried out on calm days in a sheltered area.

The magnitude of turbulent viscosity in almost the entire range of Ri_g <0.01 was different from eddy diffusivity of mass. Turbulent viscosity was almost one or two decade less than mass diffusion. Eddy diffusivity of mass varied in the range of 10^{-4} -10^{-2} m^2s^{-1} within the segments with Ri_g <0.01, in the lake and estuary. (Stevens et al., 2011) reported eddy diffusivity of mass as great as 10^{-2} m^2s^{-1} in the oceanic surface layer. (Peters, 1997) found the same value for the bottom layer during flood conditions in the Hudson River off Manhattan.

(Yeates et al., 2013) proposed a formulation for eddy diffusivity of mass based on the microstructure data collected in Lake Kinneret. They proposed that eddy

diffusivity of mass in the region with $Ri_g < 0.03$ is given by $K_\rho / D = 242 Ri_g^{-0.5}$.

Using the proposed closure for the Swan River Estuary with an estimate of a median value of Ri_g=0.02 in the weakly stratified layers, then $K_\rho = 7.5 \times 10^{-4}$, which is consistent with observations ($K_\rho = 6 \times 10^{-4}$).

As previously mentioned, 2 per cent of the segments had depths more than 10 m in the region with $0.01 < Ri_g < 0.25$. The presence of deep segments is attributed to the effects of the benthic boundary layer (BBL), where shear acts on the bottom and friction causes mixing of the bottom boundary layer.

In the intermediate range of gradient Richardson numbers, length scales were smaller than those in $Ri_g < 0.01$, implying the suppression of overturns by buoyancy and viscosity.

The variability of mass diffusion in the intermediate range of gradient Richardson number could be explained by two different mechanisms in which turbulence is sustained: (1) due to internal wave motions (Gargett and Holloway, 1984; Saggio and Imberger, 2001; Yeates, 2007; Yeates et al., 2013), and (2) more energetic due to shear driven turbulence (Gómez-Giraldo et al., 2008b; Imberger and Ivey, 1991; Saggio and Imberger, 2001). The first class generates a turbulent small scale suppressed quickly with viscosity and the second group presents a highly dissipative turbulent small scale.

(Yeates et al., 2013) proposed a model for eddy diffusivity of mass when for their intermediate range, based on microstructure data collected in Lake Kinneret. According to their closure, mass diffusion is given by $K_\rho / D = 0.81 Ri_g^{-2.12}$. Using the median value of Ri_g=0.09 (for this study intermediate range) for data collected in the Swan River Estuary $K_\rho = 1.33 \times 10^{-5}$ was located in the observation ranges

($K_\rho = 1.2\times10^{-5}$).

Turbulent viscosity presented larger values than eddy diffusivity of mass for $Ri_g > 0.25$. Usually in this range one may expect that turbulence must completely be suppressed and molecular diffusivity and kinematic viscosity should dominate. However, Figure 6.1 showed both turbulent viscosity and eddy diffusivity survived even for $Ri_g > 0.25$. Eddy diffusivity of mass decreased more rapidly than turbulent viscosity, which is consistent with previous studies (Galperin et al., 2007; Itsweire and Helland, 1989; Mahrt and Vickers, 2006; Mauritsen and Svensson, 2007; Strang and Fernando, 2001; Webster, 1964). (Galperin et al., 2007; Meunier et al., 2006; Spedding, 1997; Spedding, 2001) highlighted the influence of flow anisotropization and internal wave contamination in large gradient Richardson numbers. Internal wave action is the case for Lake Kinneret as in a study by (Gómez-Giraldo et al., 2008a) they reported four different types of internal waves that could be found in the lake. However, in the estuary anisotropy resulted from shear instability caused by a higher velocity in the surface layers.

While previously up-gradient fluxes were neglected (Yeates et al., 2013), Pr_t highlighted the importance of considering all up-gradient and down-gradient buoyancy fluxes in turbulence studies. It should be emphasized that not only the possibility of the presence of segments with up-gradient fluxes might be equal to segments with down-gradient fluxes (Etemad-Shahidi and Imberger, 2001), but also the existence of turbulent viscosity and eddy diffusivity within a segment with a different sign is considerable. In other words, according to Figures 6.2 to 6.5, one can consider four different possibilities for generating Pr_t [$(+K_\rho + \upsilon_t)$, $(+K_\rho, -\upsilon_t)$, $(-K_\rho, +\upsilon_t)$, and $(-K_\rho, -\upsilon_t)$]. The numbers of segments in each quadratic zone reveal that each zone has a considerable population that cannot be neglected.

Scatters were found in all quadratic zones revealed; however, the minimum difference from the best fit curve was observed where both turbulent viscosity and eddy diffusivity were positive (down-gradient buoyancy and momentum fluxes).

Pr_t increased with increasing Ri_g. In the regime with the higher gradient Richardson number ($Ri_g > 0.25$) when both fluxes have a similar sign, eddy diffusivity of mass decreased faster than turbulent viscosity, so the consequence is increasing Pr_t. This finding is consistent with previous findings (Esau and Grachev, 2007; Keller and Van Atta, 2000; Schumann and Gerz, 1995; Yagüe et al., 2006). However, in weakly stratified water columns Pr_t showed an asymptotic structure that varied in the range 0.4 - 0.8, which is consistent with direct measurements of the atmospheric boundary layer (Esau and Grachev, 2007). The presence of the asymptote is associated with the weakness of the instrument's capability to measure the weak stratification.

6.4 Summary

Validated microstructure velocity with the inverse method and temperature and conductivity microstructure profiles collected with the PFP in the Swan River Estuary were used to study turbulent vertical mixing. Some additional data sets collected in Lake Kinneret in 2001 were employed to enhance the available data sets. While data from the Swan River Estuary was measured in a sheltered area with negligible effects from the wind, the lake data comprised different forcing mechanisms such as wind, heating and cooling convection, internal waves and shear instability.

Using the gradient Richardson number as an independent variable and eddy viscosity and mass diffusivity as dependent parameters, vertical mixing was classified into three regimes. There was a small value of gradient Richardson number ($Ri_g < 0.01$)

where vertical transport was enhanced by boundary shear-driven turbulence. In this regime, eddy diffusivity of mass and turbulent viscosity decreased slightly with increasing Ri_g. The mass diffusion coefficient was larger than turbulent viscosity. The intermediate range of gradient Richardson number ($0.01< Ri_g <0.25$) corresponded to the diapycnal part of the water columns. However, some segments of the benthic boundary layer were located in the intermediate range. Eddy diffusivity of mass and turbulent viscosity decreased more than in the previous range. The super-critical range of the gradient Richardson number ($Ri_g > 0.25$) was where turbulence dramatically dropped. In this range, in some segments, turbulent viscosity had larger values than eddy diffusivity. This phenomenon is associated with horizontal anisotropy and the effects of internal waves.

The variability of the Schmidt number as a function of Ri_g was studied in four different zones where there were: (1) down-gradient buoyancy and momentum fluxes, (2) down-gradient buoyancy fluxes and up-gradient momentum fluxes, (3) up-gradient buoyancy and momentum fluxes, (4) up-gradient buoyancy fluxes and down-gradient momentum fluxes. The considerable population within each zone implied that neglecting the up-gradient segments leads to loosing valuable data sets. While Pr_t increased with increasing Ri_g, the Schmidt number showed an asymptote in weak stratification, caused by the limitations of the instrument in measuring the weak stratification.

7
Conclusion and recommendations

To protect water bodies from environmental deterioration a good understanding of the physics and ecology of water environments is essential. Field measurements and numerical modelling are two popular means for studying natural waters. In fact, field measurements provide all the necessary input data for numerical simulation. Moreover, to use a numerical model for sustainable management it must be validated. Therefore, the presence of some validation data for a numerical simulation is necessary too.

Usually, water bodies undergo stratification during a particular period of the year. Stratification amplifies the quality issues in natural waters. In stratified water columns, vertical mixing is smaller than horizontal dispersion. In fact, stratification acts as a barrier for vertical mixing. Vertical mixing is central to hydrodynamic and water quality studies, as it erodes the stratification and supplies nutrients from bottom layers to surface layers and transfers dissolved oxygen in the opposite direction in stratified water columns. In numerical models, vertical mixing is modelled using some closure schemes. In fact, in closure schemes vertical mixing is a function of some measurable parameters. The accuracy of a numerical model has a direct relationship to the accuracy of the vertical mixing scheme. So, direct measurements of microstructure profiles can be used to run and validate numerical models or examine an available closure scheme or propose a new vertical mixing model.

Although many direct measurements have been conducted to collect some microstructure data for turbulence studies, they have had some limitation in scope or time. They were confined to some constant depth or particular duration. Moreover, the profiles of direct measurements such as velocity have not been compared with other alternatives; also the rate of dissipation of turbulent kinetic energy has been estimated with one or a maximum of two methods. Many of the studies have focused just on active turbulence and neglected decaying turbulence.

Data collected from three direct (field) measurements in the lower part of the Swan River Estuary in Western Australia were arranged to provide a data set of estuarine processes that can serve for validation of closure schemes at the process level. The data sets provide all the necessary data (initial condition, validation condition and supplementary data) for numerical simulation.

Further, the data was used to gain a better understanding of vertical mixing in a stratified shear flow. Data was collected using a multi-scale probe developed by the Centre for Water Research (CWR), at the University of Western Australia (UWA). The multi-scale probe is a free-falling profiler and incorporated three different instruments: an instrument measuring turbulent microstructure at 100 Hz; instruments measuring fine-scale gradients in temperature, conductivity, velocity, pH and dissolved oxygen (50 Hz); and multi-wavelength fluorometers measuring fluorescence of photosynthetic pigments and dissolved organic carbon that samples at 1 Hz. The nominal drop rate of the PFP is about 0.1 ms^{-1}, which gives a vertical resolution of about 1 mm for turbulent microstructure.

The study domain was in the lower part of the Swan River Estuary, a micro-tidal estuary that is located in the southwest corner of Australia ($31^{\circ}41^{'}$ S and $116^{\circ}04^{'}$ E). The accumulated distance from the lower boundary at Fremantle to the upper border was about14.1 km Therefore, for all studies, Fremantle was chosen as the reference point. Three field studies were carried out on 27 August, 8 October, and 2 November 2012 in the domain, profiling water columns from the surface to the bottom. While the first field trip was conducted during spring tides, the second measurement was performed in neap tides. The profiling stations on different field trips were in different places within the domain. Measuring three components of flow velocity with a resolution of about 0.001 ms^{-1}, the PFP is capable of direct estimation of turbulent fluxes. Measured relative velocity (relative to the instrument) was low-pass filtered at 0.4 Hz. Then the horizontal velocities were decomposed to North-South (N-S) and East-West (E-W). By integrating the drag forces on the probe, as in the method suggested by Hendricks and Rodensbuch (Hendricks and Rodenbusch, 1981; Saggio and Imberger, 2001)) and Saggio and Imberger(Saggio and Imberger, 2001), flow velocity was estimated. The temperature and conductivity signals were digitally sharpened and smoothed using the method described by (Fozdar et al., 1985) before being used to derive density and salinity.

Due to the non-stationary nature of turbulence, analysis was conducted within stationary temperature gradient segments. The results of some turbulent properties were as some samples presented in Figure 2.5.

Three different approaches for estimating the rate of dissipation of turbulent kinetic energy are compared in the study. The rate of dissipation of turbulent energy is one of the most important parameters from which eddy diffusivity can indirectly be estimated. The first method was the Batchelor method, in which dissipation was estimated from temperature gradient microstructure. A theoretical Batchelor spectrum was fitted to the measured temperature gradient spectrum. To achieve the best fit between the theoretical and measured spectrum, the least square error method was used. The second method was the inertial subrange. In this method the rate of energy dissipation was calculated and can be estimated by fitting the Kolmogorov -5/3 slope to the velocity spectrum in a log-log domain. To use this method, at least one component of velocity must be available. Similarly to the Batchelor method, a theoretical spectrum was fitted to the measured velocity spectrum. The third method was shear microstructure dissipation (shear dissipation). In this method, dissipation was estimated from velocity strain. The results from the three methods showed almost identical results. The Batchelor method needs an extra visual investigation to discard inappropriate fit. Therefore, using this method might lead losing some segments. The inertial subrange method is time consuming and inconvenient, especially when the measured spectrum does not show a clear subrange. However, shear dissipation is more efficient and more convenient than other methods.

The results of the three field studies conducted in the lower part of the Swan River Estuary (the domain) are presented in Chapter 4. During the first field trip, the wind conditions were calm. The salinity contours showed that the domain was strongly stratified in the upper part of the domain and had weak stratification at the river mouth. However, temperature observations presented very weak thermal stratification. Dissolved oxygen concentration was larger in the surface; however, the concentration of dissolved oxygen in the upper part was larger than at the river mouth. The maximum of longitudinal velocity, shear, and shear dissipation was larger at the surface. During the second field trip, calm wind conditions were observed in the domain. Measurements were conducted throughout the second half of ebb tides. The mean variables (salinity, temperature, dissolved oxygen, turbidity and pH), and turbulent properties were measured at 10 profiling stations with an

averaged horizontal distance of about 200 m apart in five consecutive transects. The results from the second and fifth transects were compared. As the time elapsed to slack tide, longitudinal velocity decreased. The larger dissipation, shear and buoyancy flux was observed at the surface layer. During the third field experiment, wind data showed in increase compared to two previous field studies. The salinity curtain showed strong stratification within the entire domain. Thermal stratification was observed in the domain too. The dissolved oxygen concentration decreased in the domain compared to the two previous field experiments. Data collected from all three field experiments showed that fresh water discharges from the upper Swan River had an important role in building stratification within the domain. This effect amplified even more when water propagated to the upper part of the river moved back to the ocean. A comparison between the first and last field experiments revealed that there was a thermal stratification in the domain due to seasonal changes. The maximum velocity occurred in the time between high and low tide, before slack time. During ebb tide the major driving force was barotropic flow; however, at the bottom of the river mouth baroclinic flow rebounded on the barotropic flow. Reynolds stresses and shear dissipation showed a direct relation to shear values.

In Chapter 5, a time-dependent inverse method was used to estimate field velocity. The direct effects of velocity on turbulent fluxes caused special attention to be paid to velocity measurements. Although the velocity was measured with the PFP, the idea was to compare measured velocity with another alternative. The basis of the inverse method is a two-dimensional advection-diffusion equation. The equation of the advection-diffusion was discretized using forward differencing in time and central differencing in space (FTCS). The collected data during five consecutive transects on 8 October 2012 was used to run the inverse method. Salinity, temperature, dissolved oxygen, turbidity and pH were used as tracers. The inverse method was applied for the first and second transects. Combinations of all tracers achieved the optimum results. The inverse method was applied for the fourth and fifth transects. After examining different combination of tracers, the best combination was selected, which consisted of salinity, turbidity and pH. As water temperature increases due to air temperature and solar radiation, those are external factors that must be considered in addition to the hydrodynamics of the estuary. Therefore, water temperature may lead to an error in the result. The same issue happened for dissolved oxygen, where its concentration was increased by biological

activities. Therefore, it is very important to use some tracers that keep their characteristics in any reaction between transects, but show some appreciable spatial changes due to the hydrodynamics of the water body. Comparison between the inverse velocity field and the measured velocity field showed a good agreement regarding flow direction. Both methods showed flow direction to the ocean. However, in terms of magnitude, a difference was observed as the inverse method showed an averaged velocity during the time interval between two transects but the PFP presented instantaneous velocity.

Chapter 6 shows turbulent vertical mixing based on the microstructure data collected in the Swan River Estuary during three field measurements. As the domain was in a sheltered area and sampling was conducted during daytime, the main forcing driver was shear. To make the available data set comprehensive comprising other driving forces, microstructure profiles collected in Lake Kinneret in 2001 were added to the data sets. Lake data included some different driving forces such as wind energy at the surface, natural convection during the cooling time, internal wave motions and shear instability. This chapter aimed to achieve two important objectives. Firstly, the variability of eddy diffusivity and eddy viscosity as a function of gradient Richardson number was studied. Secondly, the variability of the turbulent Prandtl number as a function of gradient Richardson numbers in four different zones was investigated. Quadratic zones consisted of down-gradient buoyancy and momentum fluxes, down-gradient buoyancy and up-gradient momentum fluxes, up-gradient buoyancy and momentum fluxes and the up-gradient buoyancy and down-gradient momentum fluxes. Eddy diffusivity of mass and turbulent viscosity shared similar trends in the three different ranges of gradient Richardson number. The first region was the weak stratification regime $(Ri_g < 0.01)$, where eddy diffusivity and eddy viscosity varied slowly with increasing Ri_g. In this region, turbulent viscosity was less than mass diffusivity. The majority of segments in this area belonged to the surface layer. The second range was an intermediate band of gradient Richardson number $(0.01 < Ri_g < 0.25)$. In this range, eddy diffusivity of mass and turbulent viscosity showed more change with increasing Ri_g. The eddy diffusivity of mass was larger than eddy viscosity. The majority of the segments had medium depths; however, some segments from the benthic boundary were in this region. In the third

range, $Ri_g > 0.25$ and eddy diffusivity and eddy viscosity dropped dramatically due to the increasing gradient Richardson number. However in this regime, in some segments turbulent viscosity was larger than eddy diffusivity. This happened due to the effects of horizontal anisotropy and contamination due to the effect of internal waves. The quadratic zone of Pr_t (down-gradient buoyancy and momentum fluxes, down-gradient buoyancy and up-gradient momentum fluxes, up-gradient buoyancy and up-gradient momentum, and up-gradient momentum and down-gradient momentum fluxes) showed the importance of up-gradient segments due to the large population within these segments. It showed that neglecting the up-gradient segments was a wrong convention. Moreover, when both momentum and buoyancy fluxes were down–gradient, the bin-averaged values of the Schmidt number within one-tenth log bins of gradient Richardson number showed the minimum scatter on the best-fitted curve. For $Ri_g < 0.01$ the Schmidt number showed an asymptote. This was caused by the inability of the instrument to measure very weak stratification. However, for $Ri_g > 0.25$ when both momentum and buoyancy fluxes had the same sign, Pr_t increased with increasing Ri_g, which is consistent with findings of larger turbulent viscosity than eddy diffusivity for this range.

Recommendations for further study

A series of future studies are proposed to fill the gaps in this research field:

- The domain of the studies could be expanded to the upper Swan. Salinity contours showed strong density in the upper part of the domain. Moreover, dissolved oxygen contours showed that, in the passage of time from spring to summer, the concentration of dissolved oxygen decreased in the upper part of the domain. Therefore, it can be expected this stratification caused some quality issues in the upper Swan due to a weak vertical mixing effect (Hamilton et al., 2001).
- As previously mentioned, the domain of the study was located in a sheltered area. Although some data from the lake was used, the effects of wind were neglected on the Swan data. Therefore, it would be recommended to conduct

the field measurement where winds do have considerable effects on the water surface.

- As the field studies in the Swan River were conducted during daytime, it would be proposed to perform some field measurement during the night, to collect data relating to natural cooling convection.
- The time interval between the first and last field measurements in the Swan River Estuary was confined to 68 days. However, regular annual measurements may provide valuable information on the hydrodynamics and water quality of the estuary.
- The velocity field was estimated with a time-dependent inverse method. However, the inverse method could be used to estimate the rate of eddy diffusivity of mass.
- Temperature gradient stationary segments were determined using a threshold value of about 30. However, one might try to use a variable threshold to find the exact boundary of temperature gradient segments.
- Shear was estimated based on velocity profiles low-pass filtered at 0.4 Hz (a vertical length of about 0.25 m). It would be proposed to examine the variability of shear values for vertical length scales larger or smaller than this 0.25 m.
- The majority of literature reviewed showed the importance of down-gradient fluxes (active turbulence). It seems some research could be conducted to focus on up-gradient fluxes (re-stratification process).
- The results of this study could be used to propose a new closure scheme based on the variability of Pr_t as a function of Ri_g .

References

Agrawal, Y., 1984. A CCD chirp-Z FFT Doppler signal processor for laser velocimetry. Journal of Physics E: Scientific Instruments, 17(6): 458.

Anohin, V.V., Imberger, J., Romero, J.R. and Ivey, G.N., 2006. Effect of long internal waves on the quality of water withdrawn from a stratified reservoir. Journal of Hydraulic Engineering, 132(11): 1134-1145.

Anokhin, V.V., Imberger, J., Ivey, G.N. and Romero, J.R., 2008. Estimating net transport and mixing using a time-dependent inverse method. Journal of Geophysical Research, 113(C7).

Barry, M.E., Ivey, G.N., Winters, K.B. and Imberger, J., 2001. Measurements of diapycnal diffusivities in stratified fluids. Journal of Fluid Mechanics, 442(1): 267-291.

Batchelor, G., 1959. Small-scale variation of convected quantities like temperature in turbulent fluid. J. Fluid Mech, 5(1): 113-133.

Beutler, M., Wiltshire, K.H., Meyer, B., Moldaenke, C., Lüring, C., Meyerhöfer, M., Hansen, U.-P. and Dau, H., 2002. A fluorometric method for the differentiation of algal populations in vivo and in situ. Photosynthesis Research, 72(1): 39-53.

Bluteau, C.E., Jones, N.L. and Ivey, G.N., 2011. Estimating turbulent kinetic energy dissipation using the inertial subrange method in environmental flows. Limnology and Oceanography: Methods, 9: 302-321.

BOASHASH, B., 1986. Application-of the Wigner-Ville Distribution t6 Temperature Gradient Mikstructure:: i A New Tkchnique to-Study Small-Scale Variations. Journal of physical oceanography.

Boehrer, B. and Schultze, M., 2008. Stratification of lakes. Reviews of Geophysics, 46(2).

Brumley, B.H., Cabrera, R.G., Deines, K.L. and Terray, E.A., 1991. Performance of a broad-band acoustic Doppler current profiler. Oceanic Engineering, IEEE Journal of, 16(4): 402-407.

Burchard, H., Craig, P.D., Gemmrich, J.R., van Haren, H., Mathieu, P.-P., Meier, H.E.M., Smith, W.A.M.N., Prandke, H., Rippeth, T.P., Skyllingstad, E.D., Smyth, W.D., Welsh, D.J.S. and Wijesekera, H.W., 2008. Observational and numerical modeling methods for quantifying coastal ocean turbulence and mixing. Progress in Oceanography, 76(4): 399-442.

Burchard, H. and Petersen, O., 1999. Models of turbulence in the marine environment—A comparative study of two-equation turbulence models. Journal of Marine Systems, 21(1): 29-53.

Canuto, V., 2002. Critical Richardson numbers and gravity waves. ASTRONOMY AND ASTROPHYSICS-BERLIN-, 384(3): 1119-1123.

Carter, G.D. and Imberger, J., 1986. Vertically Rising Microstructure Profiler. Journal of Atmospheric and Oceanic Technology, 3(3): 462-471.

Chanson, H., Brown, R. and Trevethan, M., 2012. Turbulence measurements in a small subtropical estuary under king tide conditions. Environmental Fluid Mechanics, 12(3): 265-289.

d'Alessio, S., Abdella, K. and McFarlane, N., 1998. A new second-order turbulence closure scheme for modeling the oceanic mixed layer. Journal of physical oceanography, 28(8): 1624-1641.
Dallimore, C.J., Hodges, B.R. and Imberger, J., 2003. Coupling an underflow model to a three-dimensional hydrodynamic model. Journal of Hydraulic Engineering, 129(10): 748-757.
De Jong, J., Cao, L., Woodward, S., Salazar, J., Collins, L. and Meng, H., 2009. Dissipation rate estimation from PIV in zero-mean isotropic turbulence. Experiments in fluids, 46(3): 499-515.
Dillon, T., 1982a. Vertical overturns: A comparison of Thorpe and Ozmidov length scales. Journal of Geophysical Research, 87(C12): 9601-9613.
Dillon, T. and Park, M., 1987. The available potential energy of overturns as an indicator of mixing in the seasonal thermocline. Journal of Geophysical Research, 92(C5): 5345-5353.
Dillon, T.M., 1982b. Vertical overturns: A comparison of Thorpe and Ozmidov length scales. Journal of Geophysical Research, 87(C12): 9601.
Dillon, T.M. and Caldwell, D.R., 1980. The Batchelor spectrum and dissipation in the upper ocean. Journal of Geophysical Research: Oceans (1978–2012), 85(C4): 1910-1916.
Donohue, R. and Trust, S.R., 1994. Estimates of Nutrient Streamload in the Swan-Canning Catchment, 1987-1992. Swan River Trust.
Druzhinin, O.A., Troitskaya, Y.I. and Zilitinkevich, S.S., 2012. Direct numerical simulation of a turbulent wind over a wavy water surface. Journal of Geophysical Research, 117.
Durski, S.M., Glenn, S.M. and Haidvogel, D.B., 2004. Vertical mixing schemes in the coastal ocean: Comparison of the level 2.5 Mellor-Yamada scheme with an enhanced version of the K profile parameterization. Journal of Geophysical Research, 109(C1): C01015.
Elliott, J. and Oakey, N., 1976. Spectrum of small-scale oceanic temperature gradients. Journal of the Fisheries Board of Canada, 33(10): 2296-2306.
Elliott, Z.A. and Venayagamoorthy, S.K., 2011. Evaluation of turbulent Prandtl (Schmidt) number parameterizations for stably stratified environmental flows. Dynamics of Atmospheres and Oceans, 51(3): 137-150.
Ellison, T., 1957. Turbulent transport of heat and momentum from an infinite rough plane. J. Fluid Mech, 2(5): 456-466.
England, M.H. and Maier‐Reimer, E., 2001. Using chemical tracers to assess ocean models. Reviews of Geophysics, 39(1): 29-70.
Esau, I. and Grachev, A., 2007. Turbulent Prandtl number in stably stratified atmospheric boundary layer: intercomparison between LES and SHEBA data. e-WINDENG (005), 1–17.
Etemad-Shahidi, A. and Imberger, J., 2001. Anatomy of turbulence in thermally stratified lakes. Limnology and Oceanography: 1158-1170.
Etemad-Shahidi, A. and Imberger, J., 2002a. Anatomy of turbulence in a narrow and strongly stratified estuary. J Geophys Res C Oceans, 107(10.1029).
Etemad-Shahidi, A. and Imberger, J., 2002b. Anatomy of turbulence in a narrow and weakly stratified estuary. Marine and freshwater research, 53(4): 757-768.
Etemad-Shahidi, A. and Imberger, J., 2005. Vertical eddy diffusivity estimations in Swan river estuary. Dynamics of Atmospheres and Oceans, 39(3-4): 175-187.

Etemad-Shahidi, A. and Imberger, J., 2006. Diapycnal Mixing in the Thermocline of Lakes: Estimations by Different Methods. Environmental Fluid Mechanics, 6(3): 227-240.

Falter, J.L., Atkinson, M.J. and Merrifield, M.A., 2004. Mass-transfer limitation of nutrient uptake by a wave-dominated reef flat community. Limnology and Oceanography, 49(5): 1820-1831.

Ferguson, B., 1983. Doppler effect for sound emitted by a moving airborne source and received by acoustic sensors located above and below the sea surface, DTIC Document.

Ferziger, J.H. and Peric, M., 2002. Computational methods for fluid mechanics. Chapter, 5: 85-127.

Fiadeiro, M.E. and Veronis, G., 1984. Obtaining velocities from tracer distributions. Journal of physical oceanography, 14(11): 1734-1746.

Fofonoff, N.P. and Millard, R.C., 1983. Algorithms for computation of fundamental properties of seawater.

Forryan, A., Martin, A.P., Srokosz, M.A., Popova, E.E., Painter, S.C. and Renner, A.H.H., 2013. A new observationally motivated Richardson number based mixing parametrization for oceanic mesoscale flow. Journal of Geophysical Research: Oceans, 118(3): 1405-1419.

Fozdar, F.M., Parker, G.J. and Imberger, J., 1985. Matching temperature and conductivity sensor response characteristics. Journal of physical oceanography, 15(11): 1557-1569.

Galperin, B., Sukoriansky, S. and Anderson, P.S., 2007. On the critical Richardson number in stably stratified turbulence. Atmospheric Science Letters, 8(3): 65-69.

Gargett, A.E. and Holloway, G., 1984. Dissipation and diffusion by internal wave breaking. Journal of Marine Research, 42(1): 15-27.

George, W.K. and Lumley, J.L., 1973. The laser-Doppler velocimeter and its application to the measurement of turbulence. Journal of Fluid Mechanics, 60(2): 321-362.

Gibson, C. and Schwarz, W., 1963. The universal equilibrium spectra of turbulent velocity and scalar fields. Journal of Fluid Mechanics, 16(03): 365-384.

Gómez-Giraldo, A., Imberger, J. and Antenucci, J.P., 2008a. CLASSES OF HIGH-FREQUENCY INTERNAL WAVE MOTIONS AND THEIR IMPLICATIONS FOR ENERGY DISSIPATION: OBSERVATIONS FROM LAKE CONSTANCE. Application of modal analysis to strongly stratified lakes.

Gómez-Giraldo, A., Imberger, J., Antenucci, J.P. and Yeates, P.S., 2008b. Wind-shear-generated high-frequency internal waves as precursors to mixing in a stratified lake. Limnology and Oceanography, 53(1): 354.

Grant, H., Hughes, B., Vogel, W. and Moilliet, A., 1968. The spectrum of temperature fluctuations in turbulent flow.

Grant, H., Stewart, R. and Moilliet, A., 1962. Turbulence spectra from a tidal channel. J. Fluid Mech, 12(2): 241-268.

Gregg, M., 1977. A comparison of finestructure spectra from the main thermocline. Journal of physical oceanography, 7(1): 33-40.

Gregg, M.C., 1991. The study of mixing in the ocean: A brief history. Oceanography, 4(1): 39-45.

Hamilton, D.P., Chan, T., Robb, M.S., Pattiaratchi, C.B. and Herzfeld, M., 2001. The hydrology of the upper Swan River Estuary with focus on an artificial destratification trial. Hydrological Processes, 15(13): 2465-2480.
Hearn, C., Atkinson, M. and Falter, J., 2001. A physical derivation of nutrient-uptake rates in coral reefs: effects of roughness and waves. Coral Reefs, 20(4): 347-356.
Hendricks, P.J. and Rodenbusch, G., 1981. Interpretation of velocity profiles measured by freely sinking probes. Deep Sea Research Part A. Oceanographic Research Papers, 28(10): 1199-1213.
Herring, J.R. and McWilliams, J.C., 2006. Comparison of direct numerical simulation of two-dimensional turbulence with two-point closure: the effects of intermittency. Journal of Fluid Mechanics, 153(-1): 229.
Higgins, C.W., Froidevaux, M., Simeonov, V., Vercauteren, N., Barry, C. and Parlange, M.B., 2012. The effect of scale on the applicability of Taylor's Frozen turbulence hypothesis in the atmospheric boundary layer. Boundary-Layer Meteorology, 143(2): 379-391.
Hodges, B. and Dallimore, C., 2006. Estuary, Lake and Coastal Ocean Model: ELCOM. Science Manual. Centre of Water Research. University of Western Australia.
Hodges, B.R., 2000. Numerical Techniques in CWR-ELCOM (code release v. 1). CWR Manuscript WP 1422 BH.
Hodges, B.R. and Imberger, J., 2001. Simple curvilinear method for numerical methods of open channels. Journal of Hydraulic Engineering, 127(11): 949-958.
Hodges, B.R., Imberger, J., Saggio, A. and Winters, K.B., 2000. Modeling basin-scale internal waves in a stratified lake. Limnology and Oceanography, 45(7): 1603-1620.
Hodgkin, E.P. and Hesp, P., 1998. Estuaries to salt lakes: Holocene transformation of the estuarine ecosystems of south-western Australia. Marine and freshwater research, 49(3): 183-201.
Horne, E. and Toole, J., 1980. Sensor response mismatches and lag correction techniques for temperature-salinity profilers. Journal of physical oceanography, 10(7): 1122-1130.
Huang, Z.-C., Lenain, L., Melville, W.K., Middleton, J.H., Reineman, B., Statom, N. and McCabe, R.M., 2012. Dissipation of wave energy and turbulence in a shallow coral reef lagoon. Journal of Geophysical Research, 117(C3).
Imberger, J., 1985. The diurnal mixed layer. Limnology and Oceanography: 737-770.
Imberger, J., 1994. Transport processes in lakes: A review.
Imberger, J., 2004. A lake diagnostic system for managing lakes and reservoirs. Water Resources Impact, 6(1).
Imberger, J. and Head, R., 1994a. Measurement of turbulent properties in a natural system, Fundamentals and Advancements in Hydraulic Measurements and Experimentation. ASCE, pp. 1-20.
Imberger, J. and Head, R., 1994b. Measurement of turbulent properties in a natural system, The Symposium on Fundamentals and Advancements in Hydraulic Measurements and Experimentation, Buffalo, NY, USA, 08/01-05/94, pp. 1-20.
Imberger, J. and Ivey, G., 1991. On the nature of turbulence in a stratified fluid. Part II: Application to lakes. Journal of physical oceanography, 21(5): 659-680.

Imboden, D.M. and Wüest, A., 1995. Mixing mechanisms in lakes, Physics and chemistry of lakes. Springer, pp. 83-138.
Itsweire, E. and Helland, K., 1989. Spectra and energy transfer in stably stratified turbulence. Journal of Fluid Mechanics, 207(1): 419-452.
Itsweire, E., Koseff, J., Briggs, D. and Ferziger, J., 1993. Turbulence in stratified shear flows: Implications for interpreting shear-induced mixing in the ocean. Journal of physical oceanography, 23(7): 1508-1522.
Ivey, G. and Imberger, J., 1991. On the nature of turbulence in a stratified fluid. Part I: The energetics of mixing. Journal of physical oceanography, 21(5): 650-658.
Kay, D.J. and Jay, D.A., 2003. Interfacial mixing in a highly stratified estuary 1. Characteristics of mixing. Journal of Geophysical Research, 108(C3): 3072.
Keller, K.H. and Van Atta, C.W., 2000. An experimental investigation of the vertical temperature structure of homogeneous stratified shear turbulence. Journal of Fluid Mechanics, 425: 1-29.
Kocsis, O., Prandke, H., Stips, A., Simon, A. and Wüest, A., 1999. Comparison of dissipation of turbulent kinetic energy determined from shear and temperature microstructure. Journal of Marine Systems, 21(1): 67-84.
Kolmogorov, A.N., 1962. A refinement of previous hypotheses concerning the local structure of turbulence in a viscous incompressible fluid at high Reynolds number. J. Fluid Mech, 13(1): 82-85.
Large, W.G. and Gent, P.R., 1999. Validation of vertical mixing in an equatorial ocean model using large eddy simulations and observations. Journal of physical oceanography, 29(3): 449-464.
Laval, B., Hodges, B.R. and Imberger, J., 2003a. Reducing numerical diffusion effects with pycnocline filter. Journal of Hydraulic Engineering, 129(3): 215-224.
Laval, B., Imberger, J., Hodges, B.R. and Stocker, R., 2003b. Modeling circulation in lakes: Spatial and temporal variations. Limnology and Oceanography, 48(3): 983-994.
Lee, J.H. and Veronis, G., 1989. Determining velocities and mixing coefficients from tracers. Journal of physical oceanography, 19(4): 487-500.
Luketina, D.A. and Imberger, J., 2001. Determining turbulent kinetic energy dissipation from Batchelor curve fitting. Journal of Atmospheric and Oceanic Technology, 18(1): 100-113.
Lumley, J. and Terray, E., 1983. Kinematics of turbulence convected by a random wave field. Journal of physical oceanography, 13(11): 2000-2007.
Mahrt, L. and Vickers, D., 2006. Extremely weak mixing in stable conditions. Boundary-Layer Meteorology, 119(1): 19-39.
Marmorino, G.O. and Caldwell, D.R., 1978. Temperature finestructure and microstructure observations in a coastal upwelling region during a period of variable winds (Oregon, summer 1974). Deep Sea Research, 25(11): 1073-1106.
Marti, C.L. and Imberger, J., 2006. Dynamics of the benthic boundary layer in a strongly forced stratified lake. Hydrobiologia, 568(1): 217-233.
Mater, B.D., Schaad, S.M. and Venayagamoorthy, S.K., 2013. Relevance of the Thorpe length scale in stably stratified turbulence. Physics of Fluids, 25(076604): 076604.

Mauritsen, T. and Svensson, G., 2007. Observations of stably stratified shear-driven atmospheric turbulence at low and high Richardson numbers. Journal of the atmospheric sciences, 64(2): 645-655.
Mellor, G.L. and Yamada, T., 1982. Development of a turbulence closure model for geophysical fluid problems. Reviews of Geophysics, 20(4): 851-875.
Menke, W., 1989. Geophysical data analysis: discrete inverse theory, 45. Access Online via Elsevier.
Meunier, P., Diamessis, P.J. and Spedding, G.R., 2006. Self-preservation in stratified momentum wakes. Physics of Fluids, 18(10): 106601-106601-10.
Moum, J., 1990. Profiler Measurements of Vertical Velocity Fluctuations in the Ocean. Journal of Atmospheric and Oceanic Technology, 7: 323-333.
Nihoul, J.C. and Jamart, B.M., 1988. Small-scale turbulence and mixing in the ocean. Elsevier.
O'Callaghan, J.M., Pattiaratchi, C.B. and Hamilton, D.P., 2010. The role of intratidal oscillations in sediment resuspension in a diurnal, partially mixed estuary. Journal of Geophysical Research, 115(C7).
Osborn, T., 1980. Estimates of the local rate of vertical diffusion from dissipation measurements(ocean turbulence). Journal of physical oceanography, 10: 83-89.
Osborn, T.R. and Cox, C.S., 1972. Oceanic fine structure. Geophysical & Astrophysical Fluid Dynamics, 3(1): 321-345.
Ostrovskii, A. and Piterbarg, L., 1997. A New Method for Obtaining Velocity and Diffusivity from Time-Dependent Distributions of a Tracer via the Maximum Likelihood Estimator for the Advection–Diffusion Equation. Journal of Computational Physics, 133(2): 340-360.
Ozmidov, R., 1965. Energy distribution between oceanic motions of different scales. Izv. Atm. Ocean Phys, 1: 257-261.
Pardyjak, E., Monti, P. and Fernando, H., 2002. Flux Richardson number measurements in stable atmospheric shear flows. Journal of Fluid Mechanics, 459: 307-316.
Peters, H., 1997. Observations of stratified turbulent mixing in an estuary: Neap-to-spring variations during high river flow. Estuarine, Coastal and Shelf Science, 45(1): 69-88.
Peters, H. and Bokhorst, R., 2001. Microstructure observations of turbulent mixing in a partially mixed estuary. Part II: Salt flux and stress. Journal of physical oceanography, 31(4): 1105-1119.
Piccirillo, P. and Van Atta, C.W., 1997. The evolution of a uniformly sheared thermally stratified turbulent flow. Journal of Fluid Mechanics, 334: 61-86.
Pope, S.B., 2000. Turbulent flows. Cambridge university press.
Press, W.H., Teukolsky, S.A., Vetterling, W.T. and Flannery, B.P., 1992. Numerical Recipes in C: The Art of Scientific Computing (; Cambridge. Cambridge Univ. Press.
Price, J.F., Weller, R.A. and Pinkel, R., 1986. Diurnal cycling: Observations and models of the upper ocean response to diurnal heating, cooling, and wind mixing. Journal of Geophysical Research, 91(C7): 8411-8427.
Rodi, W., 1987. Examples of calculation methods for flow and mixing in stratified fluids. Journal of Geophysical Research: Oceans (1978–2012), 92(C5): 5305-5328.

Rohr, J., Itsweire, E., Helland, K. and Atta, C.V., 1988. Growth and decay of turbulence in a stably stratified shear flow. Journal of Fluid Mechanics, 195(1): 77-111.
Saarenrinne, P. and Piirto, M., 2000. Turbulent kinetic energy dissipation rate estimation from PIV velocity vector fields. Experiments in fluids, 29(1): S300-S307.
Saddoughi, S.G. and Veeravalli, S.V., 1994. Local isotropy in turbulent boundary layers at high Reynolds number. Journal of Fluid Mechanics, 268: 333-372.
Saggio, A. and Imberger, J., 2001. Mixing and turbulent fluxes in the metalimnion of a stratified lake. Limnology and Oceanography, 46(2): 392-409.
Schumann, U. and Gerz, T., 1995. Turbulent mixing in stably stratified shear flows. Journal of applied meteorology, 34(1): 33-48.
Simanjuntak, M.A., Imberger, J., Nakayama, K. and Ishikawa, T., 2011. Benthic and interfacial mixing in a strongly-stratified estuary. Journal of Hydraulic Research, 49(6): 791-798.
Simpson, J.H., Crawford, W.R., Rippeth, T.P., Campbell, A.R. and Cheok, J.V., 1996. The vertical structure of turbulent dissipation in shelf seas. Journal of physical oceanography, 26(8): 1579-1590.
Smyth, W.D. and Moum, J.N., 2000. Length scales of turbulence in stably stratified mixing layers. Physics of Fluids, 12: 1327.
Souza, A.J., 2007. THE USE OF ADCPS TO MEASURE TURBULENCE AND SPM IN SHELF SEAS, 2nd International Conference & Exhibition on" Underwater Acoustic Measurements: Technologies & Results, pp. 1-8.
Spedding, G., 1997. The evolution of initially turbulent bluff-body wakes at high internal Froude number. Journal of Fluid Mechanics, 337: 283-301.
Spedding, G., 2001. Anisotropy in turbulence profiles of stratified wakes. Physics of Fluids, 13: 2361.
Spigel, R.H. and Imberger, J., 1987. Mixing processes relevant to phytoplankton dynamics in lakes. New Zealand Journal of Marine and Freshwater Research, 21(3): 361-377.
Sreenivasan, K.R., 1995. On the universality of the Kolmogorov constant. Physics of Fluids, 7(11): 2778-2784.
Stephens, R. and Imberger, J., 1996. Dynamics of the Swan River Estuary: the seasonal variability. Marine and freshwater research, 47(3): 517-529.
Stevens, C., Ward, B., Law, C. and Walkington, M., 2011. Surface layer mixing during the SAGE ocean fertilization experiment. Deep Sea Research Part II: Topical Studies in Oceanography, 58(6): 776-785.
Stewart, R. and Grant, H.L., 1962. Determination of the rate of dissipation of turbulent energy near the sea surface in the presence of waves. Journal of Geophysical Research, 67(8): 3177-3180.
Stillinger, D., Helland, K. and Van Atta, C., 1983. Experiments on the transition of homogeneous turbulence to internal waves in a stratified fluid. Journal of Fluid Mechanics, 131(91): 122.
Stocker, R., 2012. Marine microbes see a sea of gradients. Science, 338(6107): 628-33.
Strang, E. and Fernando, H., 2001. Vertical mixing and transports through a stratified shear layer. Journal of physical oceanography, 31(8): 2026-2048.
Taylor, J.R. and Stocker, R., 2012. Trade-offs of chemotactic foraging in turbulent water. Science, 338(6107): 675-9.
Tennekes, H. and Lumley, J.L., 1972. A first course in turbulence. The MIT press.

Thorpe, S., 1977. Turbulence and mixing in a Scottish loch. Philosophical Transactions for the Royal Society of London. Series A, Mathematical and Physical Sciences: 125-181.
Thorpe, S.A., 2007. An introduction to ocean turbulence. Cambridge University Press Cambridge.
Trevethan, M. and Chanson, H., 2009. Turbulence and turbulent flux events in a small estuary. Environmental Fluid Mechanics, 10(3): 345-368.
Umlauf, L. and Burchard, H., 2003. A generic length-scale equation for geophysical turbulence models. Journal of Marine Research, 61(2): 235-265.
Webster, C., 1964. An experimental study of turbulence in a density-stratified shear flow. Journal of Fluid Mechanics, 19(02): 221-245.
Wijesekera, H., Allen, J.S. and Newberger, P., 2003. Modeling study of turbulent mixing over the continental shelf: Comparison of turbulent closure schemes. Journal of Geophysical Research: Oceans (1978–2012), 108(C3).
Wolk, F., Yamazaki, H., Seuront, L. and Lueck, R.G., 2002. A new free-fall profiler for measuring biophysical microstructure. Journal of Atmospheric and Oceanic Technology, 19(5): 780-793.
Wunsch, C., 1978. The North Atlantic general circulation west of 50 W determined by inverse methods. Reviews of Geophysics, 16(4): 583-620.
Wunsch, C., 1987. Using transient tracers: the regularization problem. Tellus B, 39(5): 477-492.
Wunsch, C., 1988. Transient tracers as a problem in control theory. Journal of Geophysical Research: Oceans (1978–2012), 93(C7): 8099-8110.
Yagüe, C., Viana, S., Maqueda, G. and Redondo, J., 2006. Influence of stability on the flux-profile relationships for wind speed, Φ m, and temperature, Φ h, for the stable atmospheric boundary layer. Nonlinear Processes in Geophysics, 13(2): 185-203.
Yamazaki, H. and Osborn, T., 1993. Direct estimation of heat flux in a seasonal thermocline. Journal of physical oceanography, 23(3): 503-516.
Yeates, P. and Imberger, J., 2003. Pseudo two‐dimensional simulations of internal and boundary fluxes in stratified lakes and reservoirs. International Journal of River Basin Management, 1(4): 297-319.
Yeates, P.S., 2007. Deep mixing in stratified lakes and reservoirs. Doctor of Philosophy PhD thesis, University of western Australia, University of Western Australia.
Yeates, P.S., Gómez-Giraldo, A. and Imberger, J., 2013. Observed relationships between microstructure patches and the gradient Richardson number in a thermally stratified lake. Environmental Fluid Mechanics, 13(3): 205-226.
Yeates, P.S., Imberger, J. and Dallimore, C., 2008. Thermistor chain data assimilation to improve hydrodynamic modeling skill in stratified lakes and reservoirs. Journal of Hydraulic Engineering, 134(8): 1123-1135.
Zaron, E.D. and Moum, J.N., 2009. A New Look at Richardson Number Mixing Schemes for Equatorial Ocean Modeling. Journal of physical oceanography, 39(10): 2652-2664.
Zilitinkevich, S., Elperin, T., Kleeorin, N. and Rogachevskii, I., 2007. Energy-and flux-budget (EFB) turbulence closure model for stably stratified flows. Part I: steady-state, homogeneous regimes. Boundary-Layer Meteorology, 125(2): 167-191.
Zilitinkevich, S., Elperin, T., Kleeorin, N., Rogachevskii, I. and Esau, I., 2013. A hierarchy of energy-and flux-budget (EFB) turbulence closure models for

stably-stratified geophysical flows. Boundary-Layer Meteorology, 146(3): 341-373.

Zilitinkevich, S., Elperin, T., Kleeorin, N., Rogachevskii, I., Esau, I. and Kouznetsov, R., 2010. Turbulence closure for stably stratified flows: Local and non-local formulations, 10th EMS Annual Meeting, 10th European Conference on Applications of Meteorology (ECAM) Abstracts, held Sept. 13-17, 2010 in Zürich, Switzerland. http://meetings. copernicus. org/ems2010/, id. EMS2010-808, pp. 808.